ABSTRACT

Title of Thesis: GAS TURBINE / SOLID OXIDE FUEL CELL HYBRIDS: INVESTIGATION OF AERODYNAMIC CHALLENGES AND PROGRESS TOWARDS A BENCH-SCALE DEMONSTRATOR

Lucas Merritt Pratt, Master of Science, 2019

Thesis Directed By: Professor Christopher Cadou, Department of Aerospace Engineering

Modern aircraft are becoming more electric making the efficiency of on-board electric power generation more important than ever before. Previous work has shown that integrated gas turbine and solid oxide fuel cell systems (GT-SOFCs) can be more efficient alternatives to shaft-driven mechanical generators. This work advances the GT-SOFC concept in three areas: 1) It develops an improved model of additional aerodynamic losses in nacelle-based installations and shows that external aerodynamic drag is an important factor that must be accounted for in those scenarios. Additionally, this work furthers the development of a lab-scale prototype GT-SOFC demonstrator system by 2) characterizing the performance of a commercial off-the-shelf (COTS) SOFC auxiliary power unit that will become part of the prototype; and 3) combining a scaled-down SOFC subsystem model with an existing thermodynamic model of a small COTS gas turbine to create an initial design for the prototype.

GAS TURBINE / SOLID OXIDE FUEL CELL HYBRIDS: INVESTIGATION OF AERODYNAMIC CHALLENGES AND PROGRESS TOWARDS A BENCH-SCALE DEMONSTRATOR

by

Lucas Merritt Pratt

Thesis submitted to the Faculty of the Graduate School of the
University of Maryland, College Park, in partial fulfillment
of the requirements for the degree of
Master of Science
2019

Advisory Committee:
Professor Christopher Cadou, Chair
Professor Kenneth Yu
Professor Chunsheng Wang

1 Dedication

In loving memory of Bubba.

2 Acknowledgements

First and foremost, this thesis would not have been completed without the help of my loving wife Thanh; thank you so much for keeping me sane, and the real goals always in mind.

Additionally, I would like to thank Professor Christopher Cadou for his continuous guidance and faith over the course of this project. Furthermore, I greatly appreciate the financial support of the Air Force Office of Scientific Research (AFOSR) through the National Defense Science and Engineering Graduate (NDSEG) Fellowship Program, which allowed me to continue to pursue the line of inquiry detailed in this work.

Separately, I would like to acknowledge my fellow graduate students and their bottomless well of camaraderie and friendship; specifically Wiam Attar, Andrew Ceruzzi, Brandon Chiclana, Daanish Maqbool, Thomas Pitzel, Stephen Vannoy, Steven Cale, and Colin Adamson. Thank you all for making the laboratory experience downright enjoyable.

Finally, on the technical side, I'd like to recognize the patient and gracious aid provided by both Tom Lavelle for NPSS programming help, and Tom Westrich for support in handling the SOFC APU safely and effectively.

3 Table of Contents

4 List of Tables

5 List of Figures

Nomenclature

Abbreviations:

AMI	Adaptive Materials Inc.
APU	Auxiliary Power Unit
CEA	Chemical Equilibrium with Applications (software package)
COTS	Commercial Off-The-Shelf
CPOx	Catalytic Partial Oxidation Reactor
CTE	Coefficient of Thermal Expansion
DGM	Dusty Gas Model
GT	Gas Turbine
HALE	High-Altitude Long-Endurance [aircraft]
HP	High Pressure
HPC	High Pressure Compressor
HPT	High Pressure Turbine
IDG	Integrated Drive Generator
LP	Low Pressure
LPC	Low Pressure Compressor
LPT	Low Pressure Turbine
MCFC	Molten Carbonate Fuel Cell
MEA	Membrane Electrode Assembly
NASA	National Aeronautics and Space Administration
NPSS	Numerical Propulsion System Simulation
OCV	Open Circuit Voltage
OPR	Overall Pressure Ratio
RTJ	Regional Transport Jet
SFC	Specific Fuel Consumption
SLS	Sea-Level Static
SLS	Sea-Level Static [conditions]
SOFC	Solid Oxide Fuel Cell
TER	Thermal Energy Reservoir
TIT	Turbine Inlet Temperature
TSFC	Thrust Specific Fuel Consumption
UAV	Uncrewed Aerial Vehicle

Symbols:

$\%Ox$	Degree of oxidation
C_D	Coefficient of Drag
C_L	Coefficient of Lift
C_L	Coefficient of Lift

C_f	Skin friction coefficient
$\dot{Q}$	Heating rate
Q_R	Specific Energy of fuel
S_{wet}	Wetted surface area
$\bar{V}$	Averaged voltage
$\dot{W}$	Power
i_0	Exchange Current Density
$\dot{m}$	Mass flow rate
$\dot{m}'$	Relative mass flow rate
m_1	Aircraft mass, full fuel load
m_2	Aircraft mass, dry
s_i	Parameter sensitivity
$u_{\dot{m}_{f,RSS}}$	Uncertainty in relative fuel flow rate, root-sum-square
u_{y_i}	Uncertainty of variable parameter
y_i	Variable parameter
π_{inlet}	Ram pressure recovery factor
h	Specific enthalpy
R	Gas Constant, Resistance
Π	Pressure Ratio
A	Area
AR	Aspect Ratio
D	Drag force, Diameter
E, V	Electrochemical Potential/Voltage
F	Faraday's Constant
FF	Pressure drag form factor
K	Coefficient of Induced Drag
K	Induced Drag Factor
L	Lift force, Length
M	Mach Number
N	Number
P	Pressure
Re	Reynolds Number
S	Surface Area of Wing?
T	Temperature
f	Fineness
g	Acceleration due to gravity
m	Mass
s	Range
t	Thickness
u, v	Flight velocity
α	Charge transfer coefficient
δ	Radial protrusion distance
ζ	Electric Power Fraction
η	Efficiency, overpotential
ρ	Density

ρ	Density

Subscripts:

0	Initial
a	Anode
act	Activation
air	Air
amb	Ambient condition
bp	Bypass
burn	Burner/Combustor
C	Compressor
c	Cathode
Carnot	With respect to the Carnot cycle
ch	Channel
cold	Low-temperature cycle condition
conc	Concentration
cross	Cross-sectional
duct	Duct
elec	Electrical system
eng,engine	Engine
ex1	Extrapolations from 1st minute of data
exAll	Extrapolation from all data
f,fuel	Fuel
FC, cell	Fuel Cell
first	First-minute values
gen	Mechanical Generator
hot	High-temperature cycle condition
i	Parameter counter
in	Input
ins	Insulation
last	Last-minute values
max	Maximum
min	Minimum
nernst	Nernst Potential
norm	Normalized
o,over	Overall
ohm	Ohmic
oper	Operating
out	Output
prop	Propulsion
rep	Repetition (of SOFC channels)
seg	Segments
T	Total condition (i.e. Pressure/Temperature)
t,turb	Turbine
th	thermal

$\zeta = 0$	Producing no electric power

6 Introduction

6.1 Motivation

6.1.1 Increasing Electrification of Aircraft

Historically, aircraft have not required substantial electrical power relative to the total power demand of the entire system. Even state-of-the-art commercial airliners marketed as 'more electric aircraft' have electric power fractions (ζ) of only 5% where electric power fraction is defined as the ratio of electrical power demand to total power demand at cruise conditions, (see Equation (1)).[1]

$$\zeta = \frac{\dot{W}_{elec}}{\dot{W}_{elec} + \dot{W}_{prop}} \tag{1}$$

Most of the energy stored on board the vehicle has been devoted to propulsion, because only a small amount was needed to supply electrical loads like instruments, lighting, and others. However, electrical loads have increased substantially in recent years as more controls, sensors, and utilities have been added to aircraft, or as existing systems like environmental or flight control systems have been converted to electric from pneumatic or hydraulic operation.[2] Even more recently (and radically), electrically-driven propulsion systems are also being considered even in larger aircraft. The National Aeronautics and Space Administration's (NASA) New Aviation Horizons 10-year plan charts the development of turbo-electric powered X-plane

technology demonstrators, with a number of possible configurations under consideration.[3] Such an aircraft would run a gas turbine on jet fuel purely (or nearly so) for electrical power generation, with the electricity then used for propulsion via fans or other means.

Figure 1 below, reproduced from [4], illustrates this trend, showing differences in electric power fraction between vehicles, using available data on a range of aircraft.[5], [6]

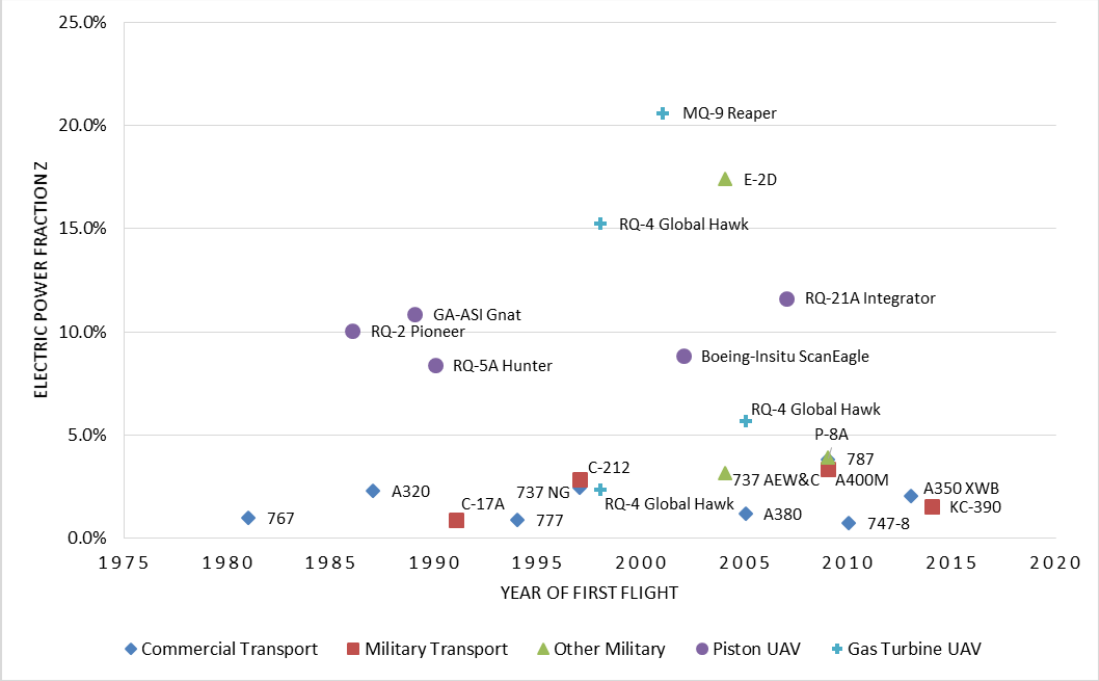

Figure 1: Electric Power Fraction at time of First Flight for various aircraft

We can also note from Figure 1 as well as Figure 2 (also reproduced from [4]) below that electric power fractions in uncrewed aerial vehicles (UAVs) are higher than in most other types of aircraft. The exception is the E-2D electronic warfare aircraft ($\zeta \approx 17\%$).

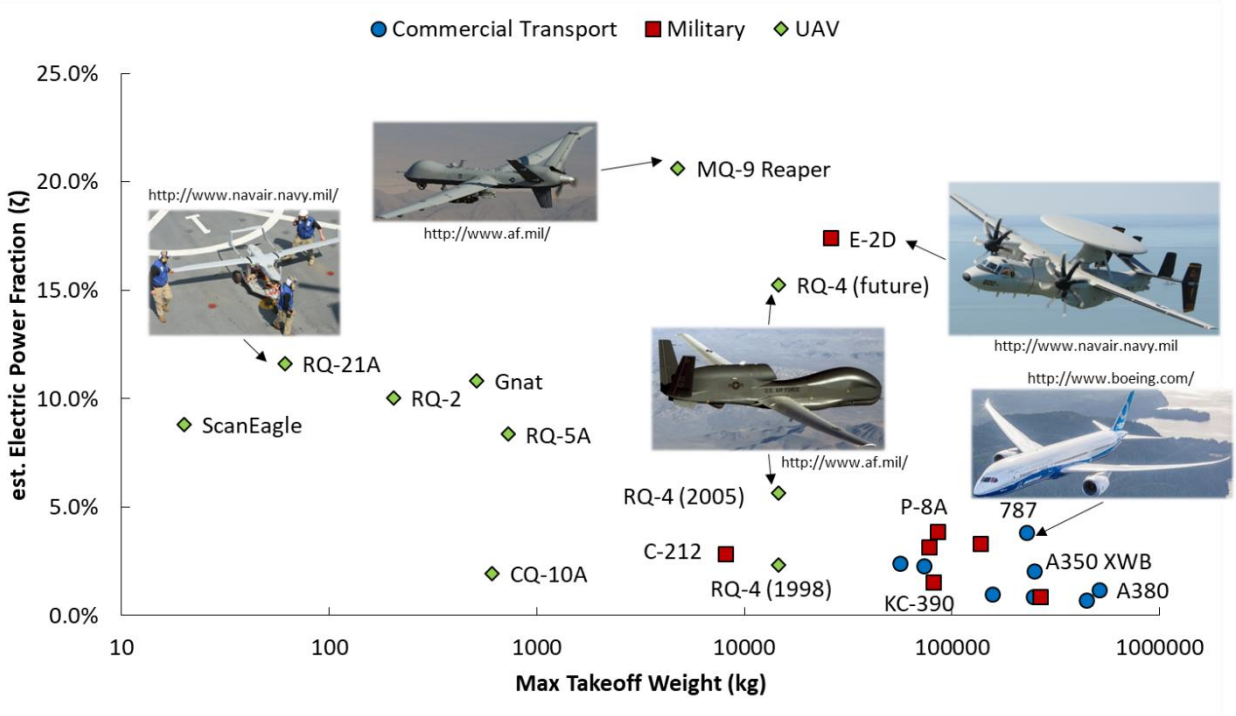

Figure 2: Estimated electric power fractions in various commercial, military, and unmanned aircraft.

Additionally, UAVs are often equipped with advanced sensor packages with large electrical power demands relative to their size. As a result, ζ can be as large as 21% in the aircraft considered.

In absolute terms, these are not an insubstantial power demands. The MQ-9 Reaper ($\zeta \approx 21\%$) requires 49kW of electrical power generation. Even though the electrical power fraction of the Boeing 787 is only 3.8%, the large scale of the aircraft implies that a full megawatt of electricity is required.[5], [6] Finally, all-electric aircraft have been proposed for a variety of purposes, including more efficient fuel usage, as well as reductions in noise and emissions. The primary challenge is achieving sufficiently high power to weight ratios for the overall system to be competitive with turbine engines.[7] Increasing electric power demands also increase the impact of

electrical generation efficiency on fuel burn, and thus the range/endurance of the vehicle.

6.1.2 Existing Electricity Sources and Alternatives

Currently, the most common sources of electrical power on aircraft are shaft-driven generators (sometimes described as Integrated Drive Generators, or IDGs) attached as a parasitic loads on the rotating components of the main propulsion system (see Figure 3) or separate auxiliary power units (APUs).[5], [6]

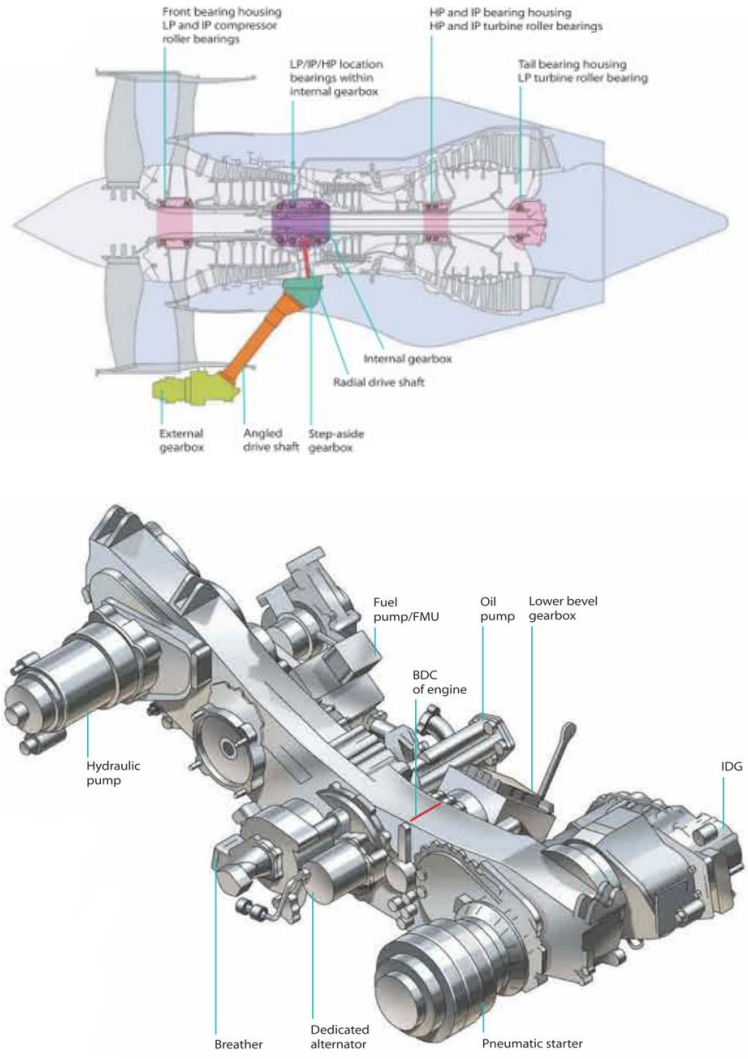

Figure 3: (Top) Schematic of turbofan with Accessory Gearbox and connections highlighted; (Bottom) Accessories gearbox. including IDG for electricity generation. Reproduced from [8, pp. 156–157]

Since the electrical generator itself is usually relatively efficient (mechanical to electrical conversion efficiencies of up to 95% are achievable in many settings[9]), the overall efficiency is most constrained by the efficiency of the heat engine used to rotate the generator's shaft. The underlying thermodynamic cycle is the Otto cycle for a piston

engine or the Brayton cycle for a gas turbine. The maximum efficiency of any heat engine is given by the Carnot efficiency (Equation (2)):

$$\eta_{Carnot} = 1 - T_{cold}/T_{hot} \tag{2}$$

Here T_{cold} is set by ambient conditions and T_{hot} usually by material limits of the engine components. Assuming ambient inlet conditions and a maximum material temperature of $1600°C$ results in a maximum possible efficiency of about 83%. However real cycles typically achieve less than half of the Carnot efficiency [10, p. 87] while modern aircraft Brayton cycles only achieve approximately 50% thermal efficiency (see Figure 4).

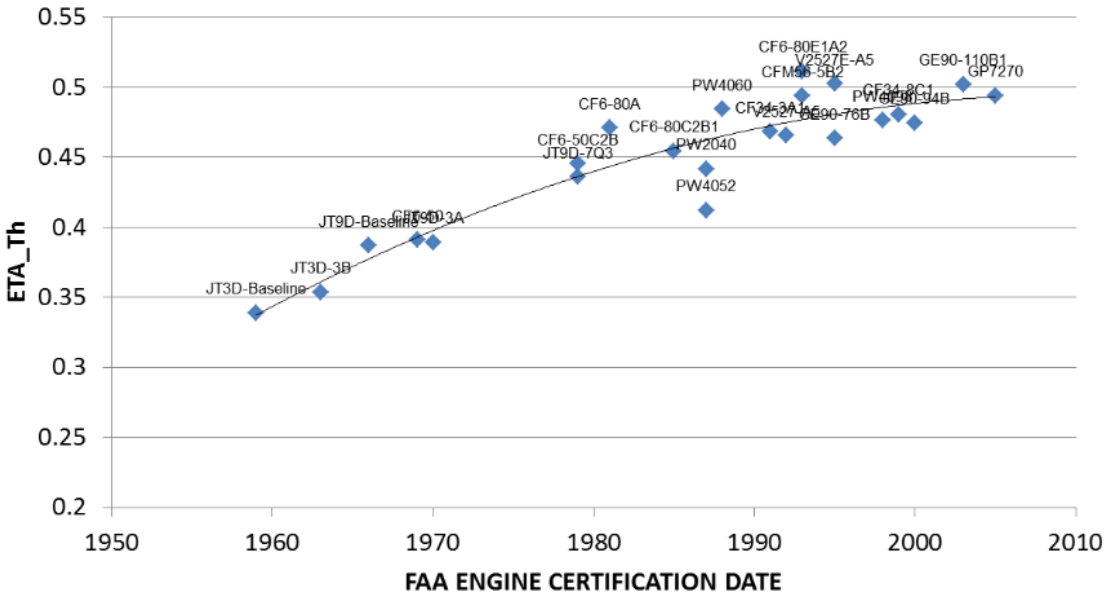

Figure 4: Thermal Efficiency Trend with Time (Cruise). Reproduced from Head [11]

Increasing electrical power demands increase the burden of this inefficiency on the operational range of the aircraft and suggests the need for alternative solutions for the production of electricity.[1]

Barring a shaft-driven electrical generator, there are several theoretical sources for electrical power. Conceivably, nuclear-electric and solar-electric power are options, but while both have been either considered or executed in a limited sense, nuclear demands too many risks (or outright pollution) and solar power is not power-dense enough nor reliably available enough (i.e. cloudy or night-time conditions) for use in most aircraft applications.[12]

The specific energy of current batteries (100-150 Wh/kg),[13], [14] and supercapacitors (approximately 1-10 Wh/kg)[15] are so low compared to liquid hydrocarbon fuels (12.3 kWh/kg) that batteries will consume most if not all of the aircraft's useful load capacity. Worse, a battery's mass does not decrease during flight, resulting in a further disadvantage compared to liquid fuels. The impact of expending fuel during flight can be illustrated by comparing the expression for the range of a fueled aircraft (Equation (3), from Eqn. 5.19 in [16, p. 152]) to the one for a battery-powered aircraft (Equation (4), derived from integration of Eqn. 5.16 in [16, p. 152]).

$$s_{fuel} = \eta_0 \left(\frac{L}{\mathcal{D}}\right) \ln\left(\frac{m_1}{m_2}\right) \frac{Q_R}{g} \tag{3}$$

$$s_{elec} = \eta_0 \left(\frac{L}{\mathcal{D}}\right) \left(1 - \frac{m_2}{m_1}\right) \frac{Q_R}{g} \tag{4}$$

Here, s is the operating range of the vehicle, Q_R is the specific energy of the fuel (energy per unit of mass), $L/\mathcal{D}$ is the vehicle lift to drag ratio, g is the acceleration due to gravity, m_1 is the mass of the aircraft with the power source (fuel or battery) and m_2 is the empty weight of the aircraft without fuel or battery—equivalent in the fuel-laden case to be the final mass of the aircraft.[16] For otherwise identical aircraft

(equivalent propulsive efficiency, $L/\mathcal{D}$, and empty weight), a fuel-powered aircraft with 30% fuel mass fraction will have almost 20% greater range than the battery-powered one simply because the weight of the fuel-powered aircraft decreases over the course of the flight. Figure 5 below shows that this effect becomes even more important as the fuel mass fraction increases. For context, an ERJ-145 regional transport jet has a fuel mass fraction of ~20% (~12% range improvement for fuel over battery) while the long-haul A380 has a fuel mass fraction of just under 51% (~41% range improvement).[5]

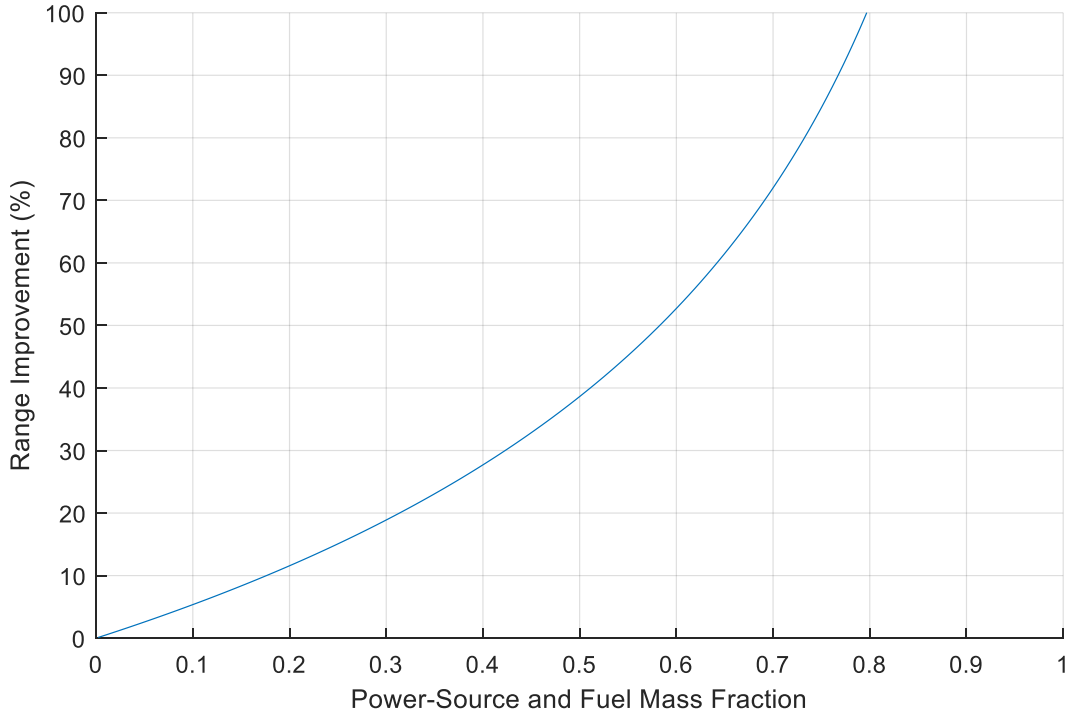

Figure 5: Percentage Range improvement from expending fuel vs. a retained power source (e.g. a battery) for a range of fuel/power-source mass fractions

As such, there is substantial advantage to continuing the use of fuel as the energy source for aircraft with increasingly large electric power requirements.

Improvements in this case need to come from the efficiency by which that fuel is converted to electrical power. As an illustration, we can analyze this scenario as two separate cycles operating in tandem, as in Figure 6. This is essentially describing an APU that is more efficient than the main engine.

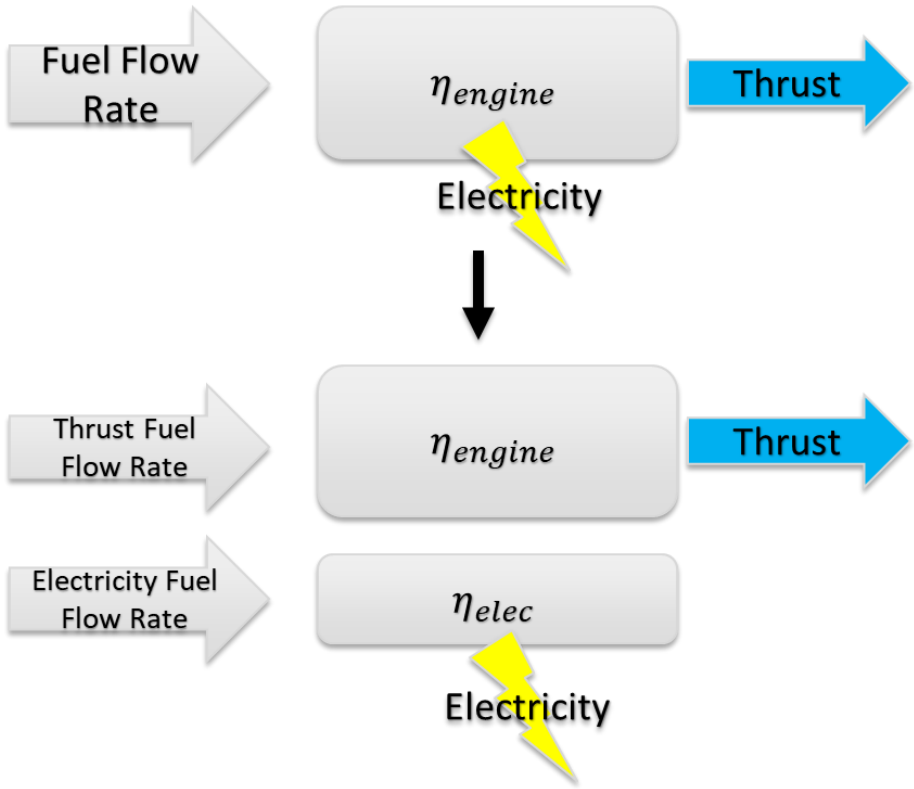

Figure 6: A single fuel cycle that produces electricity in addition to thrust (top) vs. a separated cycle with electricity produced with its own fuel supply

To give some idea of what impacts this might have on fuel demand and range, consider a simple model of the fuel flow rate demand for an aircraft based on the derivation of the Breguet range equation by Hill and Peterson[16, p. 152] in Equation (5) where $\dot{m}_f$ is the fuel flow rate, m is the mass of the aircraft, u is the aircraft velocity, Q_R is the fuel energy, (L/D) is the lift-to-drag ratio of the airframe and η_o is the overall efficiency of the propulsion system:

$$\dot{m}_f = \frac{mgu}{\eta_o Q_R (L/D)} \tag{5}$$

The additional fuel to produce some additional electric power fraction can be added to this equation as a second additive term with an alternative efficiency value, as shown in Equation (6) where η_{elec} is the efficiency of the electrical production cycle:

$$\dot{m}_f = \frac{mgu}{Q_R (L/D)} \left(\frac{1}{\eta_o} + \left(\frac{\zeta}{1-\zeta} \right) \frac{1}{\eta_{elec}} \right) \tag{6}$$

Additionally, in order to make the comparison more general, we can consider the relative fuel flow rate $\dot{m}_f'$ of different cases (Equation (7)), where the relative fuel flow rate is defined as the fuel flow rate divided by the fuel flow rate when no electric power is generated.

$$\dot{m}_f' = \frac{\dot{m}_f}{\dot{m}_{f,\zeta=0}} \tag{7}$$

The relative fuel flow rate is a number no smaller than unity, since electric power generated in this case is not used for propulsion and will always require additional fuel to produce. Relative fuel flow rate is the primary means of comparing designs in the rest of this work as our main goal is usually to minimize the overall fuel consumption at all electric power demands.

For an aircraft engine with an overall efficiency η_o based on a propulsive (η_{prop}) and thermal (η_{th}) efficiency, Figure 7 compares relative fuel flow rates based on two different notional separated electrical cycles. The first is a mechanical generator with efficiency $\eta_{elec,gen}$ based on that of the thermal efficiency of the engine while (to

avoid burying the lede) the second is a fuel cell with a somewhat better efficiency $\eta_{elec,FC}$, though the analysis applies to any alternative cycle:

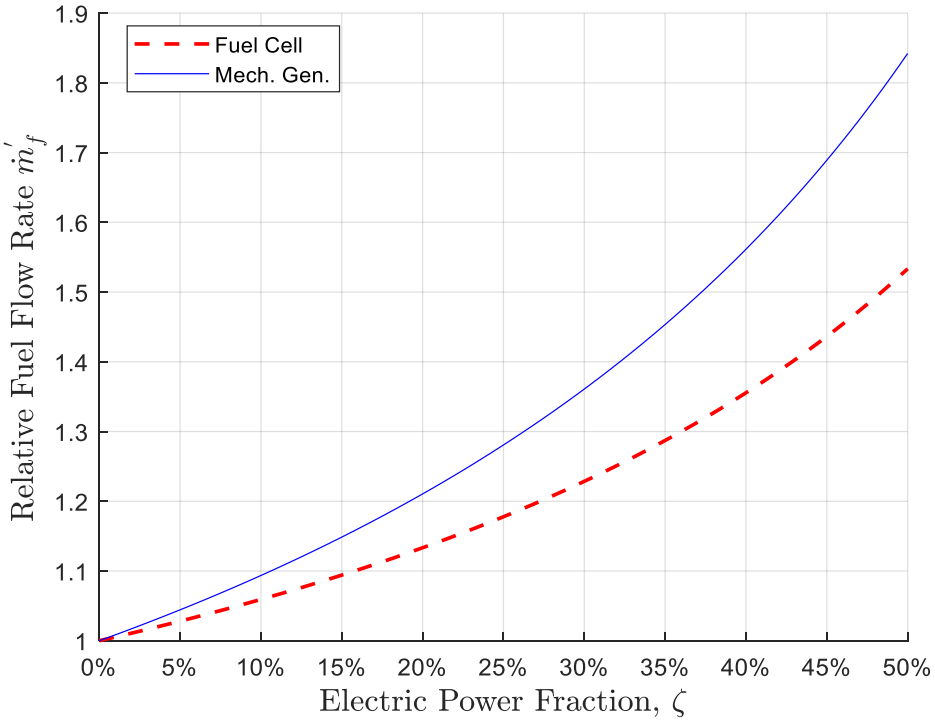

Variable	*Value*
η_{th}	0.5
η_{prop}	0.8
η_{FC}	0.6
η_{gen}	0.95
η_o	$\eta_{th}\eta_p$
$\eta_{elec,gen}$	$\eta_{th}\eta_{gen}$
$\eta_{elec,FC}$	η_{FC}

Figure 7: Relative Fuel Flow Rate for Mechanical Generator and Fuel Cell separated cycles at varying electric power fraction

The numbers provided for efficiency are mainly for illustration, but are reasonable for aircraft engines[11] and solid oxide fuel cells[10, p. 478]. The results show an improvement of about 10% in relative fuel flow rate at an electric power fraction of 25%. This simple analysis does not consider any of the actual properties of fuel cell operation, so the next section will explore their potential further.

6.1.3 Potential Solution: Fuel Cells

If we want to retain the advantage of using fuel and rely on the existing aircraft fuel infrastructure used for most aircraft today, carbon tolerant fuel cells (in particular, solid-oxide fuel cells or SOFC's) are an option. Fuel cells are often capable of producing electrical power from fuel with substantially greater efficiency than heat engines driving mechanical generators. The potential of this advantage stems from the different trend in efficiency observed for fuel cells, which is related to the Gibbs Free Energy rather than the ratio of operating temperatures.

Figure 8 illustrates the comparison while indicating usual operating ranges for gas turbines and SOFCs. The ideal operating range of the SOFC lies between ambient conditions, and the maximum required for efficient operation of a large heat engine, suggesting that those conditions are achievable in the same system.

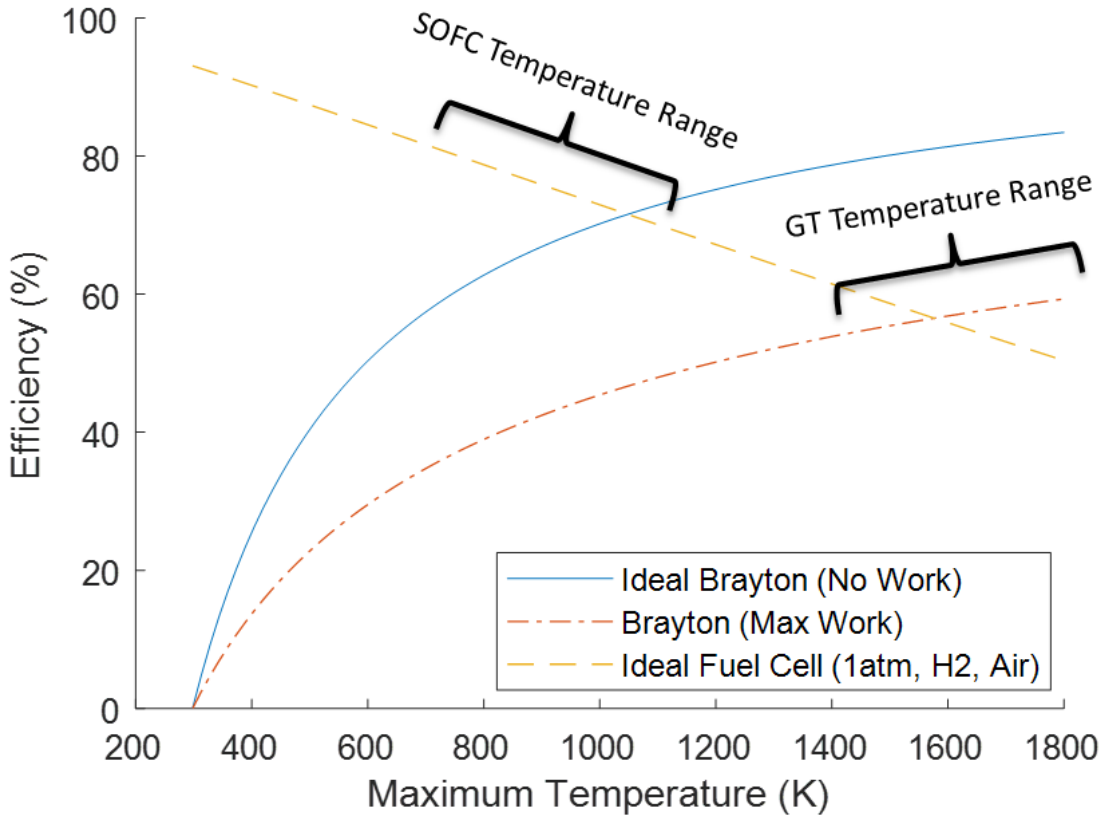

Figure 8: Efficiency Trend with Operating Temperature of Fuel Cells and Brayton Cycle

One important problem with fuel cells is that the infrastructure required to operate them (pumps, blowers, etc.) can be large and heavy. The problem is compounded by the need for large fuel cells in order to maximize the conversion of the fuel to electricity within the cell to avoid simply releasing unburned fuel. These factors tend to make fuel cell systems inappropriate for use on aircraft in the form of the APU (i.e. as a separated cycle) previously analyzed. However, recent work has shown that these problems can be mitigated by integrating the fuel reformer and fuel cell stack directly into an aircraft gas turbine's flow path.[17] Next we will expand on this hybridization of gas turbine and fuel cell.

6.1.4 GT-SOFC Hybridization

Explanations of the fundamental operations of gas turbines and fuel cells are provided in Appendices in sections 13.1 and 13.2 for the reader who is not already familiar with these technologies. Engine/fuel-cell hybrids come in a variety of forms. In the case considered here, a solid oxide fuel cell subsystem is inserted into the gas turbine's hot section in parallel with the combustor as illustrated in Figure 9. The reformer, a catalytic partial oxidation reactor (or CPOx) upstream of the fuel cell stack and the fuel cell stack itself receive pressurized air from the compressor and discharge their exhaust into the engine's combustor, enabling any unconsumed fuel to be recovered in the Brayton cycle.

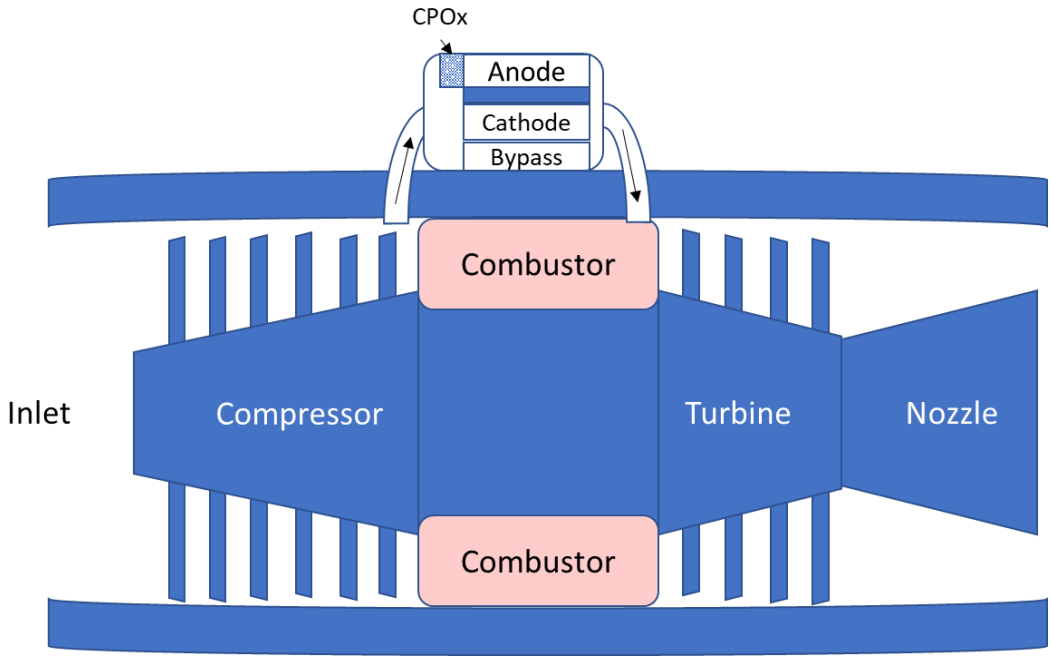

Figure 9: Simplified layout of turbojet GT-SOFC

The advantage of generating electrical power in this way arises from several possible synergies between the engine and fuel cell:

First, the GT provides most balance of plant functions for the fuel cell stack by acting as blowers and pumps, as well as providing waste heat that can be used to maintain the SOFC's membrane electrode assembly (MEA) at the appropriate temperature.

Second, placement in the hot section of the Brayton cycle ensures that the stack is pressurized above ambient conditions. The result is a moderate improvement in efficiency (with diminishing returns) as shown in Figure 10.

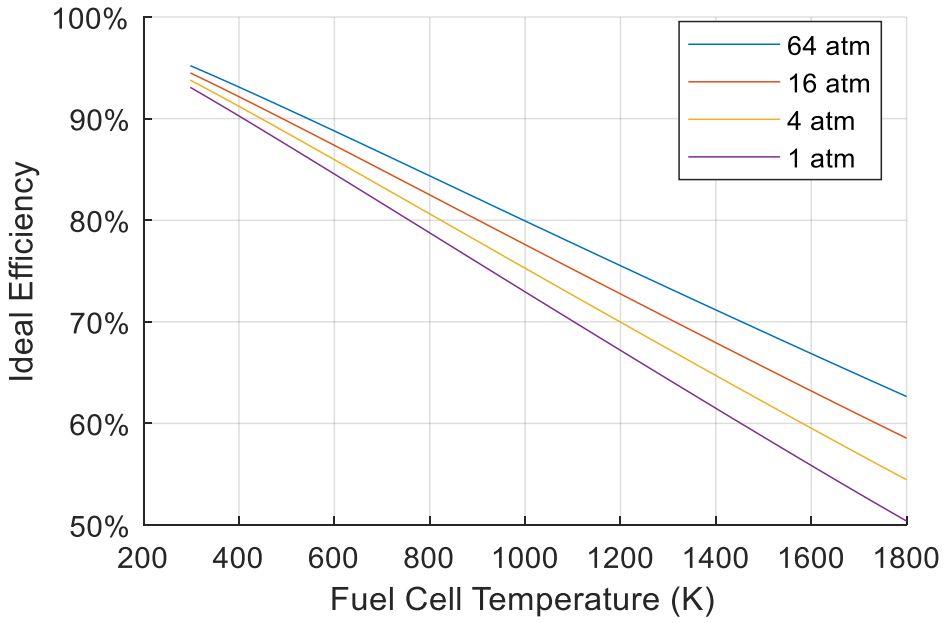

Figure 10: Ideal fuel cell efficiency at varying operating temperature for different operating pressures. Anode: 100% H2 gas, Cathode: Air

Additionally, higher pressure operation yields increased chemical kinetic rates than would be available at ambient pressure, with improvements between 68-78% power

density possible at relatively modest pressure ratios, as shown in Figure 11 reproduced from Henke et. al. This results in a higher power density, reducing the size and weight of the stack needed to meet a target electrical load.

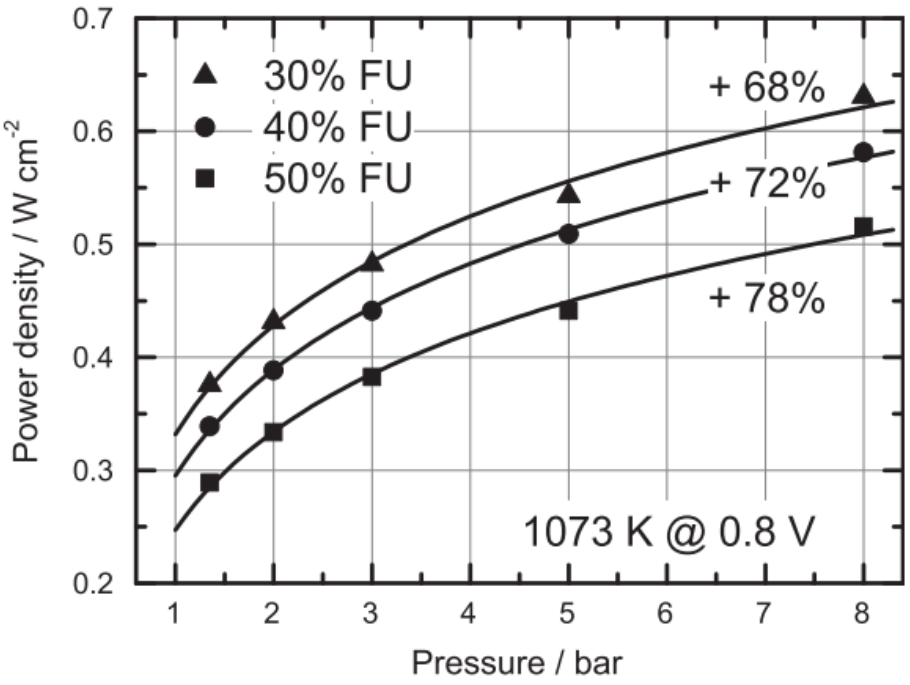

Figure 11: Power density vs. pressure for different fuel utilizations at constant temperature and voltage. Reproduced from [18]

Third, fuel cell exhaust discharges into the GT combustor so that waste enthalpy and unconsumed fuel are recovered in the Brayton cycle. as shown by Yi and Kim [19], this characteristic makes system-level performance less sensitive to low conversion in the fuel cell, enabling the use of smaller/lighter fuel cell stacks.

Finally, the turbine inlet temperature (TIT) constrains the amount of power that can be extracted from the spool to drive mechanical generators. The placement of the SOFC into the flow path before the combustor means that the electrical power generated never

reaches the turbine as additional heat, only the waste enthalpy from SOFC inefficiencies. The result is that greater amounts of electrical power can be generated before encountering the TIT material limitations.

6.2 Prior Work

6.2.1 GT/SOFC Literature Review

Waters reviewed the literature in 2015 and identified a range of research on ground-based hybridized GT-SOFC power plants, GT-SOFC APUs for aircraft, and all-electric UAVs and compared the scale, efficiency, fuel, and other characteristics of the various systems.[1], [17] Most of the studies of hybridization focus on integrated GT-SOFC systems for large-scale stationary ground-based power generation rather than aircraft [20]–[28]. At least one hybrid system used a molten carbonate fuel cell (MCFC) [29]. Natural gas [20], [23], [26] methane [21], [24], [25], [29] and syngas [27], [28] are the fuels considered. Both external[24]–[27] and internal[20]–[23] fuel reformers are employed with powers ranging from 5 kilowatts[26] to 2.4 megawatts[21]. A separate review of GT-SOFC hybridization in power plant applications reaffirmed the efficiency and fuel flexibility advantages offered by hybridization.[30] Another review article discussed transient operation and controls for hybrid power plants.[31]

One notable takeaway from the range of work described above is that most studies, especially those for vehicles, use very simplistic fuel cell models that do not

account for ‘down the channel’ performance. Also, of the already small number of studies focused on aircraft, even fewer consider traditional hydrocarbon fuels and use for combined propulsion and power.

An updated survey of the literature since Waters’ 2015 review includes additional GT-SOFC power plant models in several different configurations. An interesting general finding that applies to this work was found by Yi and Kim; that the optimal SOFC conversion rate for hybrid systems such as GT-SOFCs drops substantially compared to standalone SOFC systems—in their scenarios to 70% from 80% in a ground-based system.[19] Almost all works found use simple (i.e. zero-dimensional) fuel cell models although some are at least validated via comparison to existing systems.[19], [32]–[35] Modeling has been performed in MATLAB,[36] Aspen HYSIS,[19], [37] custom iterative solvers,[35], [38], [39] or even optimizations through a genetic algorithm[34]. An exception is a power plant study by Dang, Zhao, and Xi however noted deficiencies (in particular problematic temperature distributions inside the cell) in black-box or zero-dimensional models, and attempt to reach higher fidelity through what they describe as a “quasi-2D model.”[40]

Regarding aircraft hybrid systems, Valencia et. al. provide a distributed electrical fan system along with a turbofan for propulsion driven by a hybrid GT-SOFC system using liquid hydrogen for the fuel cell and kerosene for the GT. They employ another zero-dimensional SOFC model but include mass modeling considerations for the fuel cell and hydrogen storage, and use a similar notional

SOFC location to this work.[41] A more complicated one-dimensional Simulink model developed by Chakravarthula, Roberts, and Wolff uses an internal steam reformer in an SOFC-combustor model, requiring the combustor to initially heat air entering the SOFC.[42] The intended system configuration uses an electrically-driven compressor (powered by the SOFC as the only load), removing the need for a turbine before passing the hot exhaust gases through a nozzle to produce thrust. However, their SOFC model applies a very limited set of reactions possible at anode and cathode, makes modeling assumptions including no variation in temperature for cells at the edge of a stack versus the center, and neglects pressure losses through the SOFC. Furthermore, at this point in development the overall system described does not account for the water required in order to operate the steam reformer. Similarly employing the electric power from the SOFC for propulsion, Okai et. al. use another Simulink model to investigate a "core" GT-SOFC hybrid power generator that provides propulsive thrust as well as electrical power provided to other fans dedicated to boundary-layer ingestion.[43]–[45] They also use what is likely a zero-dimensional model but the precise methodology is not well specified although it is claimed that the model accounts for stack size "Partial pressure, thermal relations, losses, and other points."[43]

An extended version of the literature summary table initially developed by Waters [17] is included as Table 1 below.

Table 1. Previous Investigations of integrated GT-SOFC power/propulsion systems. Based on review by Waters, with updates in italic type.

Reference	Platform	Size	Fuel	Efficiency (if stated)
Ground based:	~	~	~	~
Abbasi and Jiang [22]		132 kW		
Calise et al. [20]	MATLAB	1.5 MW	natural gas	η_{sys}>90%, η_{elec}=68%
Chan and Tian [23]		2.1 MW	natural gas	η_{sys}=84%, η_{elec}=62%
Costamagna et al. [25]	MATLAB	300 kW	natural gas	η_{sys}>60%
Haseli et al. [21]	MATLAB	2.4 MW	methane	η_{sys}=60%
Leto et al. [29]	IPSE Pro	140 kW	natural gas	η_{sys}=60-70%
Palsson et al. [24]	Aspen Plus	500 kW	methane	η_{sys}=86%, η_{elec}=60%
Suther et al. [27]	Aspen Plus		syngas	
Veyo et al. [46]		300 kW, 1MW	natural gas	$\eta_{sys} = 59\%$
Zhao et al. [28]	MATLAB		coal syngas	η_{sys}=50-60%
Yi et. al. [32]	*Aspen HYSYS*	*~500 MW*	*natural gas*	η_{sys}*=73-76%*
Rokni [33]	*DNA*	*~930-1300 MW*	*natural gas*	η_{sys}*=65%*
Hajabdollahi and Fu [34]	*Aspen Plus*	*20 MW*	*natural gas*	$\eta_{sys} = 48.49\%\ (Exergy)$
Choudhary [35]	*C++*		*Syngas; natural gas*	$\eta_{sys} = 73.46\%\ (max)$
Yi and Kim [19]	*Aspen HYSYS*		*natural gas*	$\eta_{sys} = 72\%$
Saisirirat [36]	*MATLAB*	*463 kW*	*hydrogen*	$\eta_{sys} = 58\%$
Yi et. al. [37]	*Aspen HYSYS*	*503 MW*	*natural gas*	$\eta_{sys} = 64.7\%$
Pirkandi et. al. [38]		*2.12 MW*	*natural gas*	$\eta_{sys} = 62.2$
Sghaier et. al. [39]	*EES*	*120 MW*	*natural gas*	$\eta_{sys} > 60\%$
Dang, Zhao, and Xi. [40]		221.25 kW	natural gas	$\eta_{sys} = 58.86\%$
APUs:	~	~	~	~
Braun et al. [47]	Proprietary	300 kW	Jet-A	SL: η_{sys}=53%, cruise: η_{sys}=70%
Eelman et al. [48]	MATLAB	370 kW	jet fuel	η_{sys}>70%
Freeh et al. [49]	NPSS	200 kW	Jet-A	η_{sys}=40%, η_{elec}=65%
Freeh et al. [50]	NPSS	440 kW	Jet-A	η_{sys}=73%
Rajashekara et al. [51], [52]		440 kW, >880 kg	jet fuel	SL: η_{sys}=61%, cruise: η_{sys}=74%
Steffen et al. [53]	NPSS	440 kW, 1396 kg	Jet-A	η_{sys}=62%
All-electric:	~	~	~	~
Himansu et al. [54]	MATLAB	20 kW, 50 kW	H_2	
Aguiar et al. [55]		140 kW	H_2	η_{sys}=54-66%
Air Propulsion & Power:	~	~	~	~
Waters et. al. [17]	*NPSS*	*0-500 kW*	*Jet-A*	
Bradley et. al. [56], [57]	*Proprietary*	*180-780 kW*	*Various*	
Valencia et. al. [41]	*MATLAB*		*hydrogen; kerosene*	
Chakravarthula et. al. [42]	*Simulink*		*methane*	
Okai et. al. [43]–[45]	*Simulink*		*hydrogen; jet fuel*	

Comparing the state of the art today with that identified by Waters in 2015, it is apparent that the majority of research involving hybrid GT-SOFC systems continues to use zero-dimensional fuel cell models in both ground power and aircraft-based systems. The rare exceptions are Dang, Zhao and Xi with their quasi-2D model, and Chakravarthula, Roberts, and Wolff, who apply a complex quasi-1D SOFC model, though still with modeling simplifications such as a small number of electrochemical reactions considered within the flow, and an incomplete set of turbomachinery components for a complete cycle analysis. Additionally, studies on fuel-cell-based all-electric or electrically-assisted vehicle propulsion systems tend to focus on hydrogen gas as a primary fuel for the SOFC, as well as the use of the electrical power generated by the system to drive fans to produce additional thrust.

6.2.2 Prior Work at Maryland

Waters developed Equation (8) below for an aircraft's fuel consumption that accounts for the effect of electric power consumption, efficiency of electric power generation, and the weight of the power generating equipment. In this expression, $\dot{m}'$ is the relative fuel flow rate (the fuel flow rate divided by the fuel flow rate when no electric power is generated), TSFC is the thrust-specific fuel consumption of the gas turbine, Q_f is the fuel heating value, v is the flight velocity, ζ is again the electric power fraction, η_{elec} is the efficiency of the electrical power generation, $C_{D,min}$ is the static drag coefficient of the drag polar, K is the induced drag coefficient, and $C_{L,min}$

is the lift coefficient, m_0 and m_{elec} are initial masses and the varying mass of the electrical generating system respectively, S is the aircraft wing area, g is the acceleration due to gravity, and ρ is the air density:[1]

$$\dot{m}_f' = \left(1 + \frac{v}{(TSFC)Q_R\eta_{elec}}\left[\frac{\zeta}{1-\zeta}\right]\right)\frac{\left[C_{D,min} + K\left(\frac{(m_0 + m_{elec})g}{\frac{1}{2}\rho v^2 S} - C_{L,min}\right)^2\right]}{\left[C_{D,min} + K\left(\frac{m_0 g}{\frac{1}{2}\rho v^2 S} - C_{L,min}\right)^2\right]} \quad (8)$$

Equation (8) shows that increasing the electric power fraction increases fuel consumption which in turn decreases range and endurance. It also shows that the sensitivity of fuel flow rate to electrical generator weight depends on the induced drag coefficient (K) of the vehicle and weight of the generator relative to the vehicle's empty weight. Thus, the additional weight of the fuel cell influences the overall fuel consumption rate of the vehicle.

The propulsion system (and vehicle performance) were modeled using a NASA-developed simulation environment called Numerical Propulsion System Simulation (NPSS).[58] The output of this research was a range of integrated gas turbine and solid-oxide fuel cell (GT-SOFC) system models that included, most notably, a set of fuel cell component models that were much more advanced than those used in most (if not all) prior hybrid modeling efforts. These advanced features included down-the-channel performance variation, multi-step equilibrium chemistry, realistic representations of heat transfer within the fuel cell structure, and realistic

representation of oxygen ion transport via the dusty gas model [59] through the electrolyte. Some key conclusions of Waters' work were:

- GT-SOFC hybridization can reduce fuel consumption in Global-Hawk class UAVs by 5% or more depending upon how much electric power is desired.
- GT-SOFC hybridization can produce more than five times the amount of electric power than a spool-driven mechanical generator before encountering the turbine inlet temperature limitation of the engine.
- External aerodynamic drag could be an important limitation in pylon-mounted applications.

The promise of GT-SOFC hybridization identified by Waters led to follow-on efforts to construct and test a bench-scale prototype of a GT-SOFC hybrid that could be used to validate system models and to identify practical problems associated with integrating solid oxide fuel cells into the hot section of a gas turbine. Since the main goal is learning – not to produce a 'practical' flight weight system at this stage – it was decided to construct one using commercial off-the-shelf (COTS) engines and fuel cells. A small turbojet engine (AMT Olympus HP) was selected for this purpose and characterized by Vannoy who measured its performance and developed a validated model of the engine in NPSS [4], [60]–[62].

6.3 Objective and Approach

6.3.1 Objectives

The objectives pursued by this thesis are threefold. The first objective is to improve the features of the GT-SOFC model by investigating the effects of flow path and aerodynamic drag on overall fuel consumption in pylon-mounted configurations. The second objective is to develop an experimentally validated model of a COTS fuel cell (an Adaptive Materials Defender D300 [63]). Finally, the GT-SOFC model will be scaled down to the general size of the COTS fuel cell and coupled with Vannoy's model of a COTS gas turbine (an AMT Olympus High Power) to provide general sizing information for a system model that can inform the design of an integrated bench-scale demonstrator based on these components. Future work will integrate the COTS fuel cell model to improve the design on the bench-scale generator. Taken together, the overall objective of the thesis is to improve our understanding of how to exploit GT-SOFC hybridization to reduce fuel consumption in aircraft.

6.3.2 Approach

The overall approach in this work has three main steps. First, I investigate the effects of external aerodynamic drag on vehicle-level fuel consumption in the larger pylon-mounted configurations that Waters investigated. Second, I measure the performance and physical characteristics of the COTS APU looking towards using this information to develop an experimentally validated model of the integrated

CPOx/SOFC components in NPSS. Finally, I scale down and integrate the CPOx/SOFC model with Vannoy's GT model and use the resulting system model to predict the operating characteristics (temperatures, flow rates, etc.) needed in order to design the bench-scale prototype. Future measurements of APU performance will be used to improve this initial system model.

6.3.3 COTS Components

The bench-scale GT platform considered in this modeling effort is the AMT Olympus High Power, a small 230N of thrust kerosene-fueled turbojet. The inflow rate for the engine is 0.45 kg/s at maximum thrust, with a corresponding maximum RPM of 108,500. The engine was acquired in 'university configuration' which means that it has pre-installed ports for measuring temperatures and pressures at the various internal stages of the gas turbine cycle.

The APU is an Adaptive Materials Defender D300, capable of generating a maximum of 300 Watts of electrical power.[63] It is rated at 32V and 9.5 Amps maximum output. The system is fueled by propane at approximately 1 standard cubic centimeter per second fed through a sulfur filter. The system is started by a lithium ion battery that maintains the balance of plant as the SOFC reaches its operating temperature.

Figure 12 below shows both COTS systems side by side (the engine is on a thrust stand) to provide a sense of relative scale.

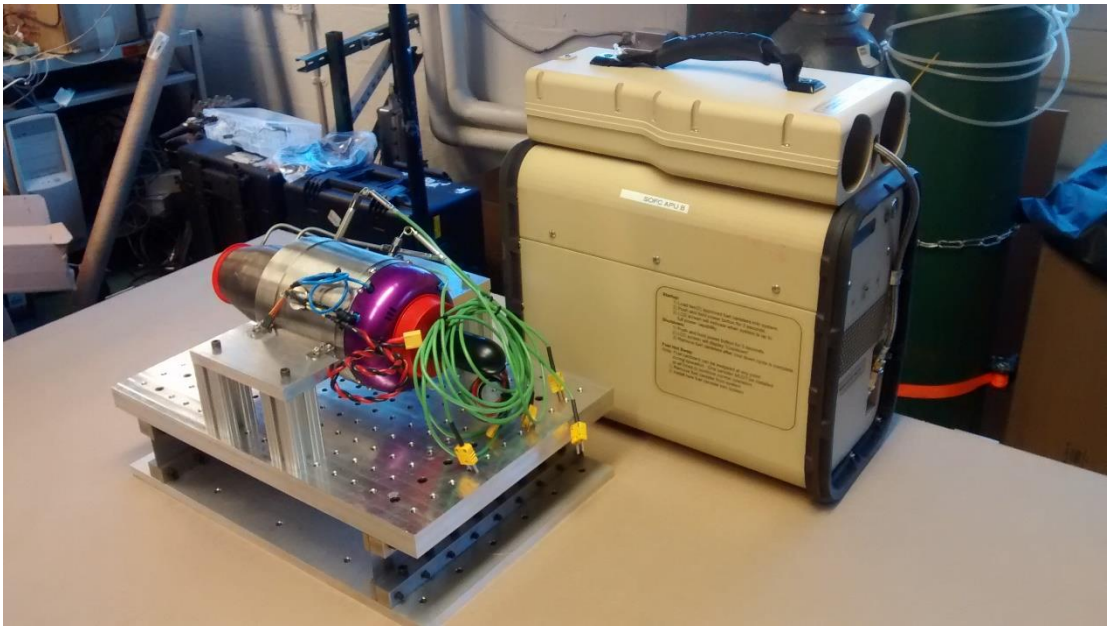

Figure 12: AMT Olympus HP at left, with Ultra/AMI D300 SOFC APU at right

7 Modeling Environment

7.1 Overview

7.1.1 Background

NPSS[58], [64]–[67] is a gas turbine modeling code and framework developed by NASA with the intention of being highly customizable in both complexity and scope. It is further designed to be able to include a variety of custom components that can function as “black boxes” in order to enable consortia of engine manufacturing companies to collaborate without revealing proprietary information. From a practical perspective, the modeling language is object-oriented, and closely based on C++. NPSS was also the simulation platform used in the work immediately preceding this thesis. [1], [17], [68]

An engine is modeled in NPSS by linking together models of individual engine components like compressors, combustors, fans, ducts, turbines, and nozzles. These component models are also often referred to as “elements”. The elements usually contain dependent and independent variables. NPSS solves the system by adjusting the values of the independent variables in order to conserve mass and energy while maintaining any other conditions specified for each component. The number of independent variables must equal the number of dependent variables in order to have a solvable system.

7.1.2 Solver Process

The component files and list of connections are considered the "model" of a specific system under consideration. Additionally, other files may be called or included to perform calculations or collect data. Finally, a case (file) is specified, which provides specific operating conditions and a range of dependent and independent variables to solve for the given case.

The solution process for any given case assumes a number of "dependent" characteristics, variables for which the system is required to match, as well as an equal number of "independent" values that may be altered in order to yield the dependent values. Another way of thinking about this is that there are a number of targets we want to achieve (for instance a particular turbine inlet temperature), and an equal number of knobs (for instance, the fuel flow rate into a combustor) to turn in order to reach these targets. Engine size parameters can also be independent variables meaning that the engine can be essentially "rubber" if need be. Given a set of starting conditions, the solver uses a modified Newton's method with Broyden updates to drive the values of the dependent variables to their intended targets by adjusting the values of the independent parameters.[69] This is accomplished by calculating a Jacobian matrix that contains the first derivatives of each independent variable with respect to each dependent variable. Calculating the Jacobian is computationally expensive so the inexact Broyden update method (generating an approximation of the

Jacobian by comparison to the previous iteration of the calculation) is often used until certain solution criteria are not met.[69]

7.1.3 Thermodynamic Model

Thermodynamic equilibrium is assumed throughout the flow enabling local species concentrations to be determined using NASA's Chemical Equilibrium with Applications (CEA) [70]. CEA accomplishes this by adjusting the composition and temperature to minimize the Gibbs free energy, and so yield equilibrium conditions. Applying CEA while considering the full range of known species is computationally expensive, and as such fewer species may be considered as desired, especially if only a known range of constituents is possible. In NPSS, CEA is applied at each port connection between components, or internally within components as necessary.

7.2 Modes of Operation

The particular sets of dependent and independent variables chosen to create and solve an NPSS model are fall into two categories: "on-design" and "off-design". In on-design cases, a particular level of performance is targeted and NPSS adjusts the size and geometry of the engine (through the scaling of known performance maps for reference turbine and compressor components) in order to achieve it for a specified operating condition. In contrast, for off-design cases the engine geometry is fixed and the resulting performance changes as the operating conditions (outside air temperature and pressure, throttle setting, etc.) vary.[66] Some independent and

dependent variables are the same in both modes of operation. Examples include the requirement for steady-state operation that the net torque on all spool shafts is zero, (dependent) or the fuel flow rate supplied to the combustor (independent). Table 2 and Table 3 below provide lists of independent and dependent variables for different modes, with more detail available in prior work by Waters.[1, p. 240] In all modes, an equal number of dependents and independents must be present in the solver in order to generate a Jacobian. Note that in the Off-Design scenarios in Table 3, this requirement means that at least one of the optional dependents is necessary for any given off-design run. More optional dependents (that are not mutually exclusive, such as the different options for thrust targets) from the list can be added to the solver as optional independents are chosen.

Table 2: Summary List of Dependents and Independents for Turbofan GT-SOFC On-Design Cases

INDEPENDENTS	DEPENDENTS
Present in all modeling runs	***Present in all modeling runs***
• HPT performance map parameter	• Net torque on the HP shaft = zero
• LPT performance map parameter	• Net torque on the LP shaft = zero
• HP shaft mechanical rotation speed, *N*	***Present in all 'On-Design' runs***
• LP shaft mechanical rotation speed, *N*	• Turbine inlet temperature = target value
• Burner fuel mass flow, $\dot{m}_{fuel}$	• Net thrust = target value
Present in all 'On-Design' runs	• Shaft speed = prediction by correlation
• Inlet air mass flow rate, $\dot{m}_{air}$	• Shaft speed = prediction by correlation

Table 3: Summary List of Dependents and Independents for Turbofan GT-SOFC On-Design Cases

INDEPENDENTS	DEPENDENTS
Present in all modeling runs	***Present in all modeling runs***
• HPT performance map parameter	• Net torque on the HP shaft = zero
• LPT performance map parameter	• Net torque on the LP shaft = zero
• HP shaft mechanical rotation speed, *N*	***Present in all 'Off-Design' runs***
• LP shaft mechanical rotation speed, *N*	• HPC Corr. mass flow = performance map value
• Burner fuel mass flow, $\dot{m}_{fuel}$	• LPC Corr. mass flow = performance map value
Present in all 'Off-Design' runs	• Fan Corr. mass flow = performance map value
• Inlet air mass flow rate, $\dot{m}_{air}$	• HPT Corr. mass flow = performance map value
FC Assembly airflow bypass ratio	• LPT Corr. mass flow = performance map value
• HPC performance map parameter	• Mass flow / area = primary nozzle demand
• LPC performance map parameter	• Mass flow / area = secondary nozzle demand
• LPC performance map parameter	OPTIONAL DEPENDENT REQUIRED
Optional Independents for 'Off-Design' runs	***Optional Dependents for 'Off-Design' runs***
• CPOx fuel mass flow, $\dot{m}_{fuel}$	• Turbine inlet temperature = target value
• SOFC insulation thickness	• Net thrust = target value
• # of radially repeating FC units per stack	• Thrust = calculated drag incl. FC mass
	• Thrust = calc. drag incl. FC mass and profile
	• FC exhaust degree of oxidation = target
	• FC exhaust temperature =target value
	• FC electrical power output = target value

Additionally, the last parameter listed for the independents (the number of radially repeating FC units per stack) is only applied as an independent to be shifted slightly when attempting to maintain a specific condition during a sensitivity analysis. See section 8.4 for more detailed information on the physical meaning of the fuel cell parameters.

Traditionally for any given set of cases of interest, 'on-design' calculations are performed first, where NPSS adjusts the physical parameters (including scaling of existing component performance maps) of the engine to achieve a particular fixed level of performance. After this baseline is established, then 'off-design' calculations are performed where NPSS calculates variation in the engine's performance as

operating conditions (like outside air temperature, outside air pressure, throttle setting, etc.) are adjusted over a range of conditions.

In this work, for all cases the physical characteristics of the engine are first determined using an ‘on-design’ calculation where no CPOx/SOFC subsystem is present. Subsequent calculations add the CPOx/SOFC subsystem and operate in ‘off-design’ mode for the gas turbine components which essentially ‘fixes’ the baseline gas turbine hardware. Various fuel cell hardware and operating parameters (this scenario’s ‘independent variables’) are adjusted to meet a set of specified electrical load and/or targeted internal conditions. By convention of the NPSS software, the fuel cell components of the GT-SOFC are designed (i.e. their physical parameters determined) in this ‘off-design’ state in order to fix the design (i.e. sizing) of the turbomachinery components while the overall GT-SOFC system may be considered ‘on-design’. True ‘off-design’ operation for the full GT-SOFC system is relegated to future work. Figure 13 illustrates this progression.

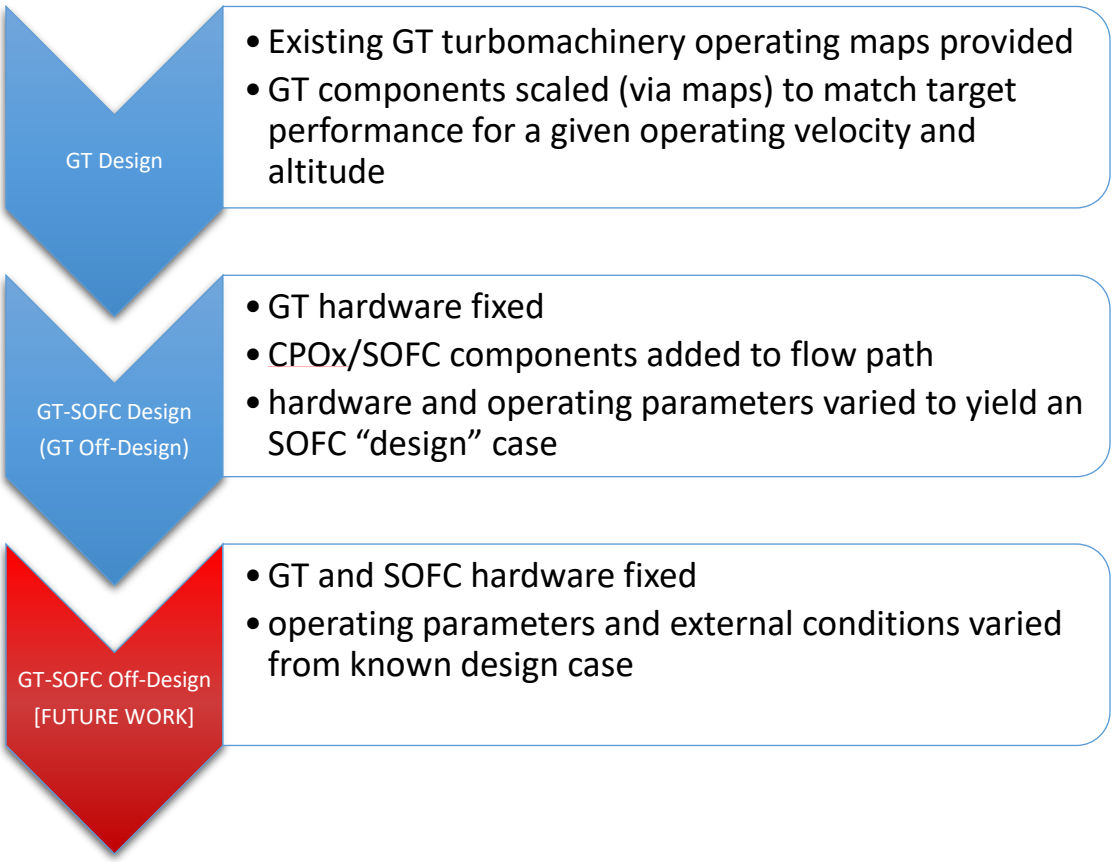

Figure 13: NPSS Calculation Procedure for GT-SOFC

7.3 Performance Measures

Several performance metrics are calculated from the solved GT-SOFC system model. The most important metrics are the previously-discussed electric power fraction (Equation. (1)) and relative fuel flow rate (Equation (7)), as well as the overall integrated GT-SOFC efficiency (Equation (9)) Drag components, subcomponent efficiencies, species compositions, and other quantities may also be of interest.

Finally the overall efficiency of the system, (Eqn. (9)) defined as the electrical plus propulsive power divided by the fuel input power (fuel flow rate times the heat of combustion), is another performance metric considered.

$$\eta_{over} = \frac{\left(\dot{W}_{prop} + \dot{W}_{elec}\right)}{\dot{m}_f Q_R} \tag{9}$$

The overall efficiency compares the total useful energy extracted from the fuel consumed to the total energy available in the fuel via combustion. This value is less operationally important in aircraft than relative fuel flow rate but is relevant for general comparison to other hybrid power systems like terrestrial installations where no vehicle baseline consumption exists.

7.4 Viewers and Analysis Tools

In NPSS, the results of a solution are traditionally output to DataViewer (hereafter "viewer") files, which are separate scripts that collect and output data from the model into useful formats. Prior work by Waters developed customized viewers for the GT-SOFC model, though these were limited to specific important variables deemed important at runtime. However, experience has shown that performing further analysis will often require additional information regarding system state that would be inaccessible without rerunning the simulation—often costly in terms of time, and storage of the precise script for a given scenario. As part of this work, a custom NPSS viewer/function ("SaveAll") was developed to extend the built-in VarDumpViewer,

[66, p. 99] which captures and outputs all existing variables in the computational model in a list to the terminal.

The custom viewer captures these list outputs for each solution and places them into a single file. An external script is then used to reorganize the long lists into a tabular format where each row represents a single NPSS solution. The result is usually a table with tens of thousands of columns and relatively few (<100) rows. Data processing software such as MATLAB can effectively pull selected columns (i.e. variables) from the large table for analysis; interrogating new variables only requires providing their name and re-reading the large table file. This custom viewer is general to NPSS and minimizes requirements to make alterations to standard viewer files to collect and process data as changes and updates are made to experimental models.

8 GT-SOFC System Model

The models discussed in this section are oriented towards the design of a laboratory-scale demonstrator system. The models used to investigate drag effects will be explained in Chapter 9. The GT and the SOFC subsystem (comprising of the CPOx, fuel cell inlet, SOFC, and combiner components) models can be considered separately prior to integration into a single model. For simplicity, we will consider a turbojet system in this section, but the same explanations hold for other systems in this work such as turbofans with the addition of additional compressor and turbine stages and a fan component.

8.1 Gas Turbine NPSS Model

More detailed information about each of these components is available elsewhere [1, Ch. 2] but summaries have been included here for convenience.

8.1.1 Inlet

The standard NPSS Inlet component [71, p. (2-68)] accepts (and usually slows) the incoming flow prior to entering the compressor. It is sketched schematically in Figure 14.

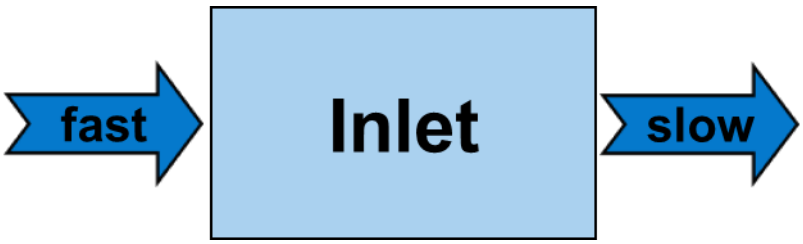

Figure 14: Inlet component diagram, reproduced from [1, p. 58]

The conditions at the inlet exit are set by the ambient flight conditions and the efficiency with which the total pressure is recovered (ram pressure recovery factor π_{inlet}). This efficiency is related to the shape of the inlet, ambient flow velocity, associated boundary layer losses, and other factors:

$$P_{T,out} = P_{T,amb}\pi_{inlet}$$

For static operation as in the laboratory-scale demonstrator, this recovery factor is taken to be $\pi_{inlet} = 1$. [62, p. 45] For other conditions it may be some other set input value or the result of a calculation based on the ambient conditions.[1, p. 58] Additionally, this component calculates the ram drag (D_{ram}), determined by multiplying the collected free stream air mass into the inlet ($\dot{m}_{in}$) by the cruise velocity (v_{amb}). Note, however, that 'ram drag' is accounted for by the overall force balance on the engine and is not considered as a separate source of drag.

8.1.2 Compressor

The compressor model uses the existing NPSS Compressor element, [71, p. (2-38)] and takes inputs of an airflow and a rotating shaft, as illustrated in Figure 15.

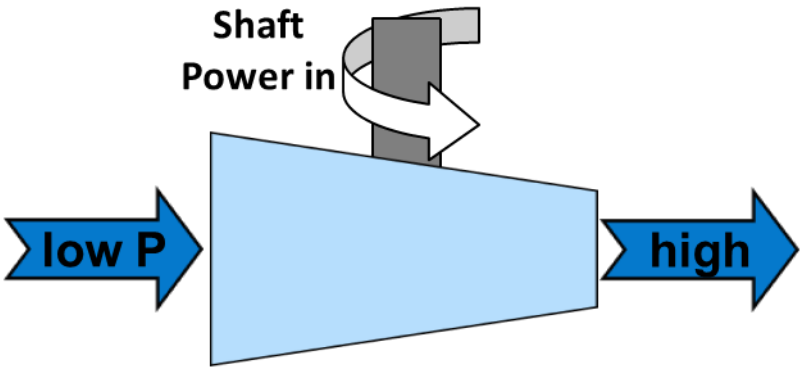

Figure 15: Compressor component diagram, reproduced from [1, p. 64]

The model takes power from the shaft to raise the pressure of the airflow to a level according to a specified pressure ratio and efficiency. An operating line parameter $RlineMap$ traverses the performance map, an example of which is provided in Figure 16.

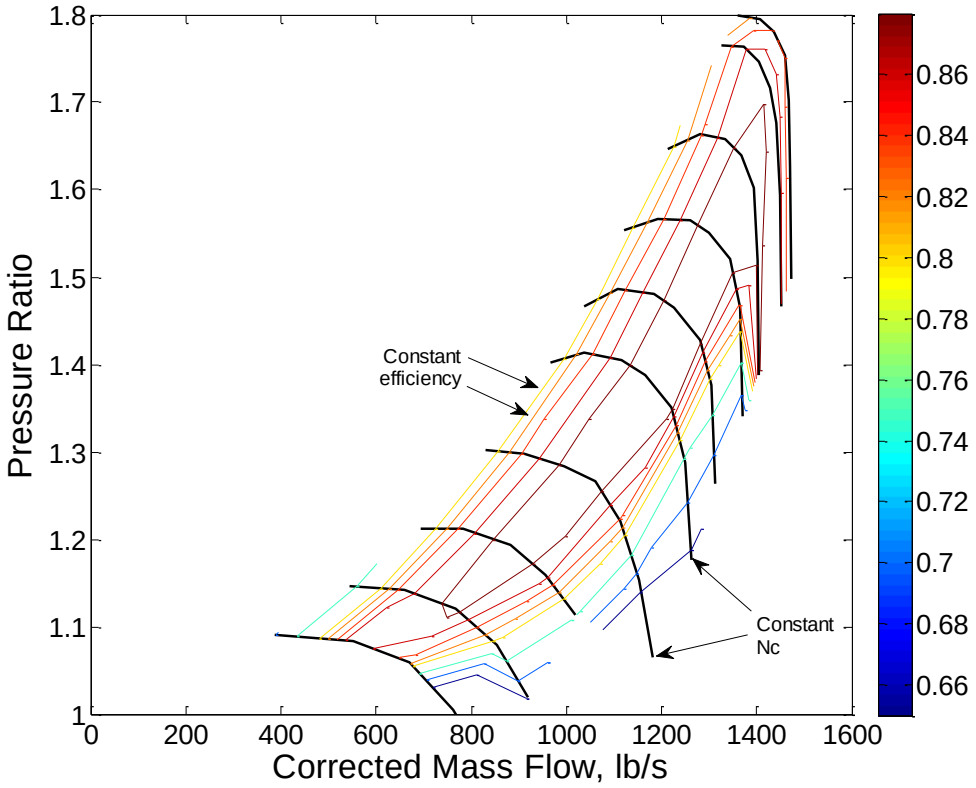

Figure 16: Example compressor performance map, reproduced from [1, p. 54]

In "on-design" cases, the compressor corrected mass flow, efficiency and pressure ratio are specified along with the desired level of thrust. The user provides a compressor map that establishes the relationship between pressure ratio, mass flow rate, speed, and efficiency. If mass flow, pressure ratio and efficiency at the design point on the compressor map do not match the desired design conditions, the map is scaled linearly in order to achieve this. An illustration of this procedure is shown in Figure 17.

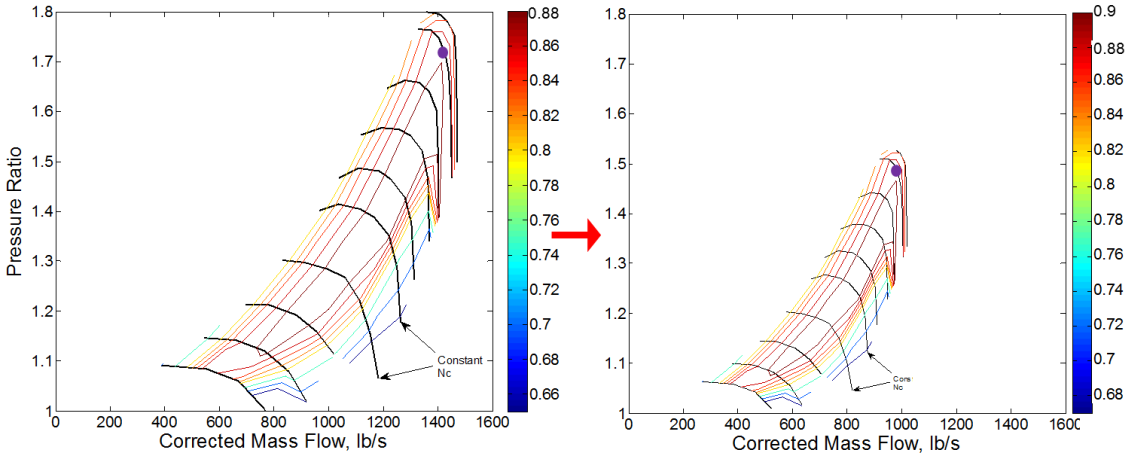

Figure 17: Compressor performance map scaling, reproduced from [1, p. 55]

This scaled map is used in subsequent calculations of 'off-design' performance. This process creates what is essentially a "rubber" engine component while in 'design mode'. Further off-design cases calculated use this scaled performance map to determine the output airflow conditions.

The exit flow conditions are calculated for a position on the compression map via the following relations, where (P_T) is the total pressure and $(\Pi_c = P_{out}/P_{in})$ is the pressure ratio:

$$P_{T,out} = P_{T,in}\Pi_c \tag{10}$$

The exit enthalpy of the flow (setting other flow properties and determining the input power) is determined from the compressor efficiency (η_c) and the specific enthalpy assuming isentropic compression (h_s) at a specified pressure ratio (Π_c) where h_T is the total specific enthalpy of the flow in or out of the system:

$$h_{T,out} = \frac{(h_s - h_{T,in})}{\eta_c} + h_{T,in} \tag{11}$$

The power $(\dot{W})$ requirement of the shaft is thus the difference between the inlet and exit enthalpy, scaled by the mass flow rate of air $(\dot{m})$ through the system:

$$\dot{W}_c = \dot{m}(h_{T,out} - h_{T,in}) \tag{12}$$

8.1.3 Combustor

The combustor model uses the existing BurnerNASA NPSS component.[71, p. (2-33)] It takes inputs of an airflow stream and a fuel stream and outputs a stream of combustion products (as illustrated in Figure 18) at the equilibrium temperature of the mixture at a pressure lower than the input pressure based on a user-specified combustor pressure ratio (π_b).

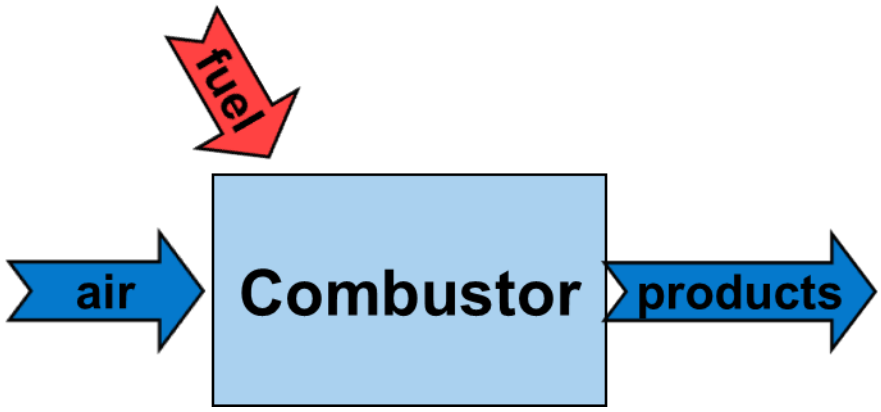

Figure 18: Combustor component diagram, adapted from [1, p. 52]

The composition and temperature of the exit flow is determined using NASA's Chemical Equilibrium with Applications. Additional possible specifications are combustion efficiency, heat loss, pressure losses due to heat release (as in Rayleigh flow).

8.1.4 Turbine

The existing Turbine NPSS model [71, p. (2-107)] as depicted in Figure 19 functions similarly but oppositely to the compressor model (Figure 19).

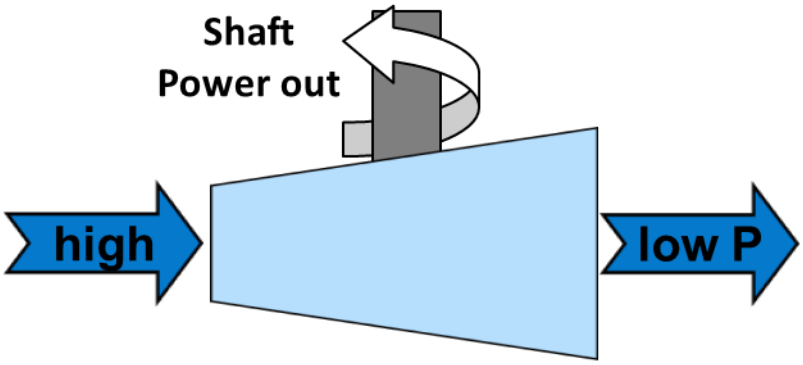

Figure 19: Turbine component diagram, adapted from [1, p. 56]

Pressure decreases across the turbine while some of the thermal power (enthalpy times mass flow rate) is converted to shaft power. Again, design pressure ratio, mass flow, and efficiency are specified, and a user-supplied turbine map is scaled (if necessary) to ensure that the design conditions match the design conditions for the map. This map is then used in calculations of 'off-design' performance. The calculations of output pressure ratio $\left(\Pi_t = \frac{P_{in}}{P_{out}}\right)$, enthalpy, and power required are determined the same way as in the compressor except for the fact that pressure and enthalpy decrease:

$$P_{T,out} = P_{T,in}/\Pi_t \tag{13}$$

The exhaust enthalpy ($h_{T,out}$) is determined using the (1) turbine efficiency (η_t) as specified or determined from an operating map, (2) the specific enthalpy assuming

isentropic expansion (h_s) and, (3) the total specific enthalpy of the flow into the system ($h_{T,in}$), as shown in Equation (14):

$$h_{T,out} = h_{T,in} - (h_s - h_{T,in})\eta_t \tag{14}$$

The power extracted onto the shaft is found from Equation (15):

$$\dot{W}_t = \dot{m}(h_{T,in} - h_{T,out}) \tag{15}$$

8.1.5 Nozzle

The NozzleNASA NPSS element is used to calculate the thrust produced by the expanding turbine exhaust as illustrated below.

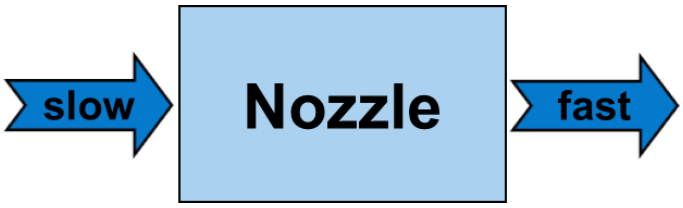

Figure 20: Nozzle component diagram, reproduced from [1, p. 60]

The element can model converging or converging-diverging nozzles. In on-design mode, the nozzle throat area is set to create choked flow for the mass flow rate provided at the entrance. In off-design mode, instead of changing the nozzle geometry, the mass flow rate must be altered in some way to maintain choked flow through the throat. This can be accomplished by changing the airflow rate through the entire system as done in this work, or by bleeding air into or out of the nozzle flow path.

8.1.6 Shaft

In a gas turbine, compressors and turbines (often in multiple sets or “spools” in larger engines) are connected by shafts to permit the turbines to drive the compressors. The built-in Shaft NPSS model, depicted generally in Figure 21, varies the rotational velocity of these and any other connected components until the net torque on the shaft from all connected sources is zero in order to achieve steady-state operation.

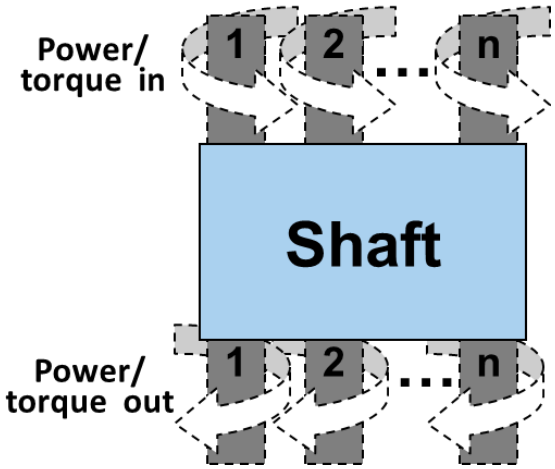

Figure 21: Shaft component diagram, reproduced from [1, p. 62]

Other shaft-connected components in this work include bypass fans and mechanical electricity generating equipment.

8.1.7 Overall GT Model

While many specific GT model configurations of varying complexity may be created (see Figure 33 for a more complicated case) the relatively simple model used to represent the small turbojet engine (AMT Olympus HP) to be used in the bench-

scale system is shown in Figure 22. It is a single-spool turbojet with no bleeds or fan bypass. Air flows from inlet to compressor, is heated via combustion with fuel, and expands through the turbine and the nozzle to produce thrust.

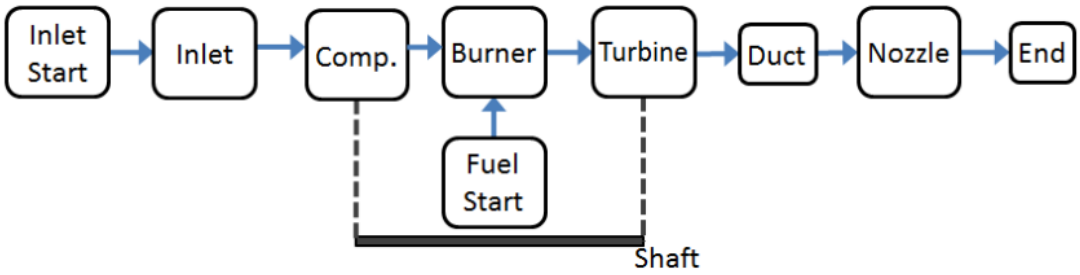

Figure 22: NPSS Schematic for AMT Olympus High Power. Reproduced from [62, p. 38]

The elements appearing in Figure 22 but not previously described are the inlet start, fuel start, duct, and flow end elements. The inlet start supplies the environmental information such as ambient pressure, temperature, density, composition, and flow speed. The fuel start provides similar information about fuel injected into the combustor. Ducts pass flow information between components and may have physical characteristics with implications for size or mass modeling. Additionally, pressure and temperature losses may be applied to the flow when passing through as defined by the user. In this work, those losses are set to be fractional pressure losses and heat loss rates in each duct, though more complicated functions such as Fanno or Rayleigh flow are also possible to implement. Finally, the flow end element terminates all fluid flow paths in the NPSS modeling system.

8.2 Reformer Model

Catalytic Partial Oxidation (CPOx) is one strategy for converting (or reforming) larger hydrocarbon molecules into mixtures of H_2 and CO (called syngas) that are suitable for consumption by the SOFC. This is achieved by passing a rich fuel/air mixture over an alumina foam catalyst that promotes incomplete oxidation of the fuel to CO + H_2 at low temperature with very little production of H_2O. Catalytic partial oxidation is advantageous in aircraft applications because it does not require water (unlike steam reformation). Disadvantages are susceptibility to coking and catalyst poisoning by sulfur in the fuel. Recent work indicates that sulfur concentrations as large as 400 ppm in the fuel gas may be acceptable (yielding stable, though suboptimal operation) [72, p. 97] though effects are observed down to as low as 50ppb.[1] By comparison, aviation fuels tend to have sulfur levels of approximately 500ppm.[73, p. 447] From a practical perspective, sulfur levels are to be minimized as much as possible within the constraints of fuel supply, mass, and expense. NPSS does not offer a standard CPOx component so it was necessary to develop one ourselves. This was done in previous work by Waters [1, Ch. 2.3.3] so only a brief description is presented here.

[1] Note that in this case, the value applies not to the fuel but the reformate after partial combustion to syngas [99, p. 5].

The CPOx model splits incoming air into bypass and CPOx streams as illustrated in Figure 23. Fuel is added to the CPOx air stream prior to the reaction zone ("reax zone" in Figure 23)

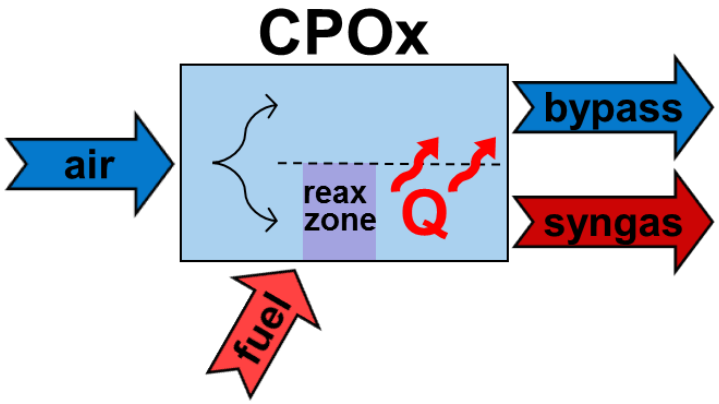

Figure 23: Catalytic Partial Oxidation Reactor component diagram, reproduced from [1, p. 68]

The reaction zone is modeled as a channel divided into a number of flow-wise segments in which pressure drop, heat loss, enthalpy, temperature, and species concentrations are calculated by enforcing conservation of mass, momentum, and energy in each segment and assuming that the mixture exiting each segment is in chemical equilibrium. Some heat produced in the CPOx is transferred into the bypass flow. The system is solved by iterating until the initial air-fuel ratio equals the minimum fuel/air ratio required to avoid soot formation (coking) which is, in turn, is determined from the exit temperature of the last segment of the CPOx in conjunction with the pressure in accordance with Le Chatelier's principle.[17]

8.3 Fuel Cell Inlet Model

The fuel cell inlet component reduces the temperature difference between the gas streams entering the anode and cathode sides of the fuel cell in order to minimize thermal stresses in the MEA. It is a necessary component in any practical fuel cell system. Functionally, the fuel cell inlet diverts a portion of the bypass air from the CPOx into the cathode channel for the SOFC, as well as carrying through the hot partially combusted (non-bypass) gases from the CPOx into the anode channel of the SOFC, as depicted in Figure 24. [1, Ch. 2.3.5]

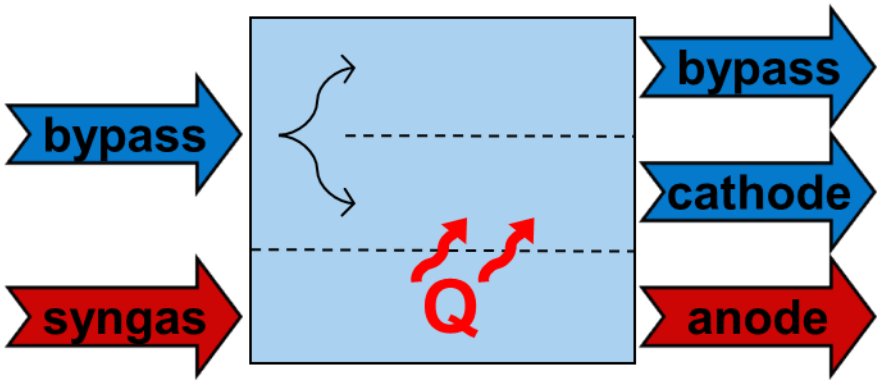

Figure 24: Fuel Cell Inlet component model, modified from [1, p. 90]

In the process, heat is transferred from the CPOx gases to the cathode channel air. The pressure drop uses a general correlation for non-circular ducts,[74] and a Nusselt number correlation for the convective heat transfer coefficient [75], both of which are also used in the similarly-shaped SOFC component. The inlet is further modeled akin to a heat exchanger, specifically using the effectiveness-NTU method described by Incroprera et. al. [76] This model has been updated by the author since

the prior work to properly calculate heat losses for each segment progressing linearly along the length of the inlet.

8.4 Solid Oxide Fuel Cell Model

8.4.1 Overall Configuration

The fuel cell model used in this work is identical to that developed by Waters [1, Ch. 2.3.4], except for variations in the specific geometry of particular GT-SOFC designs which depend on the scenario of interest and the choice of which variables are designated as dependent and independent for the solver. Specific properties that change include the SOFC length, fuel flow rate, insulation thickness, and number of membrane electrode assembly units per SOFC "stack". The physical structure of the fuel cell consists of annular rings (Figure 25) arranged around a cylindrical engine section. Calculations are simplified by assuming that the diameters of the rings are much larger than the width of the flow passages and thus can be approximated as flat. Each stack is assumed to be a certain number (N_{rep}) of repeating units thick. Each repeating unit (illustrated with dotted lines in the figure) consists of an anode channel with half cathode channels above and below that are separated from the anode channel by MEAs. the symmetry of the annular configuration simplifies heat transfer calculations because heat only flows through the top and bottom of the stack and the boundary conditions on the left and right edges of the stack can be assumed to be the same. As a result, the calculations need only be performed for a single stack.

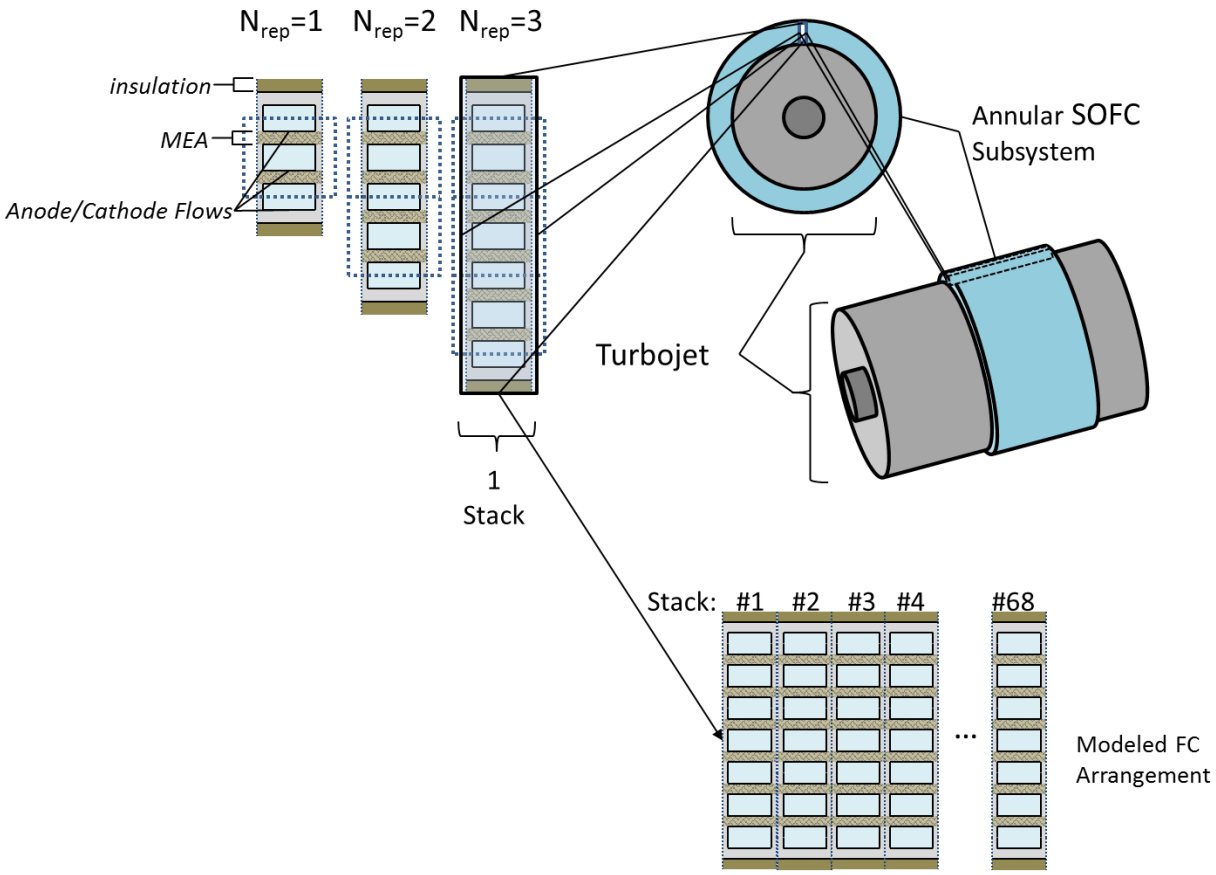

Figure 25. Assumed layout of CPOx/SOFC Components.

The fuel cell model is like the reformer's in that it is broken into a series of segments in the flow direction (see section 3.4.3.2 below). Pressure drop, heat loss, diffusion of O^{2-} ions through the MEA, and equilibrium (this time also considering reactions on the anode and cathode surfaces) are computed in each segment.

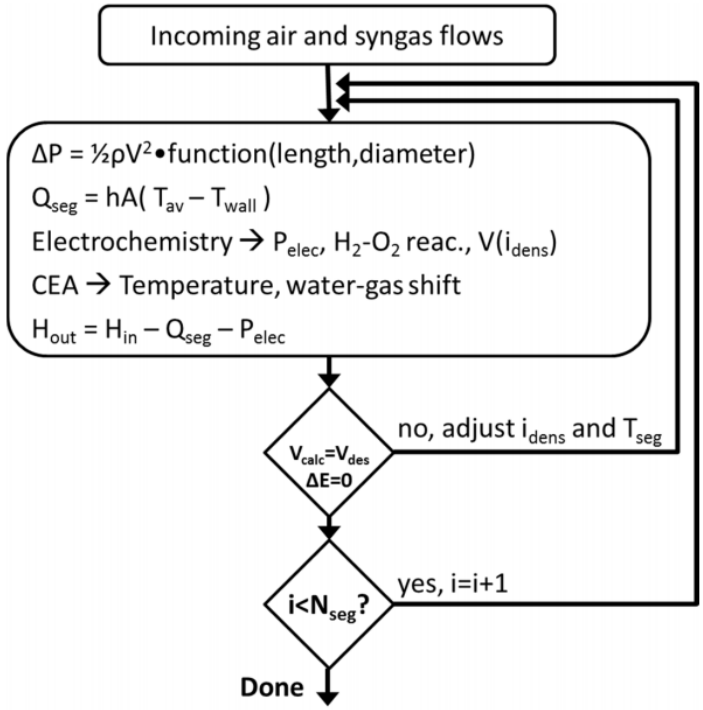

Figure 26: Iterative process for the SOFC model. Reproduced from [1, p. 78]

A diagram illustrating the iterative solution process is provided in Figure 26. The solver finds the appropriate current density for a given voltage, or alternately, the appropriate voltage for a chosen current density (though in our studies we have generally chosen the former case). A Newton-Raphson method is used for iteration as many of the relations between the overpotentials and the cell current density are implicit. Solutions are found as follows:

(1) Generate the global electrochemical reaction that can occur based on the present fuel and oxidants.

(2) Use this information to generate the Nernst potential and electron charge transfer of the cell.

(3) Assume a current-density target and use it to establish the rate of flow of various chemical species into and out of the anode and cathode to match the required number of electrons produced.

(4) Use the dusty gas model to determine the rate of O^{2-} conduction through the MEA.

(5) Use the species concentrations in the anode and cathode flows to generate concentration overpotentials at both electrodes.

(6) Use the Butler-Volmer equation to infer the activation overpotentials for both anode and cathode.

(7) Evaluate the ohmic and interface overpotentials.

(8) Calculate the leakage overpotential from a known initial leakage rate at the open circuit condition. The unknown i_{max} value is found by iteration.

(9) Determine the final cell voltage by summing the overpotentials. If a specific voltage is sought, the assumed current density is lowered or raised, depending on whether the voltage found initially was too low or too high.

The iterative process is repeated for flow down a channel (into the page of Figure 25) where the channel is divided into a number of segments as shown in Figure 27.

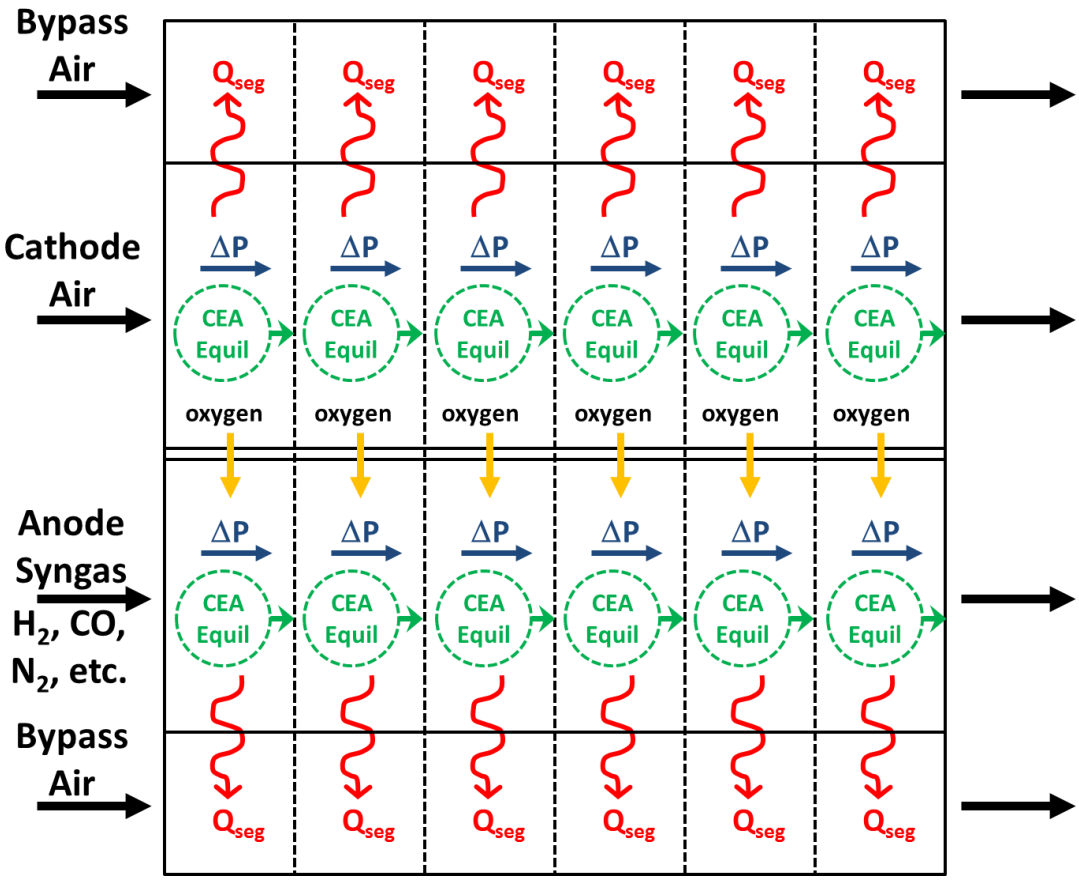

Figure 27: Illustration of down-the-channel iteration in the SOFC model, reproduced from [1, p. 77]

Eight segments have been shown to be an effective tradeoff between calculation time and accuracy (less than 0.5% deviation of flow properties from those determined with a spatial resolution of 1024 segments). [1, p. 156]

8.4.2 Electrochemistry

The electrochemical model of the SOFC is largely based on the work of Zhu and Kee [77]–[85] which provides a framework for the function and performance of a fuel cell membrane electrode assembly with arbitrary flow characteristics for the

anode and cathode. It can also account for proton or oxygen-ion conducting electrolytes as well as a variety of geometries. The model is based on generating the operating cell potential as a function of the reversible (Nernst) potential, and possible overpotentials including the concentration, activation, and ohmic losses. The model also accounts for overpotentials due to (1) contact resistances at the various material boundaries (e.g. between current collector and anode material) via η_{inter} and (2) the leakage of electric current through the ideally-insulative electrolyte material via η_{leak}. The overall equation is shown in Eqn. (16).

$$E_{cell} = E_{nernst} - \eta_{conc,a} - \eta_{conc,c} - \eta_{ohm} - \eta_{act,a} - \eta_{act,c} \tag{16}$$

In the model, concentration overpotentials $\eta_{conc,a}$ and $\eta_{conc,c}$ are determined implicitly in the Nernst potential by determining the species concentrations at each electrode interface. To do so, Zhu and Kee apply the dusty-gas model (DGM), taking account of the primary contributor to the overpotential which is specifically transport of gaseous species through the porous electrodes (usually porous by design to maximize reactive surface area). The DGM assumes that a pore wall is made up of large fixed particles in space with which gases interact. The model accounts for molecular diffusion, Knudsen diffusion, and viscous flow.

The Butler-Volmer equation (Eqn. (17)) is used to determine activation overpotentials η_{act}, and is solved by numerical iteration.

$$i_e = i_0 \left[\exp\left(\alpha_a \frac{n_e^{BV} F \eta_{act,a}}{RT} \right) - \exp\left(\alpha_c \frac{n_e^{BV} F \eta_{act,c}}{RT} \right) \right] \tag{17}$$

Ohmic resistance - essentially the losses due to the inherent ‘wire’ resistance experienced by charge flowing through the electrodes and electrolyte - is linear with respect to current and the total resistance from all sources. The total resistance is calculated from the electrode inherent resistance, added to the ion conductivity through the electrolyte. Ion conductivity is the primary source of resistance and is a function of temperature and the activation energy of ionic transport through the specific electrolyte.

More detailed information about the implementation of the SOFC electrochemistry model is available elsewhere. [1, Ch. 2.3.4], [17]

8.4.3 Heat Transfer and Pressure Loss

Broadly, heat transfer (and thus stack temperature) is controlled by the thickness of the layer of insulation (t_{ins}) on the top and bottom edges of the stack. The bypass air stream from the fuel cell inlet passes around the outside of the annular rings (with the insulation in between) allowing for cooling of the SOFC. Internal to the SOFC, both the heat transfer and pressure loss coefficient calculations are based on work by Muzychka and Yovanovich for non-circular ducts. [74], [75]

The heat transfer method is a proposed general model that combines the results of fully developed flow, Graetz flow, and laminar boundary flow regimes, yielding an expression for the average Nusselt number for uniform temperature walls and set for rectangular ducts.[75] The actual heat loss calculations are performed by solving a

discrete finite volume problem over repeating sections of the fuel cell channels as shown in Figure 28.

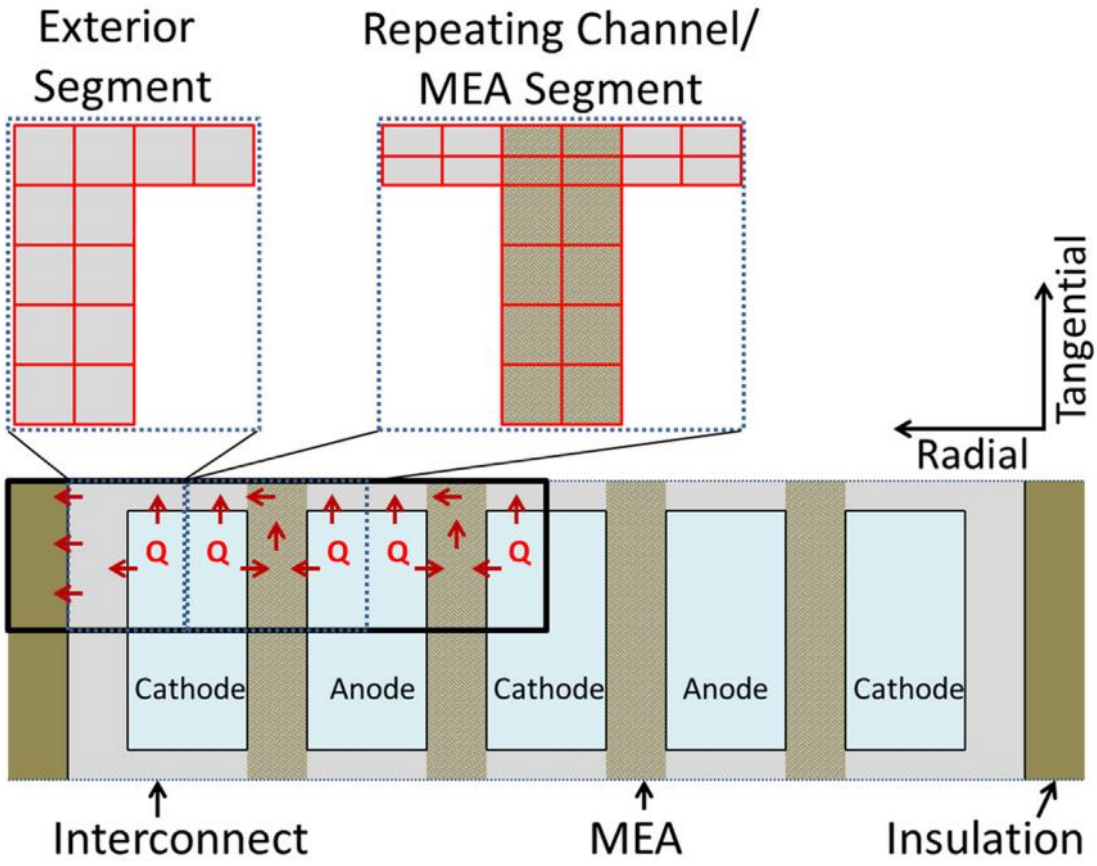

Figure 28: Discretization scheme for heat transfer calculations. Reproduced from [17]

Heat transfer from the channel flow to the wall surfaces applies the Nusselt number as determined previously via forced convection. Further heat transfer details may be found in both section 2.3.4 and Appendix D of Waters.[1]

8.5 Fuel Cell Assembly Model

The NPSS model of the CPOx/SOFC assembly shown in Figure 29 includes all of the fuel cell related components: (1) a splitter to divert some of the flow exiting the

compressor to the CPOx/SOFC assembly (CPOx) (2) a catalytic partial oxidation (CPOx) reformer (3) a fuel cell inlet that splits the airflow into cathode and cooling (bypass) flows in addition to pre-heating the anode flow to reduce thermal gradients at the SOFC entrance, (4) the SOFC itself, and (5) a plenum (combiner) that recombines the anode, cathode, and bypass flows before returning to the combustor. The latter allows unburned fuel and unused enthalpy from the SOFC exhaust to be harvested in the turbine.

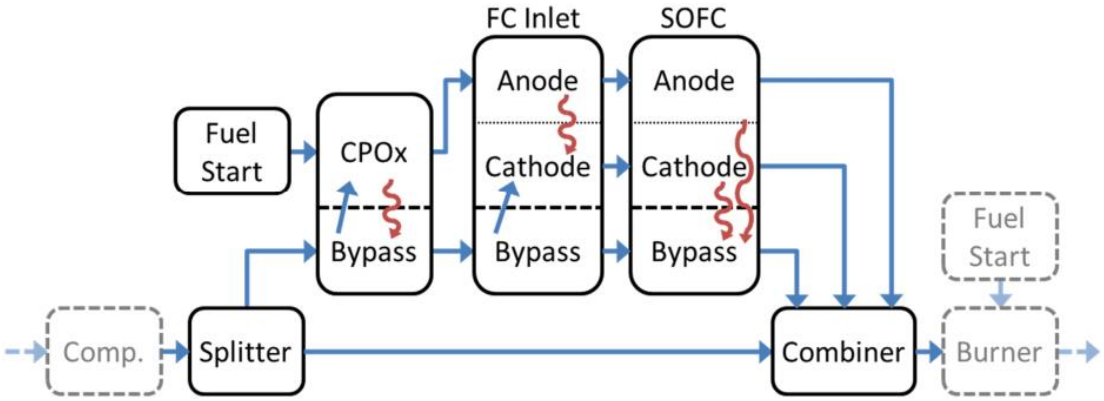

Figure 29: NPSS schematic for CPOx/SOFC Assembly. Reproduced from [1, p. 104]

The blue arrows in Figure 29 show fluid flows, while red curves show flows of heat. The ratio of cathode to bypass air flow rate is adjusted to avoid soot formation in the CPOx.

Several elements in Figure 29 have not been previously described including the Fuel Start, Splitter, and Combiner. The Fuel Start is a standard NPSS component which defines the fuel properties supplied to the system including initial extrinsic flow properties.[71, p. (2-63)] The Splitter (specifically the built-in SplitterNASA

element as described in [71, p. (2-105)]) divides a fluid flow according to a given bypass ratio, while maintaining the intrinsic properties (density, temperature, pressure, etc.) of the flow to each output. The custom Combiner element described by Waters [1, p. 67] collects and combines four fluid flows into a single flow, calculating their combined equilibrium state before passing to the next component.

8.6 Overall GT-SOFC Model

Figure 30 shows the NPSS model of the integrated GT-SOFC system.

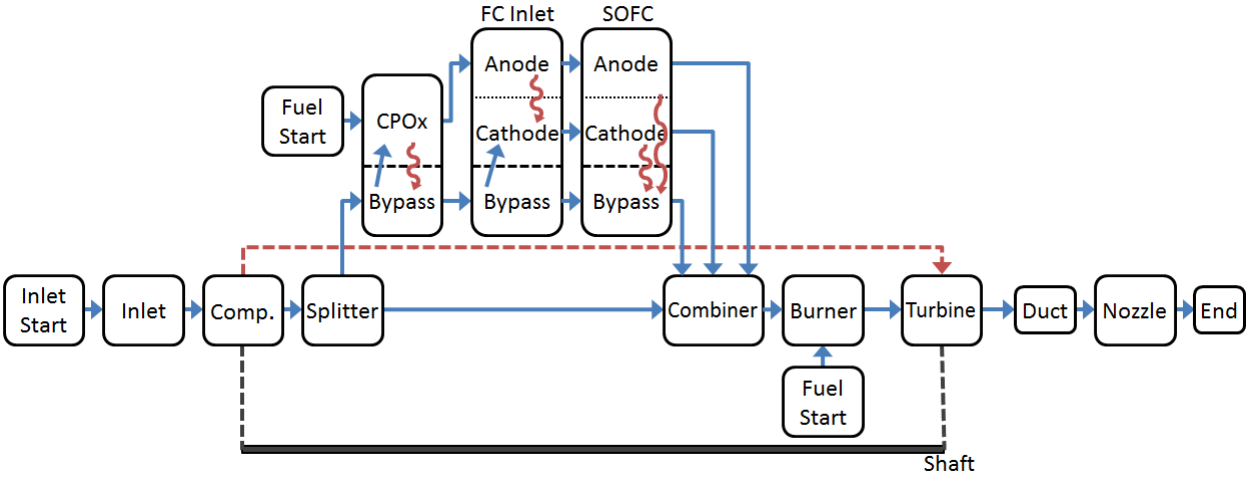

Figure 30. Schematic of NPSS model of Turbojet GT-SOFC. Reproduced from [4]

The corresponding physical layout of the fuel cell subsystem is broadly illustrated in Figure 31.

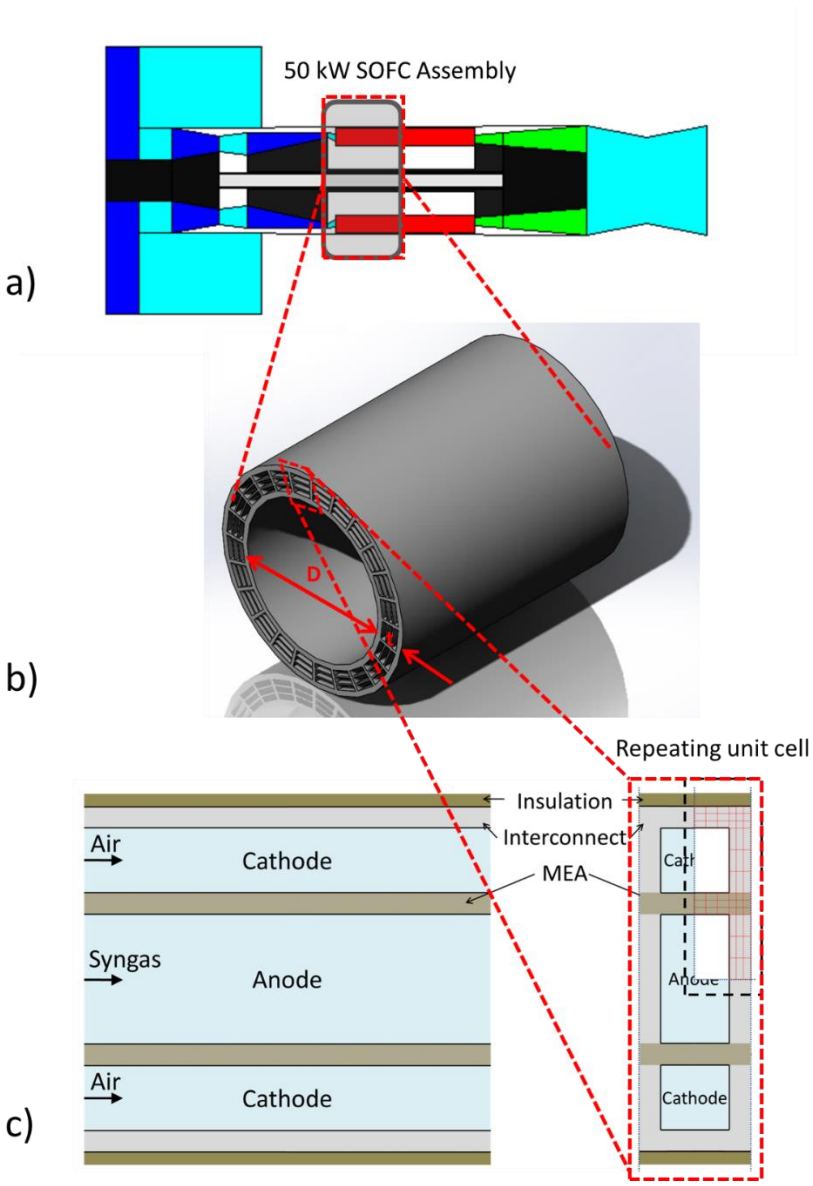

Figure 31: CPOX/SOFC Assembly layout, including a) sizing and overall placement on a high-BPR turbofan, b) a diagram of the annular assembly with channels illustrated, and c) a diagram of the repeating unit cell head-on (right) and down the channel (left)

Here, stacks of repeating units of fuel cell channels are notionally arranged circumferentially around the engine. Note that this geometry is not explicit in the model as temperature gradients between the turbine and fuel cell subsystems are not considered.

Furthermore, while the general size is consistent with the notional arrangement, the analysis is performed under the assumption that all of the stacks are flat, essentially "unwrapped" from the engine—which can be less reasonable an assumption for a small laboratory-scale gas turbine such as the AMT Olympus [61], [62] than it is for a larger-diameter HALE UAV or passenger jet.

8.7 Mass Estimation

While the thermodynamic benefits of an integrated GT-SOFC are clear in ground applications, mass and volume are additional key factors for evaluating the usefulness and performance in aircraft. Should an efficient integrated GT-SOFC be too large or heavy, specific power and power density for the aircraft overall will fall, lowering performance by increasing profile drag or increasing the required angle of attack to counteract the larger system mass. As such, accurate modeling of the mass and volume of the gas turbine, SOFC assembly, and supporting hardware is an essential extra step in determining the viability of a GT-SOFC system for aircraft. [1, Ch. 4] This section will expand on the models used for each component. Note that these models are not relevant to the design of the lab-scale model presented in Chapter 10.1, since it is not intended to fly.

8.7.1 Gas Turbine

The gas turbine mass is determined using a model based on Onat and Klees [86] and Sanghi et. al., [87] which generates a system mass by determining the sizing

requirements piece by piece based on the operating conditions of the engine model state. The full model implemented (here applied to mass and aerodynamic drag analysis) is identical to that used by Waters, which has been validated to be accurate to within 14% for a range of known GT engines and 10% for American GT engines. [1, Ch. 4.2] Note that mass and volume estimation is not relevant for the analysis lab-scale model based on the AMT Olympus turbojet, though in such a case, the mass model of the GT would be simply the mass of the Olympus as provided.

8.7.2 Fuel Cell

The CPOx/SOFC assembly mass is determined in a similarly piecewise fashion to that of the gas turbine. However, often set values for the dimensions of the system and channel are chosen ahead of the calculation, rather than being determined by the system operating state, as described in section 7.2. Again, the full mass/volume model is identical to the one employed by Waters. [1, Ch. 4.3] A notable design consideration is a mass-advantage to increasing radial stack size over adding entirely new stacks due to the mass of the interconnect wall and insulation.

8.7.3 Additional Hardware

In addition to the GT and CPOX/SOFC assembly, there is a duct that contains the assembly and mounting bolts that support the weight of the assembly added to the engine. The size of the duct is set to be large enough to accommodate the length and area of the SOFC, including the cooling bypass flow. The area (A_{duct}) is represented

by Equation (18). A_{bp} is the area of the bypass duct, in turn determined by the cooling air mass flow rate $\dot{m}_{bp}$, the density (ρ_{bp}) of air diverted from the compressor, and the design bypass flow velocity (v_{bp}), which is set in this work to be 100 m/s. A_{SOFC} is the area of the fuel cell anode and cathode ducts, determined by a the number of fuel cell anode/cathode channel units (N_{FC}) multiplied by the area of a single SOFC stack unit including walls. The resulting inner diameter (D_i) and outer diameter (D_o) of the duct are set by the diameter of the engine (set by the engine operating requirements) and the area of the duct (as shown in Equation (19)) respectively.

$$A_{duct} = A_{bp} + A_{SOFC} = \frac{\dot{m}_{bp}}{\rho_{bp} v_{bp}} + N_{FC} A_{FC,unit} \tag{18}$$

$$D_o = \sqrt{D_i^2 + \frac{4}{\pi} A_{duct}} \tag{19}$$

In one variant of the external aerodynamic model (see chapter 9.1 and Figure 35 in particular), the duct winds back once, doubling its radial area. In that case the second equation becomes:

$$D_o = \sqrt{D_i^2 + \frac{8}{\pi} A_{duct}} \tag{20}$$

The mass of this duct depends on a wall thickness and material density that are specified in the model. Again, the model is identical to the one employed by Waters. [1, Ch. 4.3.4]

9 Role of Aerodynamic Drag

9.1 Vehicle Drag Polar

The drag polar will be used to relate increases in engine weight (due to the additional fuel cell components) to increases in drag. Two vehicles will be considered: a high-altitude long endurance (HALE) aircraft based on the RQ-4 Global Hawk and a regional transport jet (RTJ). Specifications for both aircraft are available in prior work [1, p. 140], [17] and reproduced in Table 4.

Table 4: Specifications of Reference Aircraft. Reproduced from [17]

Parameter	HALE	RTJ	Units
Powerplant			
Rated thrust	35.0 x 1 eng.	35.0 x 2 eng.	kN
Weights			
Loaded airframe*	7,000	15,000	kg
Fuel capacity	7,500	4,000	kg
Wings			
Wingspan, b	40.0	20.0	m
Planform area, S	64.0	50.0	m^2
Aspect ratio, AR	25.0	8.0	
Cruise			
Altitude	16.8	10.7	km
Mach	0.5	0.8	
Drag polar			
C_{Dmin}	0.0195	0.016	
K	0.01725	0.09	
C_{Lmin}	0.3	0.1	

*Loaded airframe weight includes payload but not fuel or engines

The drag polar takes the form of Equation (21) found as Equation 12.5 in Raymer.[88, p. 263]

$$C_D = C_{Dmin} + K(C_L - C_{Lmin})^2 \quad (21)$$

Here C_D is the overall drag coefficient, K is the dynamic drag coefficient, $C_{L,min}$ is the static lift coefficient, and $C_{D,min}$ is the static drag coefficient at $C_{L,min}$.

The lift and drag coefficients are defined in Equations (22) and (23)

$$C_L = \frac{L}{qS} \quad (22)$$

$$C_D = \frac{D}{qS} \quad (23)$$

,

Here L is the lift force, S is the wing area, and the free stream dynamic pressure is $q = \rho_{air} v^2/2$ where ρ_{air} is the air density and v is the flight velocity. The additional weight of the fuel cell components increases the lift (L) required to achieve level flight and thus increases drag through Equations (21), (22), and (23). Figure 32 shows drag polar plots for the HALE and RTJ aircraft considered here.

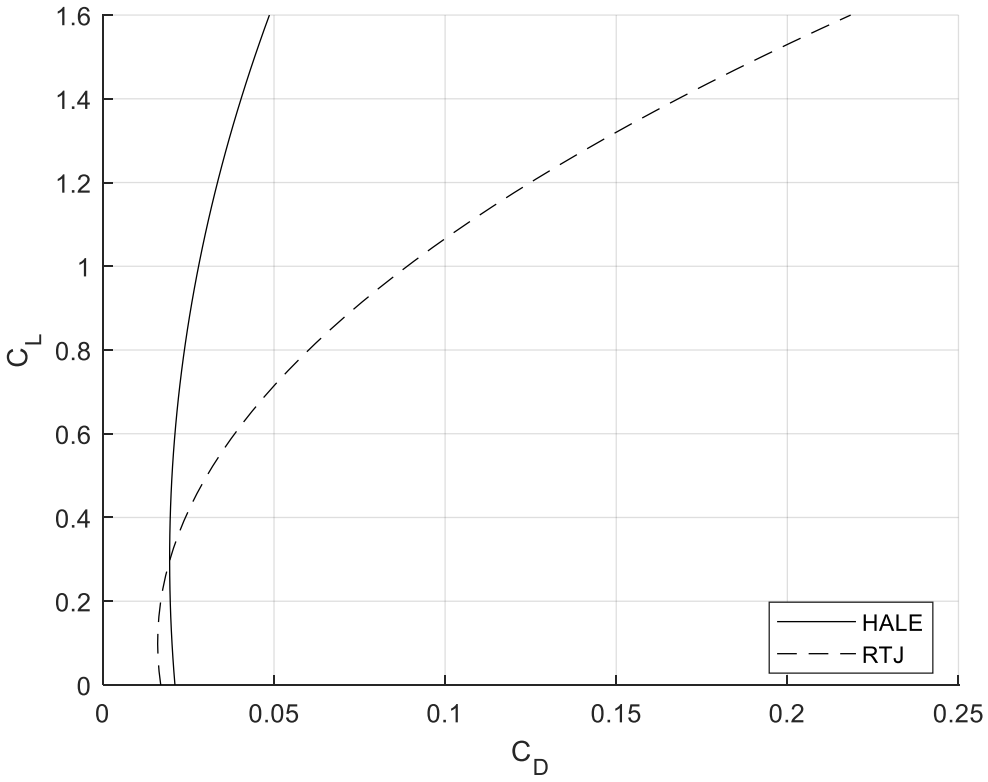

Figure 32: Drag Polar plots of High-Altitude Long-Endurance (HALE) and Regional Transport Jet (RTJ) aircraft

9.2 NPSS models for HALE and RTJ aircraft

The HALE and RTJ aircraft are equipped with turbofan engines so the NPSS model discussed in section 8.6 is extended to account for the additional turbomachinery as illustrated below in Figure 33.

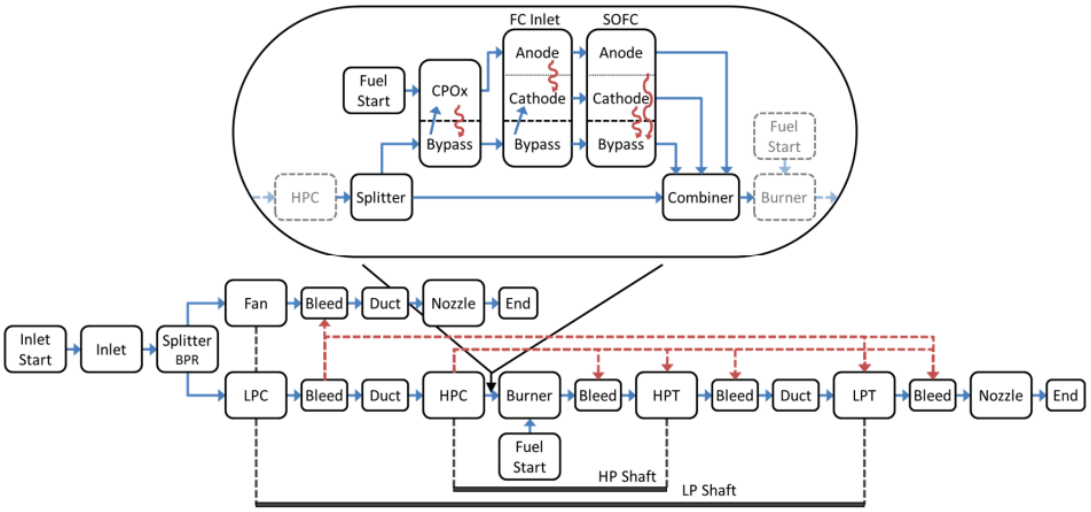

Figure 33: NPSS Schematic of a high bypass ratio turbofan GT-SOFC. Reproduced from [1, p. 108]

The fuel cell subsystem components and general integration scheme are the same as discussed previously. New components are high- and low-pressure compressor and turbine spools (HPC/HPT and LPC/LPT) and a fan implemented as a Compressor component on the low-pressure spool. Also present, but not currently utilized, are several standard Bleed components that combine or separate flows while maintaining mass and energy conservation and allowing for heat loss to the environment, allowing for off-design controls in future work.[1, p. 51], [71, p. (2-22)]

9.3 Engine Pylon Drag Model

The fuel cell components also increase the physical size of the engine which, in pylon-mounted configurations, will lead to additional (profile) drag that is not accounted for in the drag polar. This drag must be added to the induced drag (from the drag polar) to get the total additional drag on the vehicle due to the additional fuel

cell components. Waters placed the additional mass/volume of the SOFC system placed in an annular ring around the outside of the engine as illustrated in Figure 34 [1, Ch. 7.3]. In doing so, he applied the following drag model added drag components on top of the standard drag polar of the given aircraft profile (here a HALE aircraft similar to the Global Hawk, and a regional transport jet (RTJ)).

The drag model assumes an annular configuration of the CPOx/SOFC assembly wrapping around the combustor section of the gas turbine as shown in Figure 34. Note that for this turbofan configuration, the core of the gas turbine is largely cylindrical. The assembly sits around the outside of the engine core protruding a distance (δ)) into the secondary bypass fan flow. The assembly exhausts into the combustor 20 cm downstream axially. Fairings upstream and downstream of the protrusion smooth the flow of air past the assembly. The minimum length of the assembly is constrained by the fixed compressor discharge plane and combustor injection point.

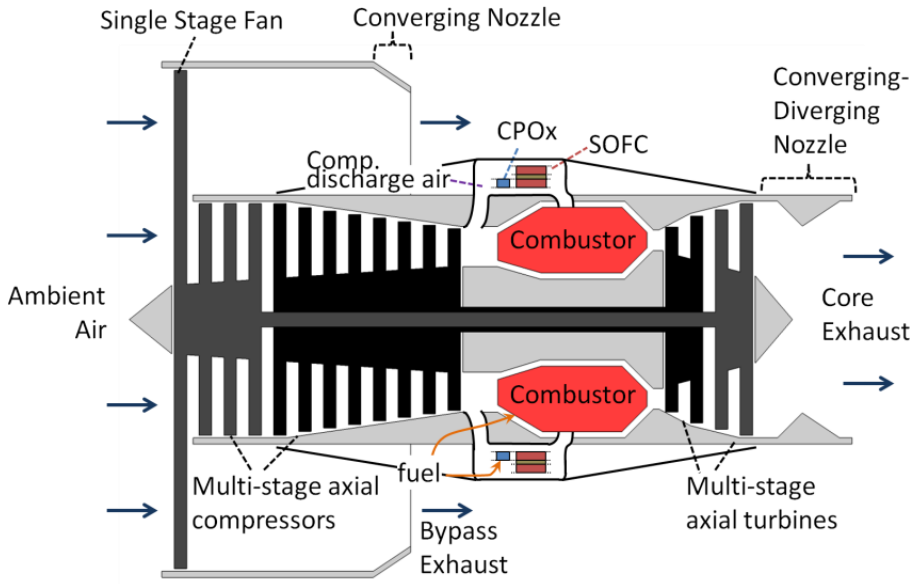

Figure 34: Configuration and drag model of pylon-mounted CPOx/SOFC assembly, modified from [1, p. 141]

Variations on this configuration include changing the length of the fuel cell channels and changing the profile of the gas turbine involved. The axial length of the fuel cell is allowed to increase by creating a single turn inward along the axial length of the CPOx/SOFC assembly such that the flow may return to the same point of injection into the combustor, as depicted in Figure 35. The outer diameter of the assembly discussed in section 8.7.3 requires the previously discussed Equation (20) as the area taken up by the assembly ducts is doubled by the turn-back.

The flow area changes substantially in high pressure ratio engines so that a substantial fraction of the CPOx/SOFC assembly may be at least partially contained within the profile of the compressor (see Figure 35). Thus, profile drag losses are not incurred until the CPOx/SOFC reaches sufficient size to protrude into the bypass flow.

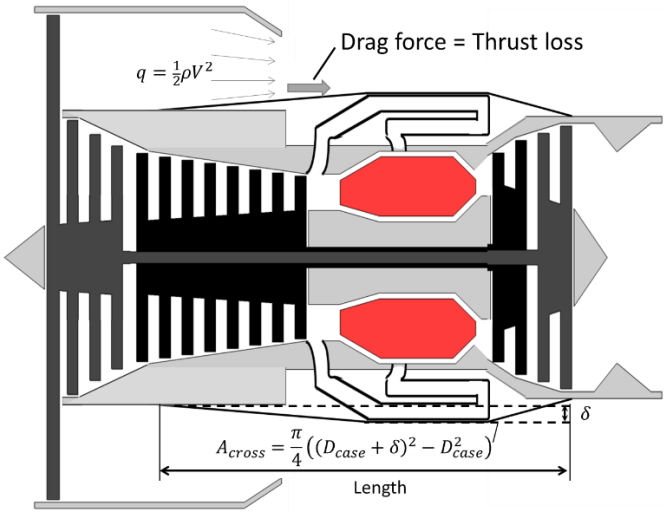

Figure 35: Illustration of the configuration for the GT-SOFC using "narrow waist" GT and variable length CPOx/SOFC assembly by utilizing a turn-back, modified from [1, p. 143]

The drag of the protrusion of the CPOx-SOFC components into the flow follows Raymer [88, Ch. 12.5], which considers the drag force (D) for a specific component as it is related to local flow dynamic pressure (q), skin friction coefficient (C_f), pressure drag form factor (FF) and wetted area (S_{wet}) as in equation (24).

$$D = qS_{wet}C_fFF \tag{24}$$

The flow exiting the turbofan is assumed to be turbulent, while C_f is a function of the local flow Reynolds number (Re) and Mach number (M) as in Equation (25):

$$C_f = \frac{0.455}{(\log_{10} Re)^{2.58}(1 + 0.144M^2)^{0.65}} \tag{25}$$

The pressure drag form factor (FF) depends on the 'fineness' $f = l/\sqrt{(4/\pi)A_{cross}}$ of the fuel cell duct as in Equation (26), where (l) is defined as the length and A_{cross} as

the profile cross section of the GT-SOFC core (not counting secondary flow channels, i.e. fan flow).

$$FF = 1 + 60/f^3 + f/400 \quad (26)$$

The profile drag force is added to the induced drag force from the vehicle drag polar to estimate the overall thrust required to maintain level flight.

9.4 Fuel Cell Configurations

Since the electric power generated is assumed to be applied to secondary purposes rather than propulsion, any increase in electrical demand will increase drag and thus the fuel flow rate.

Recalling the model of the SOFC described in section 8.4.1, there are several ways to increase electrical generation capacity. First, we can simply change the number of SOFC rings around the GT which is equivalent to changing the number of "stacks" in any other fuel cell scenario. From a real-world perspective, this is the most common method as generally a single stack size is designed and manufactured. An alternative is to vary the size of the stack itself. This is less convenient/economical to manufacture but is more mass/volume efficient while also changing the stack's heat transfer properties. Both approaches increase the radial size of the CPOx/SOFC assembly leading to more drag.

Another possibility is to grow the cell axially instead of radially as shown in Figure 35. This allows the length to vary up to the physical limits of the GT core whether that is the end of the nozzle, or of the "narrow waist" of some engines.

Extending the fuel cell axially does not directly increase the profile drag in this model (though it does increase the assembly mass), until the physical length limit (here taken to be the end of the low-pressure turbine, or the end of the narrowed waist in very-high bypass ratio scenarios) is reached and another SOFC stack must be added to increase power generation.

For the same flows of fuel and air, this case provides longer channels for reactions to occur, whereas building out radially splits the flow into additional channels, such that fuel and oxidizer travels down each more slowly. In each case, we are concerned with determining the range of performance (including electrical generation) that is possible for the GT-SOFC. In addition, we are interested in identifying the most important GT-SOFC design parameters. This is accomplished by performing a sensitivity analysis. While Waters conducted performance [1, Ch. 7.3] and sensitivity analyses [1, p. 160], [17] of similar integrations using a similar overall system model, Waters' analysis did not carefully investigate the effects of profile drag. This is something we will do here.

9.5 Mechanical Generator Model

The baseline of comparison for the fuel cell is a mechanical generator driven by the high-pressure spool of the turbomachinery. The generator is modeled by extracting a specified amount of power from the high-pressure Shaft element in the model via the built-in variable for horse-power extracted 'HPX'.[71, p. (2-96)] The mechanical power extracted is assumed to be converted to electricity with 100%

efficiency. The generator is assumed to cause no additional profile-drag by being held fully within the body of the turbofan hub (see Figure 3), but the generator does apply a mass penalty that becomes a part of the total aircraft mass in the drag polar. The mass of the mechanical generator is determined from a given specific power of the generator, here bracketed between two cases of 1kW/kg and 5kW/kg, as have been used in prior work[1, Ch. 7.3.2], [17] and in a similar range to the survey of electric motors shown by Ng and Datta in Figure 24 of [14].

Applying this to the HALE GT model operating in cruise conditions (M=0.5 @ 55kft) and solving for progressively-higher levels of power extraction from the shaft yields the plot of fuel consumption vs. electric power fraction presented in Figure 36. The limitation on power extraction in both cases is determined by the turbine inlet temperature (TIT) limit which, in turn, is set by the materials and design of the turbine. Here it is assumed to be 1600K.

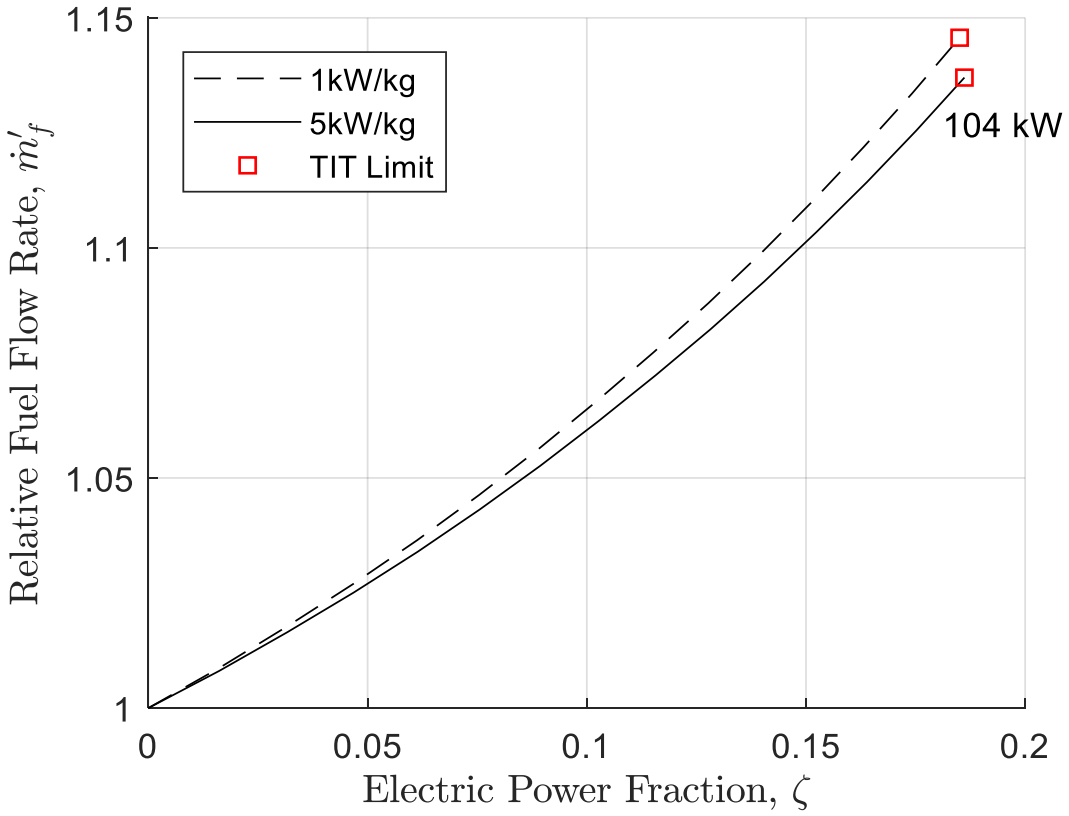

Figure 36: Mechanical Generator Performance on HALE aircraft at cruise conditions (M=0.5 @ 55kft) Maximum electric power output is 104.4 kW and occurs when the combustor exit temperature reaches the turbine inlet temperature limit of 1600K.

The effect of the change in specific power on relative fuel flow rate is relatively small (~1% variation at $\zeta = 15\%$ for a five-fold difference in specific power) as the specific power of any generator is much greater than that of a fuel cell. As noted in previous work, the specific power of the gas turbine itself drops substantially with altitude.[1, Ch. 7.3.5]

9.6 GT-SOFC Results

Both duct configurations have been considered when modeling the high bypass ratio turbofan in the HALE aircraft. To-scale layouts of the configurations are provided in Figure 37. The figure illustrates three cases, each building off a turbofan with a bypass ratio of 5 and an overall pressure ratio (OPR) of 24, operated at cruise conditions (M=0.5 @ 55kft). The yellow and bold-outlined annular section around the combustor section (red) in each diagram represents the reformer and fuel cell subsystems, designed to operate at a specific power level (50 kW and 250 kW are considered here) using a fixed value of $N_{rep} = 18$ in the fuel cell, with 186 units per stack (for a total width of 3.6 ft). Either the number of annular stacks (1-5) or the fuel cell length (0.2-1.48 meters) is varied to meet the required electrical load. The ranges allowed for each configuration are based on reasonable physical limits; in particular the axial length is required to fit between the compressor exhaust plane and the turbine exhaust plane using a single turn-back, while the radial growth is limited to the fan diameter of the turbofan engine which completely blocks the flow.

Other engines, including turbojets, low bypass ratio turbofans, and "narrow-waisted" (i.e. very high bypass ratio and/or pressure ratio) turbofans have all been evaluated previously at a number of conditions including takeoff and idling (sea-level-static conditions) as well as at varying altitudes and Mach numbers.[1, Ch. 7][17]

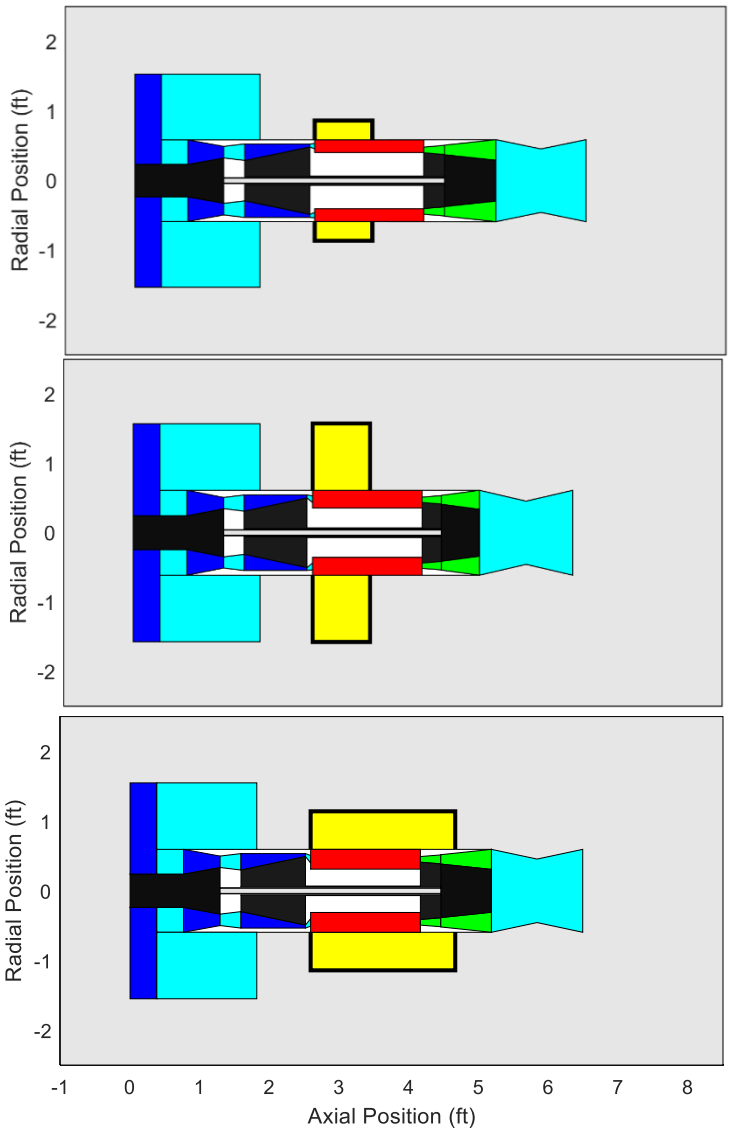

Figure 37: High bypass ratio engine profiles with 50 kW (top) and 250kW by either additional radial stacks (middle) or length-extension of one stack (bottom) CPOx/SOFC assembly profiles

In order to reach the engine profiles shown above, the 50kW solution (a single stack 20cm long) at top is taken as the starting point for either radial-growth through stack addition (middle) or growth in terms of length (bottom). The length-growth will also incur some radial growth in order to accommodate the turn-back and additional cooling bypass flow. The results are shown below in Figure 38. Note that the length-

growth results are shown as a continuous line (as theoretically any length along the line would be viable), whereas growth by stack-addition is shown by distinct points corresponding to each full stack being added to the assembly. Arrows indicate the configurations shown above, which are also considered later in the sensitivity analysis.

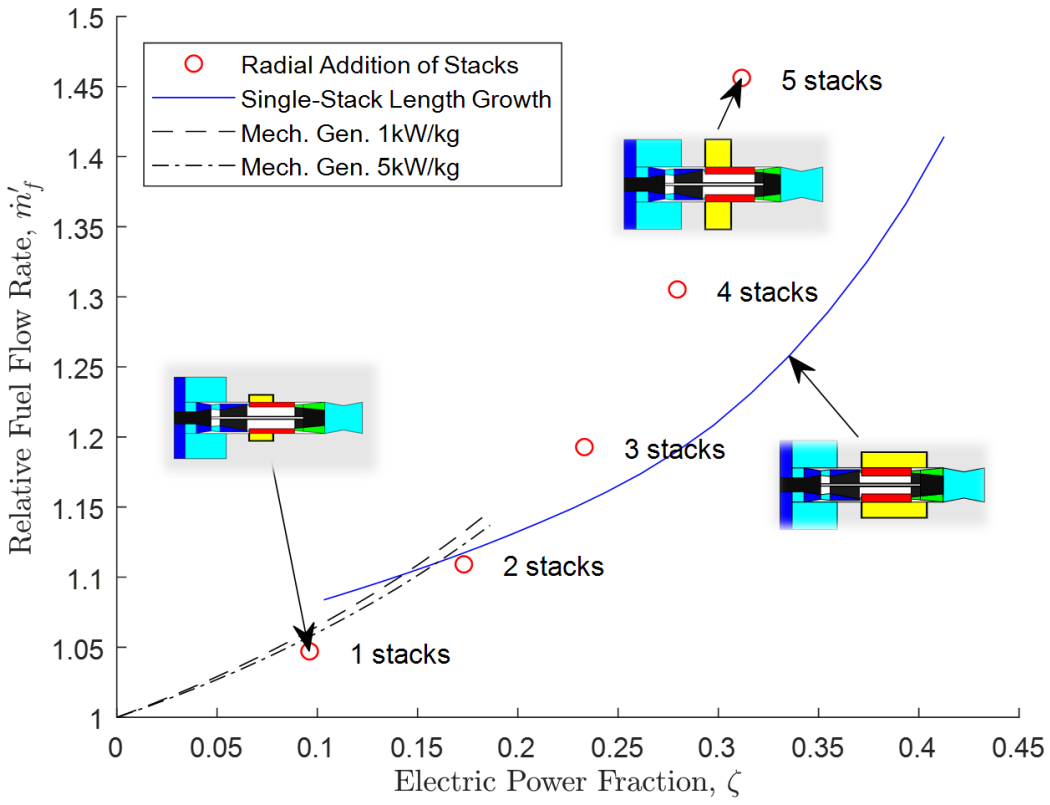

Figure 38: Length and Stack growth-type performance ranges, in comparison to mechanical generator performance.

Figure 38 shows that integrated GT-SOFCs regardless of configuration can access higher electric power fractions, and in some cases at lower relative fuel flow rates, than GT/mechanical-generator systems. The cases presented here show smaller

reductions in relative fuel flow rate than presented in prior work, reproduced in Figure 39, likely due to the stacked nature of the model; Figure 39 was generated by the addition of single SOFC units with and $N_{rep} = 1$ rather than 18, yielding an essentially continuous range of performance rather than an initial larger ~50kW assembly.

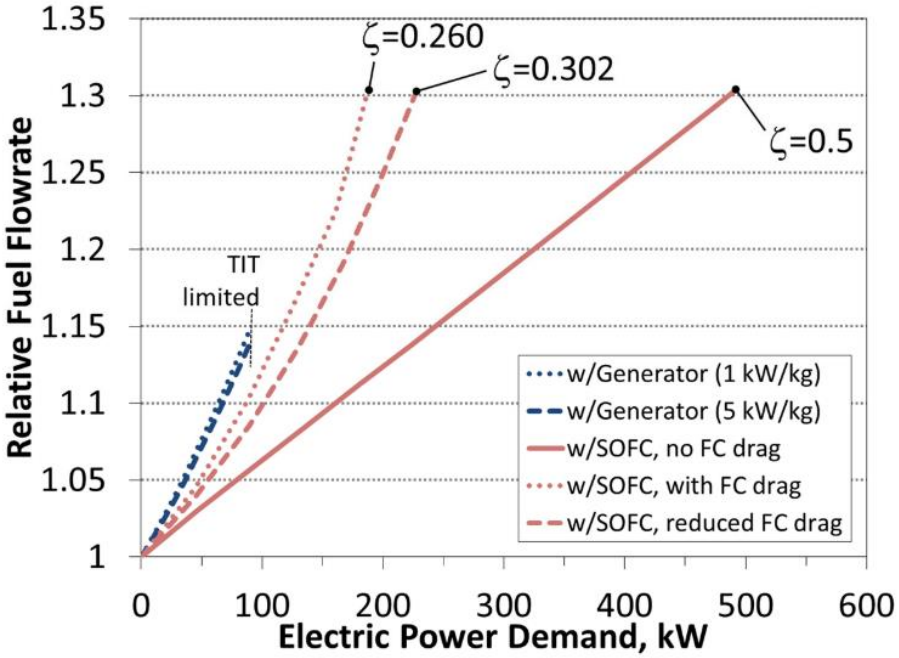

Figure 39: Comparison of relative fuel flow rate in BPR=5, OPR=24 GT-SOFC with and without external drag penalty, HALE UAV, level cruise at 16.8km, M=0.5, reproduced from Figure 95 of [1]

Additionally, the length growth case begins at the same power level as the 1-stack radial growth case, but incurs higher profile drag penalties in order to accommodate the turn-back into the combustor. Put another way, by allowing the fuel cell to turn back at all, the radius of the length-growth case needs to have a larger

diameter, and so incur more profile drag losses for the same power level. This initial disadvantage fades as the length of the fuel cell is increased.

However, the ability of the GT-SOFC to reach higher electric power fractions than the mechanical generator is consistent, with the mechanical generator ultimately limited in electric power fraction by the TIT limit, restricting how much energy can be added to the GT core flow. Both options increase the TIT; for the GT-SOFC, additional propulsive power needs to be extracted from the shaft to compensate for additional mass and profile drag, with the length growth case increasing in profile drag more slowly. Figure 40 shows the contributions to total drag from induced (due to added SOFC weight in the vehicle drag polar) and profile drag on the nacelle. We can immediately note that the change in profile drag is (1) larger than the change in mass-related drag as the electric power fraction increases, and (2) substantially different between the length-growth and stack-addition configurations.

The length-growth configuration increases the profile drag by ~250 N in return for 200kW of additional electric power generation, while the radial-growth configuration increases profile drag by ~600N for the same electric power! In contrast, both growth configurations have nearly identical induced drag values, with a relatively small change of ~150 N of drag between 50kW and 250kW of electric power generation.

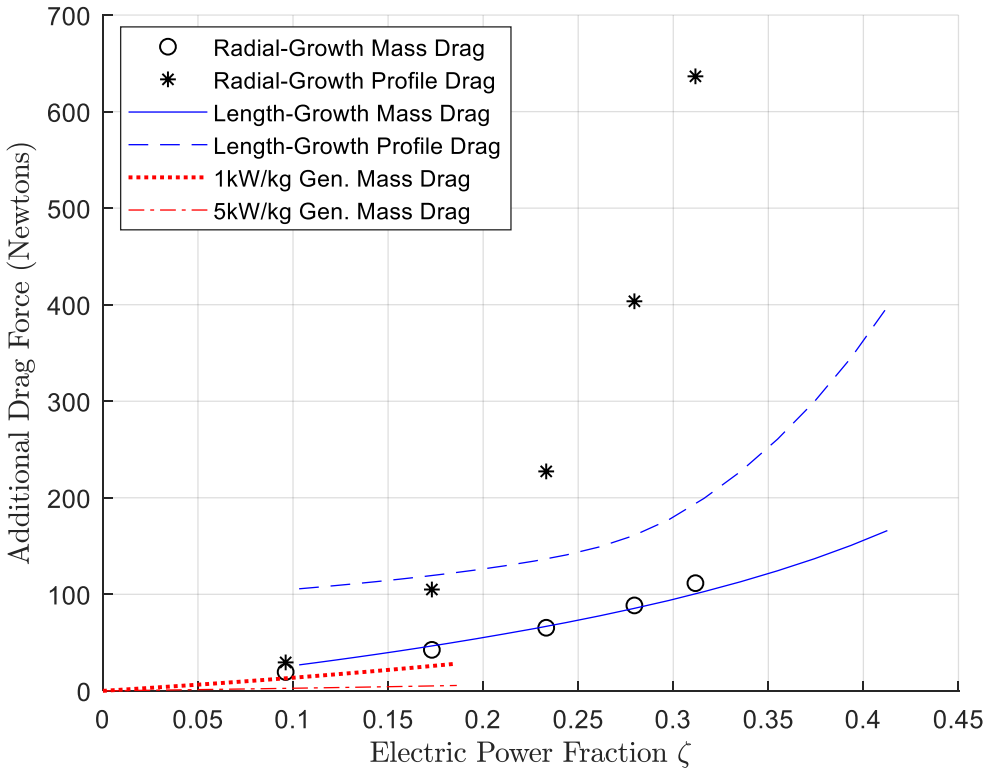

Figure 40: Contributions to total drag from Drag Polar (i.e. mass-varying) and nacelle profile drag from SOFC Assembly for configurations used in Sensitivity Analysis, all as functions of electric power fraction.

In all cases, the turbofan is required to increase the thrust output in order to accommodate increases in drag. Additional thrust requires additional energy to be added to the Brayton cycle, in turn driving up the necessary TIT in GT-SOFC configurations in order to maintain the same flight condition.

However, in these scenarios the temperature increase is less than when generating the same amount of electric power mechanically from the shaft. As such, the turbine inlet temperatures for the GT-SOFCs shown in Figure 41 rise more slowly (and the length growth case the slower of the two configurations) than for the mechanical generator but still rise, with similar trends in the relative fuel flow rates.

Ultimately, the GT-SOFC systems are restricted by the given spatial constraints rather than TIT.

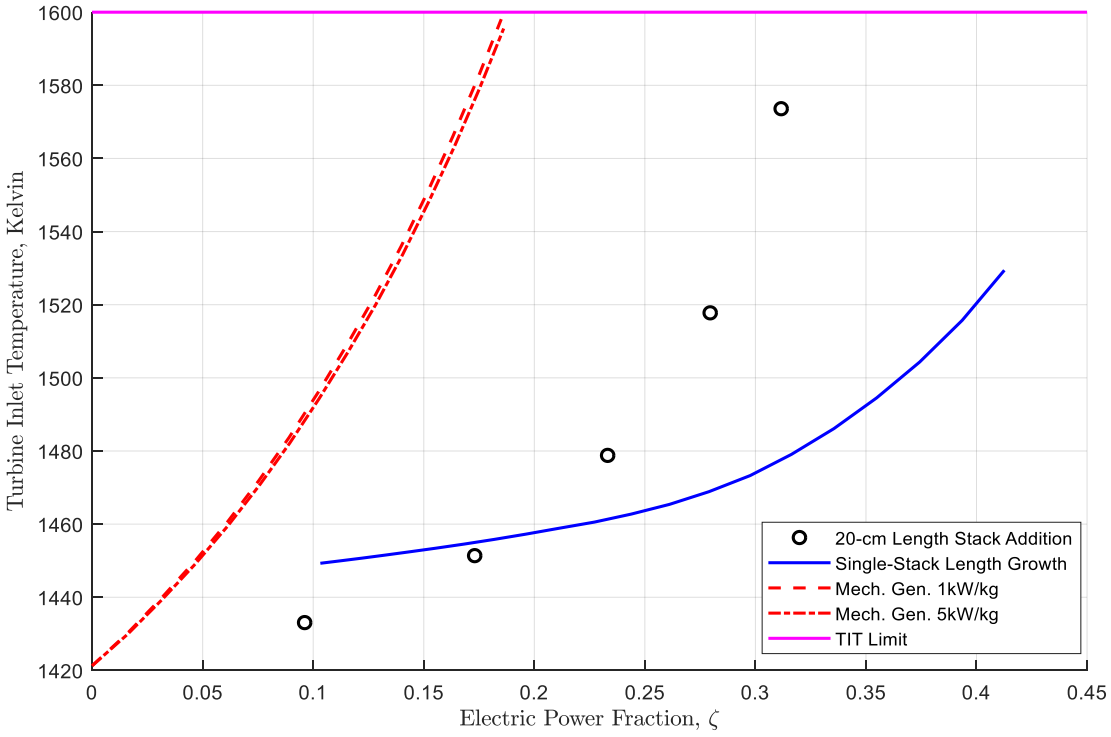

Figure 41: Turbine Inlet Temperature Variation with Electric Power Fraction for various electricity generation configurations on the HALE aircraft model

The increase in TIT implies an increase in throttle setting, with the aircraft here assumed during design (with no additional electricity generated) to be operating at 60% throttle in cruise. Consequently, an advantage that GT-SOFCs provide is a greater margin to increase engine throttle than when using mechanical generators for a given production of electric power.

The overall implication is that efficient aerodynamics for an integrated GT-SOFC are important for minimizing fuel expenses. Based on the evidence shown here, the aerodynamics are a more important consideration than the additional mass

of the SOFC. Put another way, the power density can be more important than the specific power if the assembly extends into the airflow.

9.7 Model Uncertainty

For any complicated nonlinear model such as the NPSS modeling performed here, there is a concern that uncertainties in the input parameters could lead to uncertainties in the conclusions that the model provides—in this case, that the uncertainty in fuel flow rate may encompass any variations we observe. This is checked by multiplying each sensitivity coefficient by the expected uncertainty in its associated parameter and summing the results in a root-sum-square (RSS) manner to get an overall uncertainty in fuel flow rate, as shown in Equation (27). Here, $u_{\dot{m}_{f,RSS}}$ is the expected (RSS) uncertainty in fuel flow rate, u_{y_i} is the uncertainty of any particular input parameter y_i, s_i is the sensitivity of the system to that input parameter, and N is the number of parameters considered. Waters and Cadou.[17] performed a similar analysis but for a smaller set of parameters.

$$u_{\dot{m}_{f,RSS}} = \sqrt{\sum_{i=1}^{i=N} \left(u_{y_i} s_i\right)^2} \tag{27}$$

In order to determine the set of sensitivity values s_i, a sensitivity analysis is performed for each of the converged states for the NPSS GT-SOFC model design conditions shown in Figure 37. To determine a sensitivity coefficient for each

variable in a design condition, the electrical power generated is added to the list of dependent variables so that the GT-SOFC "performance" of flight condition and electrical power output can be maintained while our variable of interest is changed. In order to maintain equal numbers of dependents and independents, the variable N_{rep} is added to the set of independents for the solver, allowing the size of the fuel cell stacks used to vary slightly to accommodate fractional changes in the variables of interest by providing slightly more or less reacting surface area in the SOFC. A finite difference method is used to estimate $\partial \dot{m}_f / \partial y_i$ is generated by slightly increasing or decreasing the value of the property y_i and re-calculating $\dot{m}_f$. The amount of increase/decrease is ~5% and is chosen as needed in order to cause changes in excess of the solver tolerances. The value of y_i is re-set and the solver is then run again to check convergence back to the original conditions. Equation (28) gives the formula for the sensitivity of $\dot{m}_f$ to the ith parameter.

$$s_i = \left(\dot{m}_{f,i} - \dot{m}_{f,0}\right)/\Delta y_i \tag{28}$$

Figure 42 shows the sensitivity of $\dot{m}_f$ to various parameters in the HALE aircraft operating at 55kft and M=0.5 for the three different designs illustrated in Figure 37.

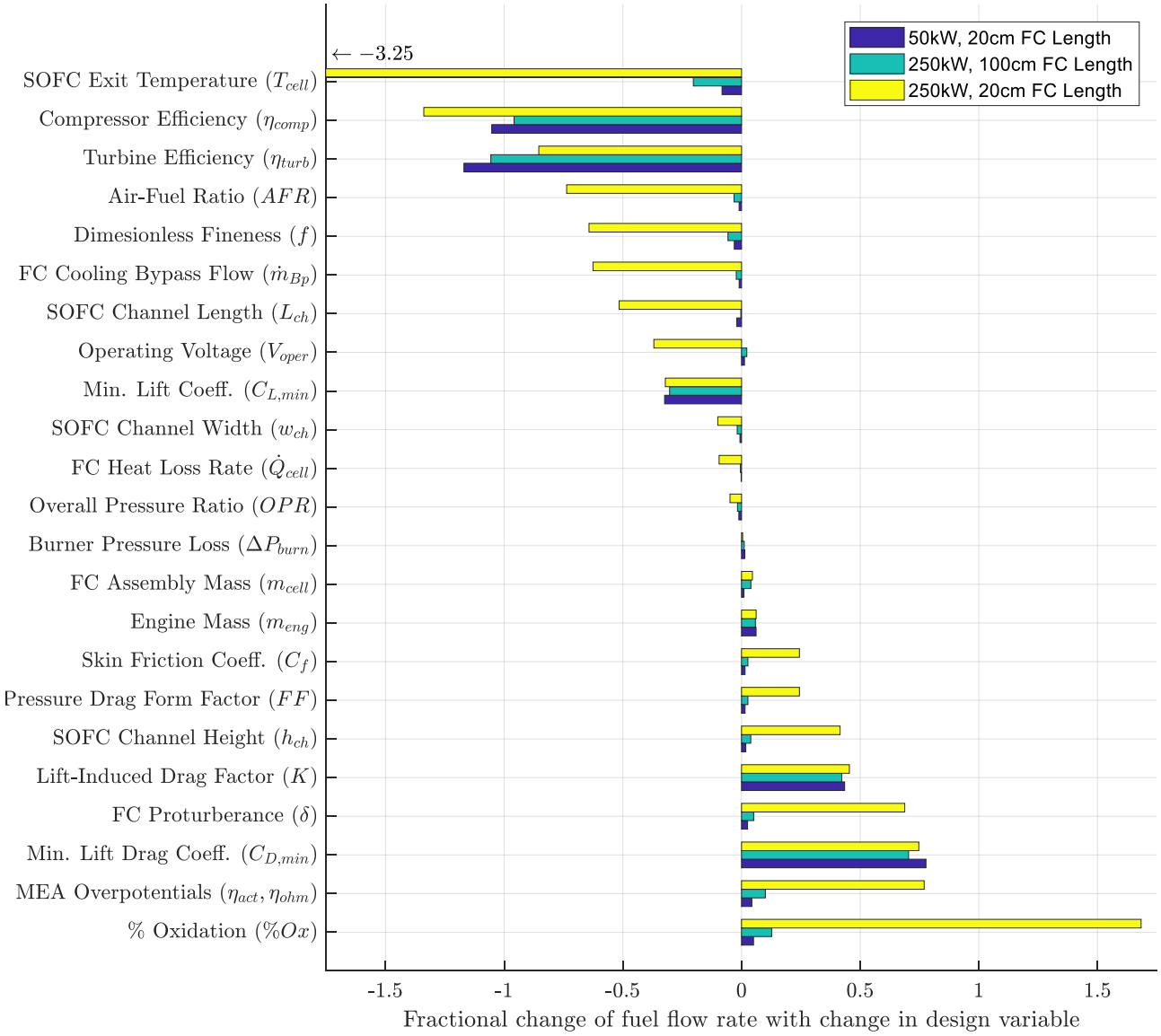

Figure 42: Sensitivity Analysis for High BPR Turbofan in HALE UAV conditions (BPR=5, OPR=24, 0.6V, 75% Oxidation @ 55kft M=0.5) at various electric power levels

This is a greatly improved and expanded version of prior analyses by Waters and Cadou [1, p. 159], [17] in which errors are corrected, more design variables are considered (especially those associated with profile drag) and different fuel cell

configurations are considered. In particular, the determination of turbomachinery efficiency (η_{turb}, η_{comp}) sensitivity has been corrected, and sensitivities to an additional drag polar variable ($C_{L,min}$) and fuel cell profile drag variables (C_f, f, FF, δ) have been included. Different power levels are also considered to illustrate the importance of making comparisons at different electric power fractions. The higher operating voltage of 0.7V with 90% conversion of fuel described in previous work has been omitted as any performance improvement is generally lower than the case given here. This is borne out by the lower sensitivity to operating voltage compared to the degree of oxidation which indicates an increasing fuel flow rate as higher conversions are targeted.

The most striking conclusion from the updated sensitivity analysis is that the flow-occluding configuration (adding stacks radially to add electric power rather than lengthening the existing fuel cells) yields order-of-magnitude greater sensitivities for values related to the fuel cell subsystem than either the lower power level or length-growth configuration at the same higher power level, with the most extreme sensitivity being to the SOFC exit temperature: Every 1% increase of fuel cell operating temperature reduces the relative fuel flow rate by over 3%!

As further evidence, all SOFC-related variables indicate reductions in the fuel flow rate by reducing the mass and especially profile drag of the system. For example, an increase in SOFC operating temperature increases the power density of the SOFC, allowing for a smaller fuel cell (in this case one with a lower N_{rep}) to provide the same target power level.

Finally, the sensitivity to variables unrelated to the SOFC assembly are only somewhat altered between all three cases tested, despite the difference in electric power generation and relative fuel flow rates observed. For all tested variables, a brief narrative explanation the system's sensitivity to each variable is provided in Table 5.

Table 5: Explanations of Fuel Flow Rate Sensitivity to System Parameters

	SYSTEM PARAMETER	EXPLANATION OF SYSTEM SENSITIVITY
AIRCRAFT PARAMETERS	Lift-Induced Drag Factor ($\boldsymbol{K}$)	Increasing induced drag increases the required thrust and thus fuel flow rate
	Min.-Lift Coefficient ($\boldsymbol{C_{L,min}}$)	Increasing the minimum lift coefficient increases aerodynamic efficiency thereby reducing overall fuel flow rate
	Min.-Lift Drag Coeff. ($\boldsymbol{C_{D,min}}$)	Increasing drag decreases aerodynamic efficiency thereby increasing fuel flow rate
GAS TURBINE PARAMETERS	Burner Pressure Loss ($\boldsymbol{\Delta P_{burn}}$)	Pressure losses reduce gas turbine efficiency increasing fuel flow rate for given thrust level
	Compressor Efficiency ($\boldsymbol{\eta_{comp}}$)	Increasing compressor efficiency reduces required fuel flow for given thrust level
	Engine Mass ($\boldsymbol{m_{eng}}$)	A heavier engine means more induced drag and increased fuel consumption.
	Gas Turbine OPR	Increasing overall pressure ratio increases kinetic rates in the FC decreasing system size, mass, drag, and thus fuel flow rate.
	Turbine Efficiency ($\boldsymbol{\eta_{turb}}$)	Increasing turbine efficiency reduces required fuel flow for the same performance
FUEL CELL PARAMETERS	Assembly Mass ($\boldsymbol{m_{cell}}$)	A heavier fuel cell assembly means more drag and increased fuel consumption
	Channel Height ($\boldsymbol{h_{ch}}$)	Increasing channel height increases FC protuberance without improving active surface area leading to more drag and increased fuel consumption.
	Channel Length ($\boldsymbol{L_{ch}}$)	Drag penalties from additional system mass dominate at lower power, with proportionally increasing benefits from additional active surface area with increasing electrical power fraction.
	Channel Width ($\boldsymbol{w_{ch}}$)	Increasing channel FC width increases active surface area of FC and decreases the necessary FC size leading to reduced drag and fuel consumption
	Cooling Bypass Flow ($\boldsymbol{\dot{m}_{BP}}$)	Increasing bypass flow rate (for a certain designed flow velocity in the bypass duct) allows further cooling of the FC, but also increases the duct area and thus drag
	Exit Temperature ($\boldsymbol{T_{cell}}$)	Increasing SOFC Exit Temperature increases FC kinetic rates reducing the necessary size of the FC and thus the drag and the fuel flow rate
	Fuel Oxidation (%$\boldsymbol{Ox}$)	Increasing % fuel oxidation reduces flow through the FC or increases the size of the FC. The former increases fuel consumption by reducing the overall efficiency of the system. The latter increases fuel consumption by increasing system weight and thus drag.
	Global AFR	Increasing the global air fuel ratio (in this model by increasing air flow into the SOFC assembly) effectively increases the bypass airflow improving cooling but also increasing drag via increased mass and internal aerodynamic drag.
	GT-SOFC Fineness ($\boldsymbol{f}$)	Increasing fineness (increasing length vs. cross-sectional area) reduces drag and thus fuel flow rate
	Heat Loss ($\boldsymbol{\dot{Q}_{cell}}$)	Minimal influence with magnitude approaching solver tolerances. Likely a tradeoff between additional mass and efficiency reduction through heat loss
	MEA Overpotentials ($\boldsymbol{\eta_{act}, \eta_{ohm}}$)	Increasing the internal fuel cell voltage losses lowers efficiency and increases fuel consumption
	Operating Voltage ($\boldsymbol{V_{oper}}$)	There is an optimum value determined by the V-I curve for the particular operating condition
	Pressure Drag Form Factor ($\boldsymbol{FF}$)	Increasing pressure drag increases fuel flow rate
	Protuberance into Fan Flow ($\boldsymbol{\delta}$)	Increasing protuberance increases drag and thus fuel flow rate
	Skin Friction Coefficient ($\boldsymbol{C_f}$)	Increasing skin friction increases drag and thus fuel flow rate

Recall that the sensitivity analysis is primarily intended to determine the expected uncertainty in our model's findings due to uncertainty of inputs—in particular the uncertainty of their effect on the relative fuel flow rate. Recall from Equation (27) that the second required piece of information is the uncertainty of each input value u_{y_i}. The uncertainty values are given to be a blanket 5% unless otherwise stated, with special attention paid to establishing more informed uncertainty values for high-sensitivity parameters. In particular, the following assumptions are made:

- Fitting parameter uncertainties in the drag polar are assumed to use rounded significant figures, such that their uncertainties are determined by the percentage equivalent of $\pm$ five-tenths the place of their last significant digit. For example, the minimum lift coefficient of the HALE aircraft is interpreted to be 0.3 ± 0.05, or $\pm 17\%$.
- The accuracy of the turbomachinery efficiencies is assumed to be within 0.1% as specified in the E3 program performance maps [89] applied to this model.
- All other variables receive a blanket assumption of accurate knowledge to within 5% of the real value, or knowledge to one part in twenty of the remaining variables, many of which are measurements of distance that are likely to be at least this accurate.

Based on these assumptions, the RSS uncertainty is found to be $\pm 5.5\%$ for the 50kW "base" case, $\pm 5.3\%$ for the length-growth 250kW case, and $\pm 21.0\%$ for the radial-growth 250kW case, with a visual representation given in Figure 43.

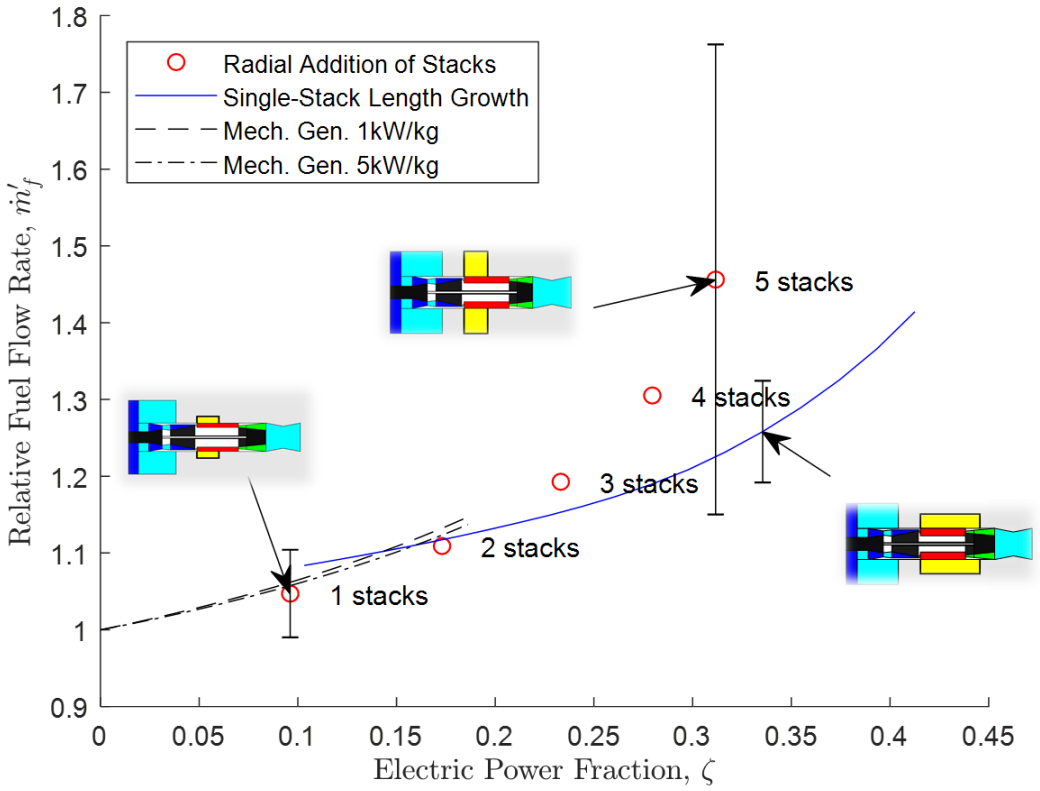

Figure 43: Uncertainty analyses included in relationship between relative fuel flow rate and electric power fraction for different GT-SOFC and mechanical generator configurations

On first inspection this is discouraging since the base case uncertainty fully encompasses the mechanical generator estimations, and a similarly large error bar is present for the length-growth case. The width-growth case expected uncertainty stretches between relative fuel flow rates of 1.1-1.8, encompassing the length-growth case entirely. However, the greatest contributing factors to uncertainty are the fitting parameter uncertainties associated with the drag polar. This emphasizes the importance of the airframe over modifications to the propulsion system, but the airframe is independent of the system under investigation.

If we redo the uncertainty analysis neglecting the drag polar parameters, we instead yield $\pm 0.7\%$ for the 50kW "base" case, $\pm 1.5\%$ for the length-growth 250kW case, and $\pm 20.3\%$ for the radial-growth 250kW case, represented visually in Figure 44.

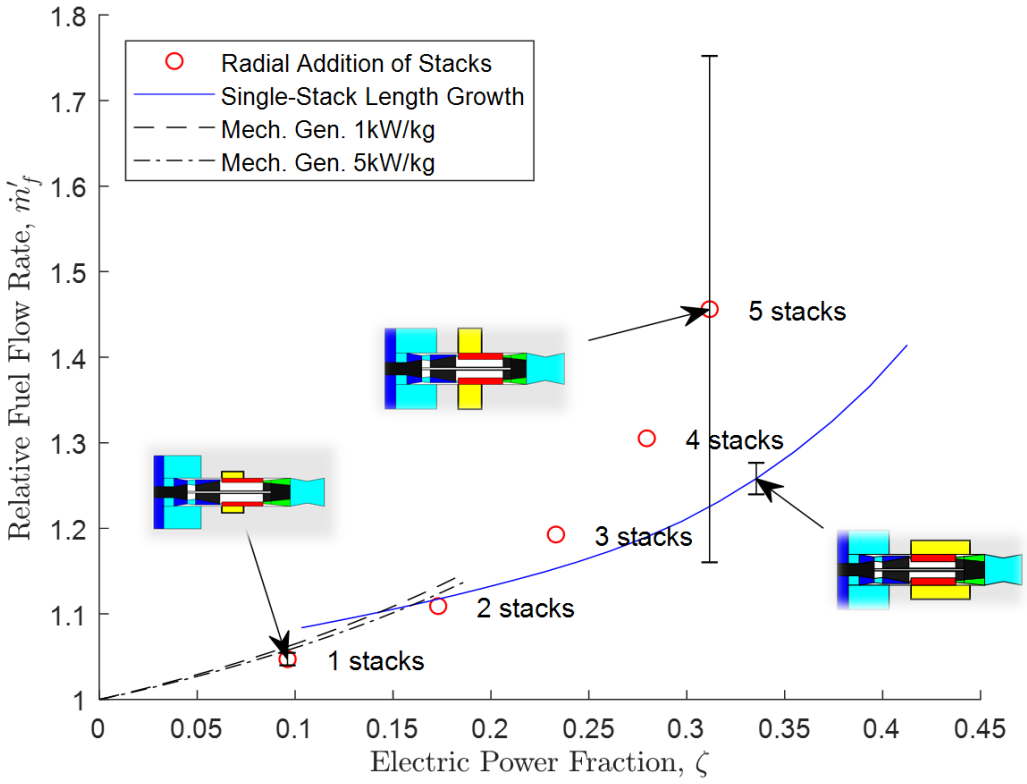

Figure 44: Uncertainty analyses (excluding drag polar parameters) included in relationship between relative fuel flow rate and electric power fraction for different GT-SOFC and mechanical generator configurations

Under this analysis including only the GT-SOFC parameters, the two more "reasonable" base and length-growth scenarios exhibit reasonable uncertainty from which we may reasonably draw conclusions. The radial-growth case however retains a large uncertainty, which is unsurprising given the high sensitivity values the case

had for many fuel-cell parameters. The conclusion is that this questionably physical case likely stretches the pylon drag model beyond its region of usability.

In closing, it has been shown here that profile drag may constitute a substantial barrier to minimizing the relative fuel flow rate for GT-SOFC systems, usually well in excess of mass-induced drag penalties. Additionally, we may conclude that while a GT-SOFC has an increasing improvement versus a mechanical generator at higher electric power fractions, the most significant advantage is in generating greater amounts of electrical power before encountering the turbine inlet temperature limit.

10 APU Model

10.1 Approach

The Ultra/AMI D300 (Figure 45) is a propane-fueled, SOFC-based APU that produces 300W (32V, 9.5A). It is similar to the current D300 and was marketed to the US military primarily for the purpose of recharging batteries in the field quietly.[63], [90]

Figure 45: Two Ultra/AMI D300 APUs with standard propane tank supply

The APU features a set of 56 tubular, propane-fueled SOFCs each with an integrated CPOx fuel reformer that converts the propane fuel to syngas (predominantly H_2 and CO) for use by the fuel cell. The tubular cells are bundled together in a cylindrical array with a CPOx reformer making up roughly the front third on the upstream side of each tube followed by SOFC in the remaining two-thirds. Immediately downstream of the SOFC array is a combustor that burns the remaining fuel and oxidizer to maintain

system temperature. The integrated CPOx/SOFC element is shown in Figure 46. Its compact, self-contained nature makes it very well suited for integrating with a small gas turbine: It has a single air inlet, a single exhaust outlet, built-in instrumentation that measures air and fuel flow rates as well as temperatures and currents in all of the FC elements, and its own control system. The initial plan is to retain the control system and continue to operate on propane. Subsequent efforts would replace the control system and switch the fuel to Jet-A.

While the APU is designed to operate at approximately 1 atm of pressure, the manufacturer has indicated that it is possible to operate it at higher pressures - albeit at higher risks of leaking and overheating. The manufacturer has also indicated that the reformer would likely work with Jet-A for some unknown period.

Note from Figure 46 that the main power generation components only occupy the bottom half of the APU. The rest of the space is taken up by fuel filtering, battery, power electronics, and blowers. This illustrates the significant effect that balance-of-plant components have on the mass and volume of fuel cell systems. Note also the similar size of the APU compared to the small gas turbine whose power output is well in excess of 10 kW, constituting greater than an order of magnitude greater power density over the APU. This demonstrates the power density advantage of engine-based energy conversion systems over unhybridized fuel-cell-based energy conversion systems.

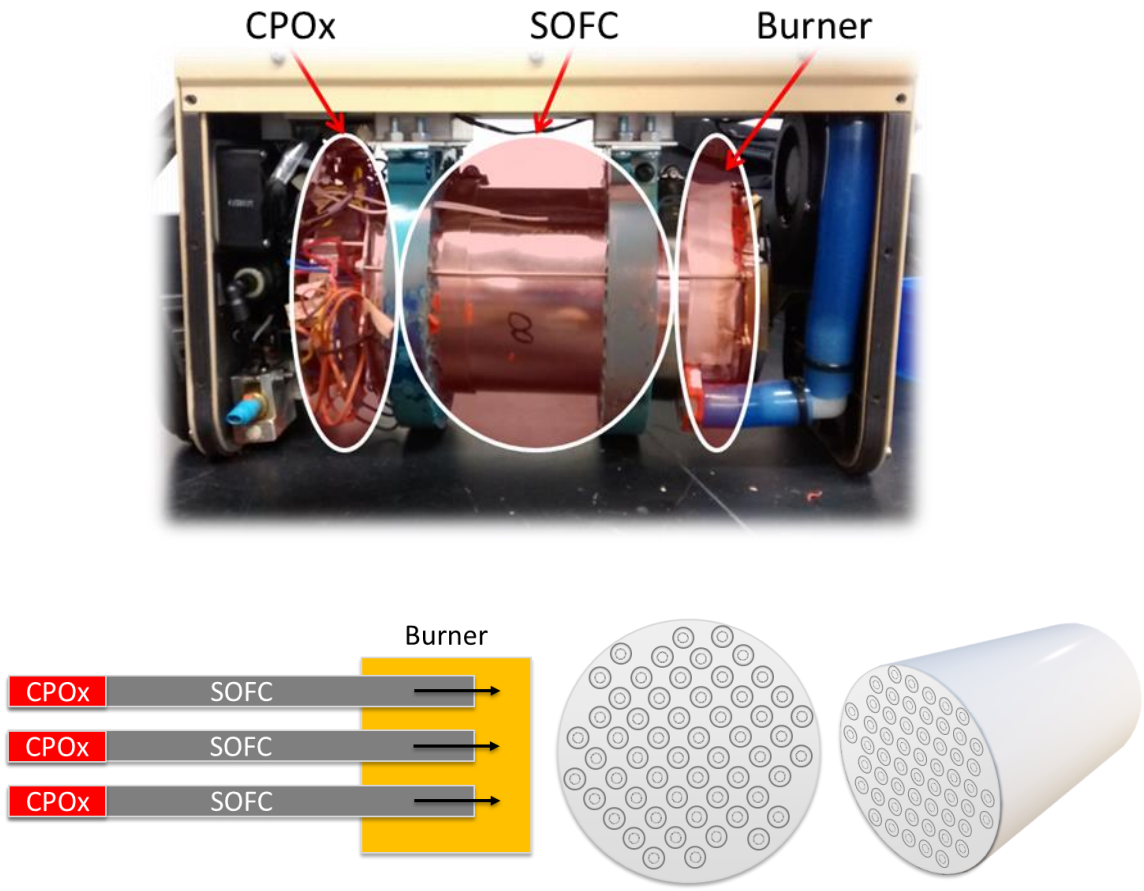

Figure 46: APU hardware identification in photograph (top) and rough layout diagram (bottom)

Unfortunately, no model nor any precise internal schematic are available for the performance of the integrated CPOx/SOFC. Therefore, the rest of this chapter is devoted to measuring the APU's operating voltage and current over a wide variety of operating conditions in order to develop a model of its performance. This task was made somewhat easier by the fact that the APU is equipped with an ASCII data port (RS-232) that enables one to interrogate all internal sensors. The main challenges were learning how to extract data from the RS-232 port and the extremely long

equilibration time of the system which eventually required the development of methods for inferring steady-state performance from non-steady-state measurements.

What follows are the results of a non-destructive characterization of the system. From here onward, I will refer to ‘measurements’, ‘data points’, ‘operating conditions’, ‘runs’ and ‘experiments’. ‘Measurements’ will refer to raw data output from the device while ‘data points’ refers to the processed results of those measurements to generate a single value for a given operating condition. An ‘operating condition’ is a set state of operation for the system for which we are trying to generate a data point. A ‘run’ refers to a physical instance of data collection using the standard operating procedure discussed later in this chapter, while an ‘experiment’ is the collection process for a single data point.

10.2 Instrumentation and Data Acquisition

Conveniently, the APU is instrumented with a variety of temperature, flow rate, and other status sensors placed at a variety of locations within the housing to inform the control system of the APU status. Less conveniently, almost all of these sensors are inaccessible for calibration, knowledge of precise location, and replacement without disassembling the device. Furthermore, this makes connecting additional external instrumentation difficult and calibration nearly impossible without substantial risk of damaging the system.

All sensor outputs can be polled in near real time (approximately 1.5 Hz) through the ASCII data port. A challenge was that the port did not follow a known standard to interact with data acquisition software like LabView out of the box. As a result, a customized set of data acquisition and processing scripts needed to be created. One run (November 10, 2017) has data collected only by written observations due to the failure of the data acquisition system. Further processing is then readily carried out in MATLAB, the results of which will be discussed later.

10.3 Experimental Setup and Procedure

A schematic illustration of the overall experimental setup is presented in Figure 47 and a photograph of the system is presented in Figure 48. The system consists of several components including:

- BB-2590 Battery (incl. charger, neither pictured)
- Propane filter (for sulfur removal)
- Propane fuel tank (mercaptan-free to minimize use of the sulfur filter)
- Propane gas regulator (~30 psi max output all that is initially required)
- Raspberry Pi B (with keyboard/mouse/monitor/power-supply)
- RS-232-to-USB converter (not pictured)
- RS-232-to-coaxial converter (not pictured)
- Power Resistor Bank (Resistive load)
- Associated gas tubing and fittings

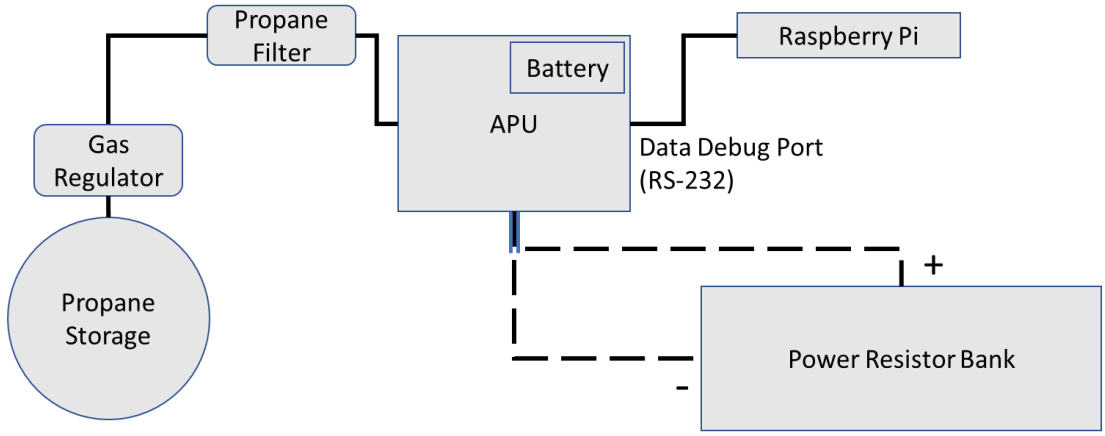

Figure 47: SOFC APU experimental setup component diagram

Figure 48: Image of SOFC APU experimental setup

The power resistor bank is comprised of several arrays of power resistors with each array capable of rejecting at least 400W total output power (well above the APU rating of 300W). The arrays are stepped in total resistance such that following a quasi-binary progression provides resistance increments of approximately 8 ohms by design in the range of 1.5-122 Ohms. The arrays are generally used in series with at

least one 1.5Ω 400W dissipation-rated power resistors connected at all times for safety. Clip leads connect the power output terminals inside the APU body to the load bank. The negative lead is connected to a safety switch that is turned off before changing the load state. Cooling is provided by a room fan that blows air along the length of the power resistor bank, starting near the negative lead. The resistive load applied to the APU is changed by connecting and disconnecting different sets of power resistors at clip connections shown in Figure 49. Each set of power resistors is rated to handle 400W of dissipation in series, though in nearly all scenarios this is a substantial safety margin since the APU is rated to 300W maximum output, and the internal power conditioning causes it to function as a constant-voltage source of 32.6V that limits the power dissipation to $P = V^2/R$, or $P = 1063/R$. If the given 300W output is to be followed, the lower boundary for the resistance value is approximately 4Ω, while any higher resistance value will be dissipating less power. While the stack voltage may exceed the output voltage at low current values, in the case of a short the stack supply voltage would drop precipitously, again lowering the effective power output. Practically, individual resistors within the sets may be placed in series or parallel (e.g. two 2Ω resistors in parallel yielding a single ohm) to achieve greater resolution of resistance when their individual power dissipation ratings will not be exceeded in the overall circuit. The varied load allows us to access a range of operating points along the stack potential curve, albeit generating a nonlinear range of power. This can be seen in Table 6 which is a partial (of a total of 64 design states) state table assuming that the APU output remains constant at 32.6V (std. deviation ≈

0.5V). Observations indicate that this is mostly the case. A constant-current load bank is being developed to replace the current power resistor bank and allow more consistent loads to be applied to the APU and future GT-SOFC demonstrator.

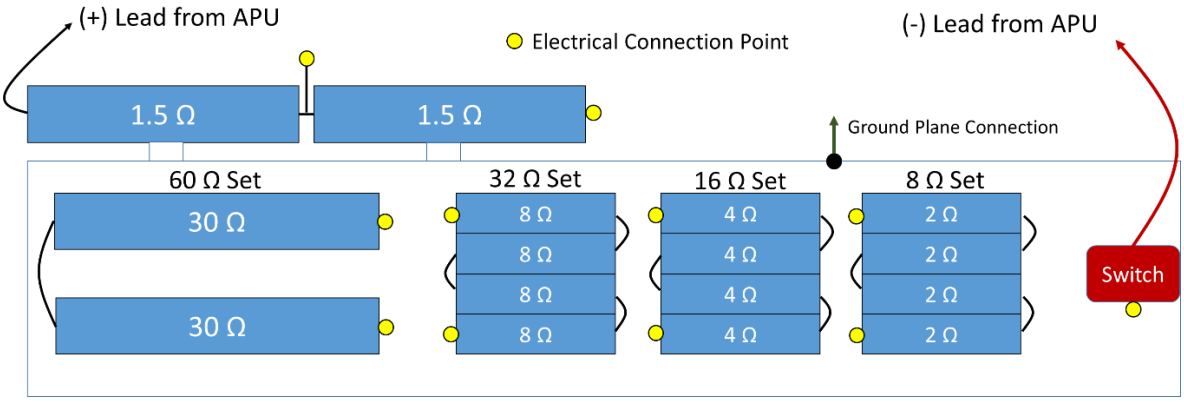

Figure 49: Diagram of Power Resistor Bank

Table 6: Partial State Table for Power Resistor Bank

60 Ω set	32 Ω set	16 Ω Set	8 Ω set	Secondary 1.5 Ω	Total Resistance (Ω)	Power Dissipation (W)
			X		9.5	112
		X			17.5	60.7
		X	X		25.5	41.7
	X				33.5	31.7

The complete Standard Operating Procedure (SOP) for measuring APU V-I curves is provided in Appendix 13.3. An abbreviated version is reported here. An experiment begins by turning the APU on. This connects the APU's control system to an onboard battery that powers the system as it brings the SOFC stack to the target

operating temperature of 790 C. Once this temperature is reached, the control system switches to electrical power generated by the SOFC and recharges the battery. Our experiments begin after the battery is recharged (approximately one hour) and the system has reached equilibrium. It takes an additional 20-30 for the system to equilibrate between operating conditions. When a set of experiments is complete, the system proceeds with an approximately 20 to 30 minute shutdown sequence where the fuel cell is allowed to cool slowly. This is likely to prevent system damage from mechanical stresses induced by coefficient of thermal expansion (CTE) mismatch to the tubular cell, as well as to the Nickel anode, which can degrade at high temperatures under oxygen or water to form NiO. The formation of bulk NiO places substantial mechanical stresses on the anode layer and can permanently damage the performance of the SOFC.[82], [91] Similarly to prevent unwanted oxidation of the anode, it has been suggested to operate the SOFC at cell voltages greater than 0.6V, which in this system indicates a stack voltage of 33.6V. This is all in addition to dangers of rapid or uneven thermal contraction. In some instances, the APU has suddenly lost power and turned off without this shutdown cycle. If this happens, it is important to rapidly restart the system and resume the controlled shutdown cycle in order to prevent damage. The system provides no notification of power failure; consequently, the power loss has not always been noted immediately and the system has been allowed to stand hot for at most the length of an experiment (~20-30 minutes). However, such instances are not correlated to the varying polarization curve provided by the APU shown in later sections.

The goal of the experiments is to measure the SOFC's polarization (V-I) curve by varying the electrical load on the system and measuring V and I. All results are for a single stack operating temperature (790C) because of the control system. Future experiments could investigate the effect of changing the target operating temperature (by bypassing the control system) and increasing the operating pressure (by feeding the stack compressed air).

10.4 Typical Data and Challenges

While it would be tedious to display all sensor outputs, several are of importance and will be illustrated as they appear in a test run with a single trial. Most important are the "stack" voltage and current values which measure the state of the fuel cell stack itself, rather than the operating output of the APU system, which includes substantial power conditioning and balance-of-plant losses that are distinct from the CPOx/SOFC.

Other important variables include the stack temperatures, and flow rates. The APU operates at local atmospheric pressure. Figure 50 below shows time histories of voltages, currents, power output, temperatures, and flow rates over the course of a single run from start to finish. This particular run included only one load point which was the recharging of the starter battery.

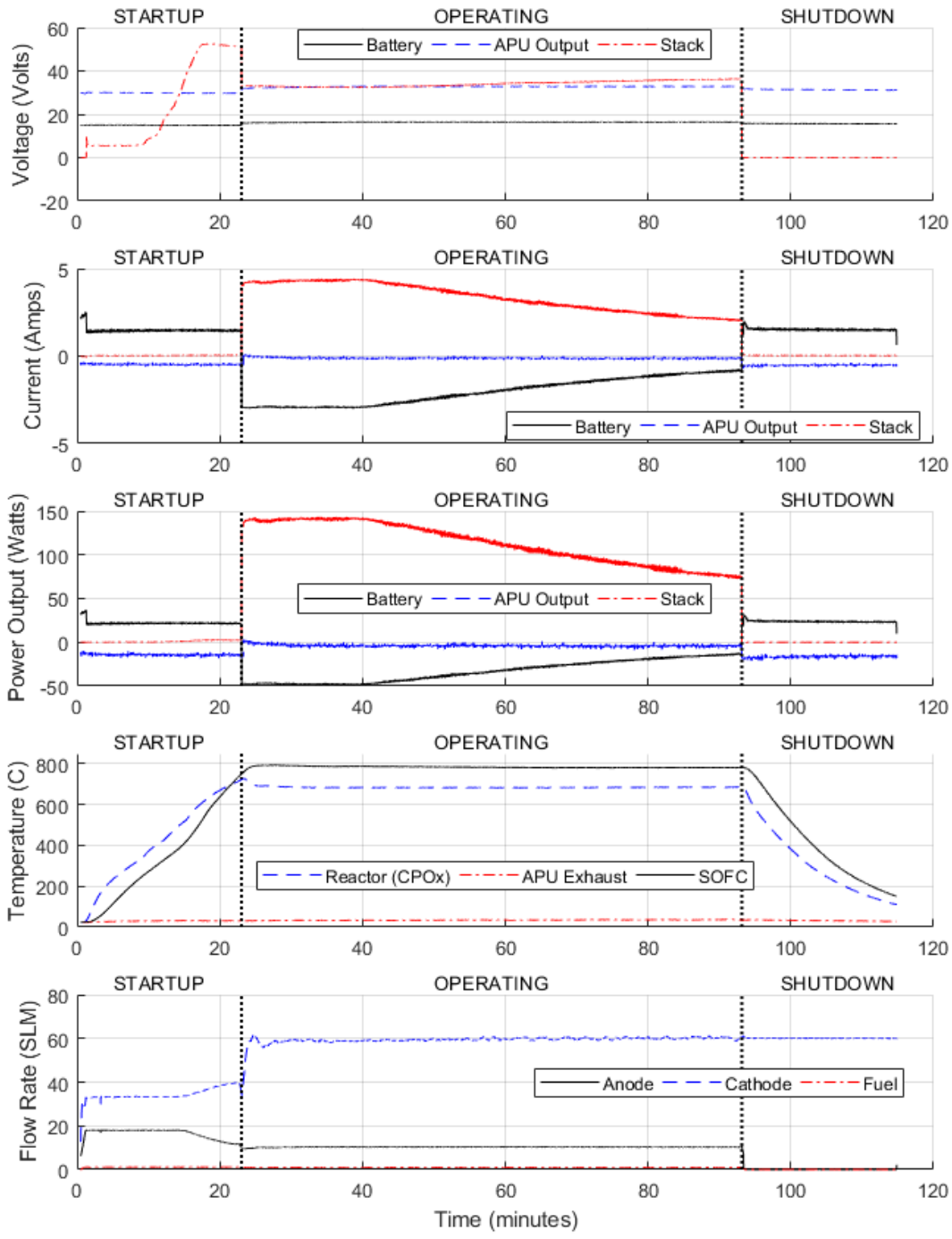

Figure 50: Example Voltage, Current, Temperature, and Flow Rate time histories for startup, operation (in this case only re-charging the battery) and shutdown.

Figure 50 also shows startup and shutdown conditions. During startup, the onboard battery is used to start the system balance of plant for approximately 25 minutes. During this period, the SOFC stack is not under load, and its voltage rises to nearly the open-circuit voltage (OCV) before the system switches from the battery to the SOFC stack to maintain balance of plant. The stack voltage just prior to the startup of each run lacks the balance-of-plant loads and has temperature conditions closest (within approximately 5K of the operating temperature) to those during operation. As such, it can be considered the OCV of the stack, usually observed to be around 0.9V. The current draw from the battery during startup is substantial: over an amp (at ~16.5V from two batteries). Fuel and air burned in the tail gas combustor heats cathode air raising the temperature of the SOFC

When the SOFC reaches its target temperature (790C), the system switches from battery power to SOFC power and recharges the battery. The charging current tapers off as the battery approaches capacity although charging will continue at trickle-charge levels. Temperatures, the APU output voltage, and fuel and air flow rates generally remain stable during operation although the actual demands on the SOFC will vary with load and charge condition of the battery.

During shutdown, fuel and anode flow (a partial oxidation of fuel and air) will cease while airflow through the cathode continues. The SOFC stack is disconnected from both internal and external loads while the recharged battery resumes powering the balance of plant. The CPOx/SOFC cool steadily during shutdown until a sufficiently low temperature (~150 C) is reached that the system can be shut down. In

most runs, the startup and shutdown cycles are only partially recorded, if at all. A table of all experiments performed is included in Appendix 13.4, along with graphical results for each run in the form of Figure 51.

Figure 51 is an example time history from a typical experimental run that illustrates some of the possible challenges (circled areas).

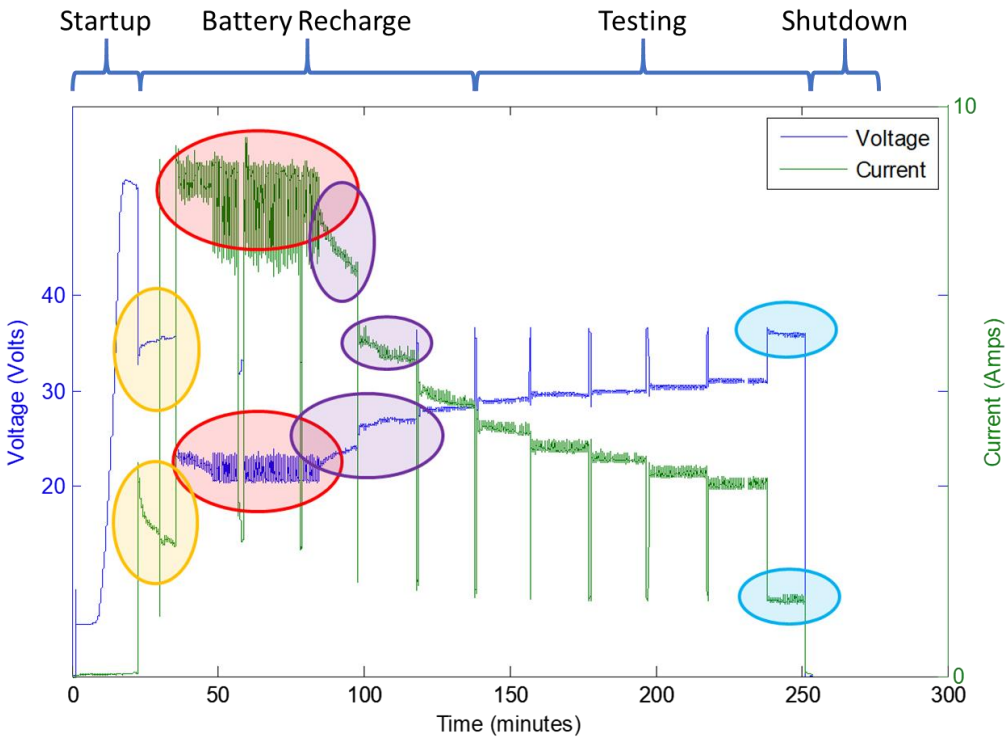

Figure 51: Typical experimental output for APU stack voltage and current, oval highlights added for in-text description

Voltage is plotted in blue and current is plotted in green. At the far left the voltage sits near a peak value of 51.3V, the OCV for this run. In the yellow circled areas, we see a sudden drop in voltage and increase in current followed by an exponential decay as the battery that starts the APU is automatically connected to the

system and subsequently recharged. The battery is allowed to fully charge before measurements are collected.

The red ovals above (second from left) show the response of the system to an overload condition when more current is demanded than is considered ‘safe’ by the control system. The protection mode causes ‘noisy’ data as the load is rapidly disconnected and reconnected by the control system. This protection mode prevents access to the full SOFC polarization curve by setting an upper limit on current and a corresponding lower limit on voltage.

The purple ovals show the temporal responses of voltage and current to the application of a fixed resistive load. Voltage and current oscillate, likely due to control system feedback, while the averages approach steady-state asymptotically. It can take 20-30 minutes or even longer (according to the manufacturer) to reach equilibrium. This is a significant problem because it makes experiments take a long time and makes it hard to know when the system has really reached equilibrium. Strategies for predicting voltage and current at equilibrium by fitting curves to time histories are addressed in a later section.

Finally, the rightmost set of blue ovals show voltage and current time histories associated with no external load connected. Current is not zero and voltage is not near the maximum observed (51.3V as the observed OCV) because of the balance of plant loads. This prevents us from measuring the low-current/ high-voltage portions of the polarization curve. While some insight might be gained from the response of the system under battery power as the fuel cell comes up to temperature during startup,

interpreting it is complicated by the fact that the cell is not at a constant temperature. Voltage and current jump to their no-external-load values between data points when one load is disconnected and replaced with another. This produces the 'spikes' seen between testing loads in Figure 51. Finally, note that the fuel cell responds almost instantaneously to changes in electrical load over the observable timescale of ~1 second. By comparison, the long (20-30 minute) equilibration process indicated by the manufacturer instead represents a relatively small change relative to the instantaneous response when presented a change in load.

10.5 Measurement Processing

The measurements collected from the APU debug port are often noisy, both with random noise and systematic distortion from a variety of causes. These can include (1) the random fluctuations in the electrical load placed on the stack, (2) variation in electrical load as the resistive load bank heats up (increasing the resistance), as well as (3) the equilibration of the SOFC stack itself to the change in load and heating conditions, which the manufacturer (corroborated as good-practice as well by Mastropasqua et. al.[92]) has suggested to take at least 20-30 minutes between data collection. Finally, (4) any hysteresis, degradation, or other variation in conditions during the test that alters the polarization curve without being sufficiently corrected by the equilibration process.

As such, the output requires additional processing in order to infer fundamental characteristics of the fuel cell. Regarding (1) the stochastic error takes place over an

approximately 1.5 Hz sampling rate (roughly 0.65 seconds per sample). Averaging across a given number of data points can smooth the data reasonably, as observed in Figure 52. By observation, one minute of observations (~90-100 points) yields a substantially smoothed trendline.

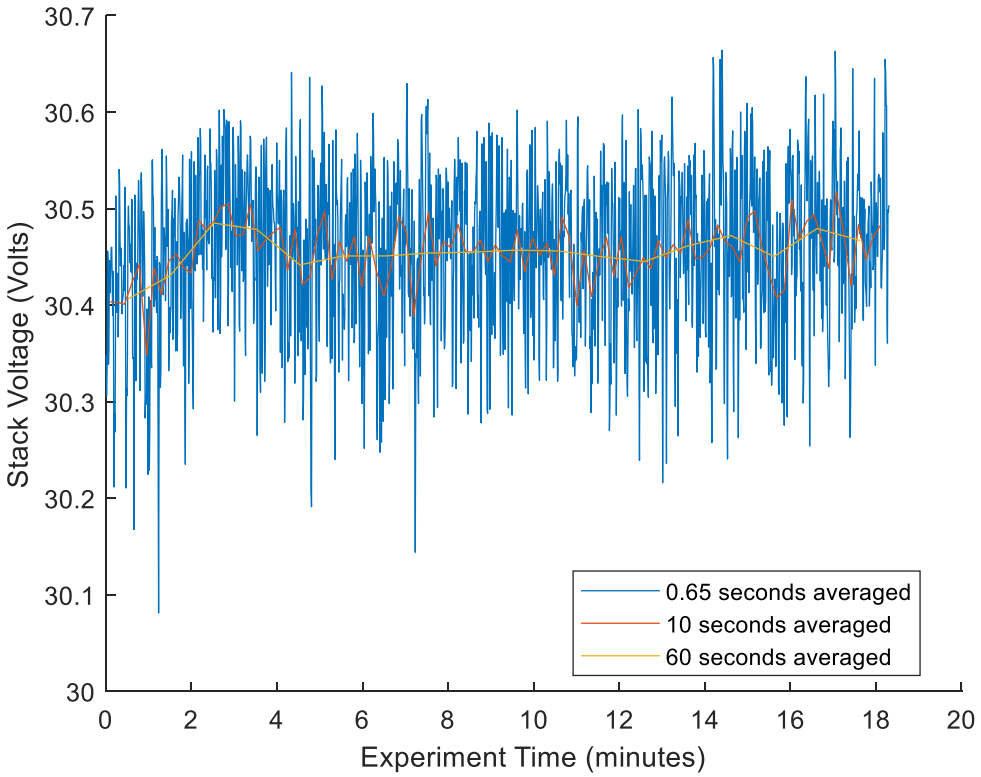

Figure 52: Stack voltage time histories: Raw measurements and averaged data over 10s and 60 s windows.

Issues (2) and (3) are addressed by allowing each experiment to run for an extended period, so that both the SOFC stack and the power resistor bank to equilibrate. Issue (4) is inferred by comparing data from many runs. For example, if consecutively acquired data points fall along a well-defined trendline, but repeating the experiment over different days yields different trend lines it suggests that the fuel

cell itself may be changing/degrading over time. Unfortunately, this appears to be occurring and the stochastic measurement variation and equilibration are relatively minor distortions compared to the variation between runs. Therefore, we will first address the apparent degradation between runs before addressing corrections for noise and system equilibration time.

Figure 53 shows APU stack voltage vs. current output for 6 different sets of experiments. Data collected by hand are included to show historical trends.

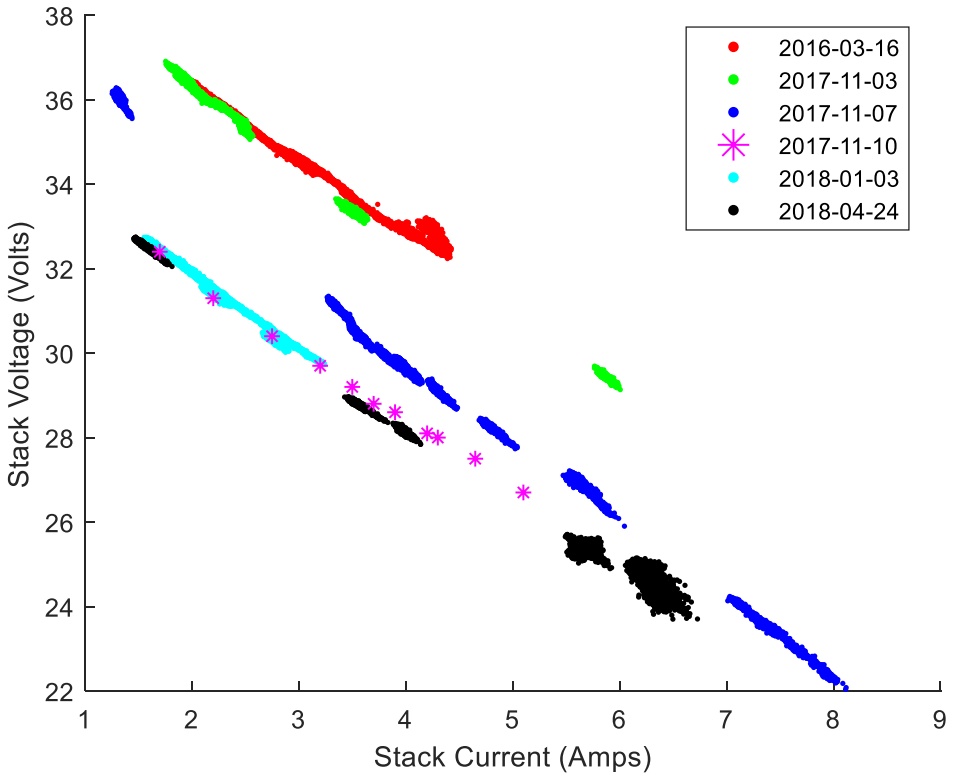

Figure 53: Polarization Plot of Raw Output from Different Experiment Runs. Starred data (Nov. 10, 2017) are hand-recorded from end of each experiment.

10.5.1 Fuel Cell Stack Performance Degradation

Figure 53 shows that the performance of the APU fuel cell stack tends to get worse over time and between runs, providing current at lower and lower voltages, indicating greater losses in the production of electricity. In particular, between November 3rd and November 10th, 2017 the stack performance degrades substantially. Figure 53 also illustrates qualitatively the relatively large degree of error represented by run variation versus noise or system equilibration. The explored "middle" portion of the polarization curve the data represent, wherein the current draw is substantial but not near the extreme of the fuel cell's capability, is expected to be largely linear as a result of ohmic losses in the fuel cell (see Figure 75 in section 13.2), and this is observed qualitatively for all data collected in a single run. Furthermore, the slope of a fitted line is mostly consistent between runs, such that the source of the variation in overpotential is expected to be related to changes in activation polarization, and degradation occurring between runs which suggests a thermal or redox cycling issue.[91]

Review of the notes taken during this period, as well as raw data output for all variables recorded by the APU, do not indicate a clear reason for the sudden degradation in this period, though a trend of a variation of about 10 Kelvin temperature decrease over time is observed for the fuel, exhaust, and control electronics operating temperatures, with higher performance associated with the higher operating temperatures—though temperatures within the stack itself are

consistent. Furthermore, sets of runs together before and after November 2017 appear to be internally consistent, i.e. the degradation occurred over a couple of runs, and has stabilized, which indicates that this may have been some kind of break-in process for the APU.

A possible explanation for the degradation include the formation of NiO from Ni in the anode during shutdown.[91] Fuel flow ceases during shutdown, so oxygen supplied from reacted water and carbon dioxide or air may leak into the anode chamber provide the oxidative environment. NiO formation places mechanical stress on the anode material and alters the nickel grain size, amount, and geometry, reducing the number of active sites in the anode. Alternatively, sulfur impurities could degrade performance—albeit in this case desulfurized propane (<1ppm) and a sulfur filter were employed to prevent this effect.

Finally, individual SOFC tubes may have failed (e.g. shorted out), as the system does not report on the status of each unit within the stack. In fact, the observed open circuit voltages are approximately 0.9V, which is lower than the 1.1V typically expected for SOFC systems.[82, p. 1213] This suggests that the overall stack voltage should be divided between fewer than the total 56 tubular SOFC units present in the APU, perhaps as many as 10 of the 56 if the typical open circuit voltage is achieved. However, the OCV value of the stack is largely consistent across all runs (0.91-0.89V), which is evidence that the observed ~10% degradation isn't due to additional SOFC units shorting out.

As it represents the current performance of the fuel cell, we can consider the observed polarization curve to be represented by the data collected on Nov. 10th, 2017 and onward. While other data collected can be used for testing different processing methods, they do not represent the current polarization curve of this APU unit.

10.5.2Last Minute Analysis

One strategy for addressing the equilibration problem is to simply wait a specified amount of time (the same for every new data point) and then average over the last minute to get a voltage and a current. Figure 54 shows the results of such an approach, including experiments that were only hand-recorded since they were taken at the end of each experiment as well.

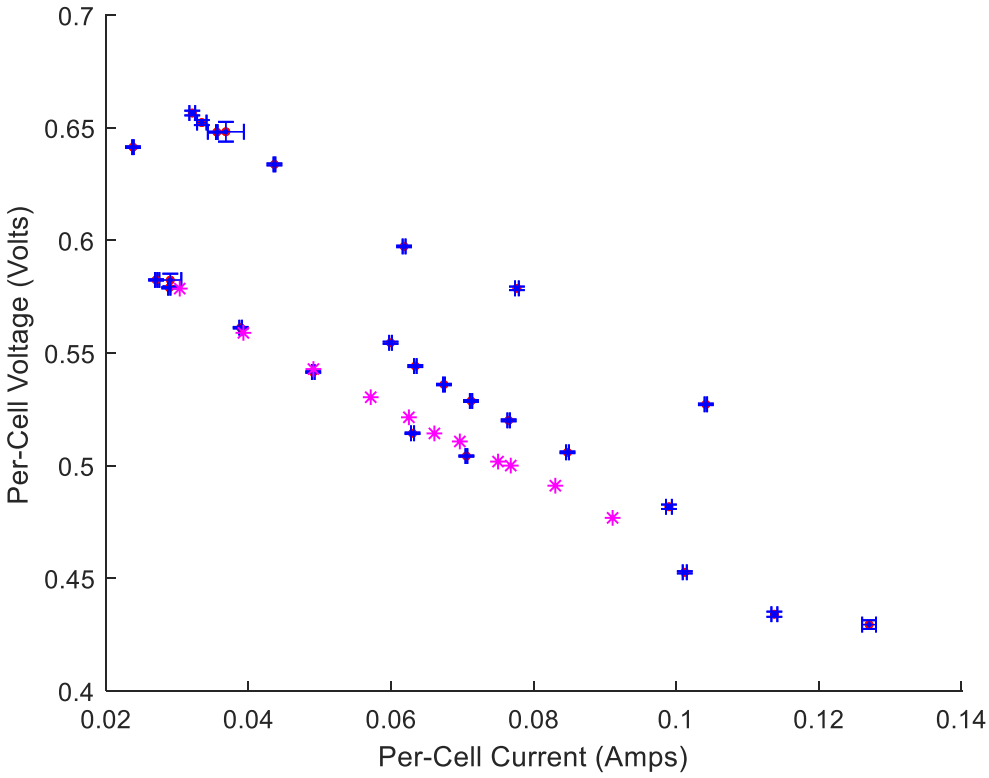

Figure 54: Polarization curve derived from average of last-minute data with one standard deviation error bars; starred data indicate hand-recorded experiments without error information

Although difficult to see, the data in Figure 54 also have error bars indicating one standard deviation in both cell voltage and cell current, which clearly show that the trend is much larger than the measurement uncertainty. When we limit our results to the more recent data points (i.e. from Nov.10th 2017 and onwards) and apply a linear fit, we generate Figure 55. Figure 55 also includes the observed OCV during later runs, although the intervening low-current region of the polarization curve is currently inaccessible while the stack is used to maintain the balance of plant in the APU.

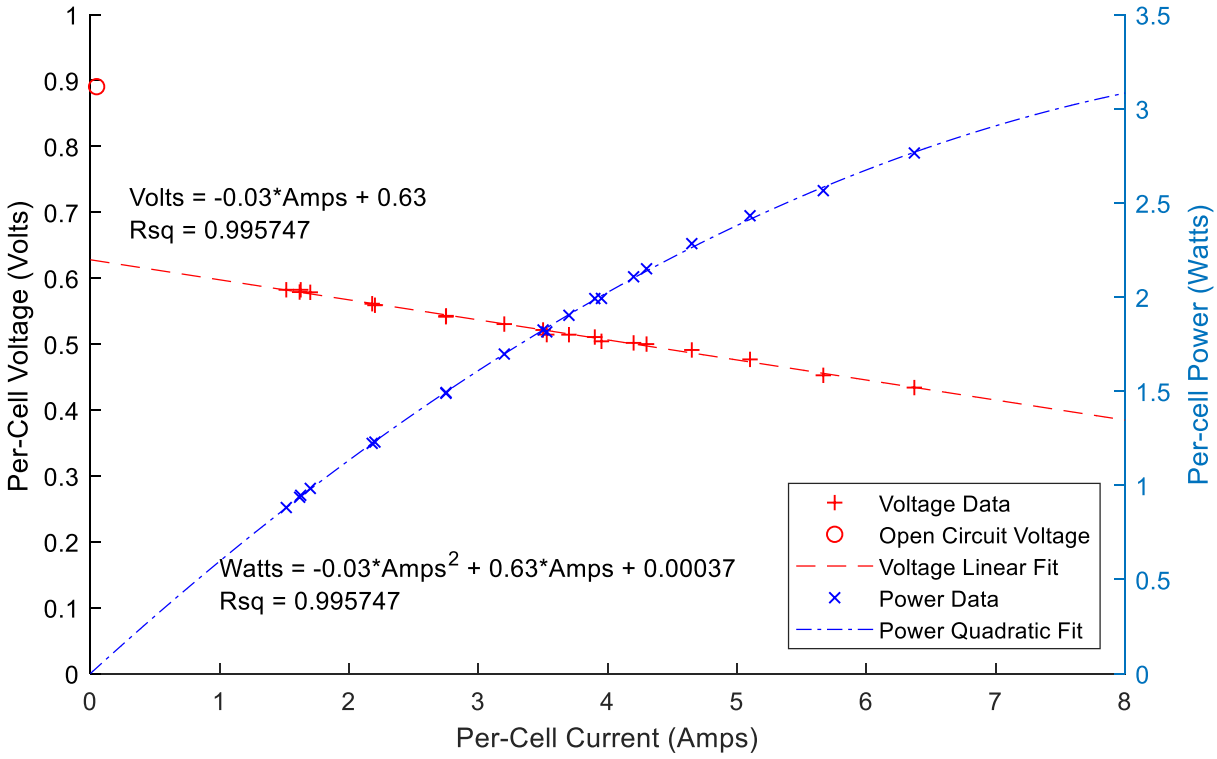

Figure 55: Per-Cell Polarization Data and Fittings for SOFC APU, incl. Power Output. Uses last-minute data from experiments on 11/10/17 1/3/18, and 4/24/18.

A linear fit is used because the APU's control system limits access to the linear portion of the V-I curve. As a result, the inherent ohmic resistance of the cell can be measured but it is not possible to measure the activation overpotentials associated with the low-current portion of the V-I curve or the concentration overpotentials associated with the high current portion of the V-I curve. In addition, we note that the preferred operating regime for the fuel cell is on the lower-current side of the peak of the power curve, so it makes sense that the control system restricts operation to this region.

In terms of fulfilling our original goals of characterizing the performance of the fuel cell, Figure 55 provides an initial range of responses for the limited range of

operating parameters available to the un-modified APU. Further characterization will require disassembly of the APU (to disentangle balance of plant loads from the SOFC stack) or other equipment such as electronic impedance spectrometry measurements to clarify different components of the SOFC electrochemistry.

10.6 Improvements for Future Data Collection

The lab-scale gas turbine-APU hybrid will be difficult and expensive to run for long periods of time which, behooves us to find ways to predict performance at an operating condition without having to wait for the system to equilibrate fully. While replacing the load bank with a constant current load could help, it would only do so if the APU's equilibration time scale is of similar length or shorter than that of the load bank. This is unlikely given that the APU is substantially larger than the load bank so other strategies will likely be required.

10.6.1 Establishing Convergence

For the purposes of investigating the electrochemical properties of GT-SOFC systems, we need to establish a definition for when the fuel cell stack (and eventually the entire hybrid system) has reached equilibrium. Considering that without infinite time we don't precisely know what the equilibrium condition will be a priori, we require a practical estimation that will be reasonably close. The simplest method is to simply allow the SOFC to operate at a single condition for an extended period, but long operating times are not always feasible.

For a given system, we can attempt to establish a reasonable timeframe or rate of change that, during the run, we can determine a system to be converged 'close enough' to the equilibrium value. The specific means of establishing the rate of change and/or an appropriate timeframe will depend on the physical size, thermal mass, and electrochemistry of the system, but for our purposes here will be determined empirically from the range of data already collected.

Consider Figure 56 which plots the voltage and current time histories collected from all experiments, with some spurious data omitted. In particular, data were removed if they were collected while the battery was charging (in this case defined to be a current load greater than a minute-averaged 0.1 Amp), thus changing the load over time. We also removed one final spurious experiment which experienced a temporary reduction in internal load during the run from a change in demand from the balance of plant.

The remaining time histories are averaged over one minute intervals (as in Figure 52) and then normalized by the final minute's data which usually occurs at run times between 20 and 30 minutes, although some experiments have lasted an hour or more. The resulting curves show a maximum variation of 1% of voltage and 8% of current measurements from start to finish for all remaining experiments (Figure 56). Figure 56 also includes the power output of the stack during all remaining experiments.

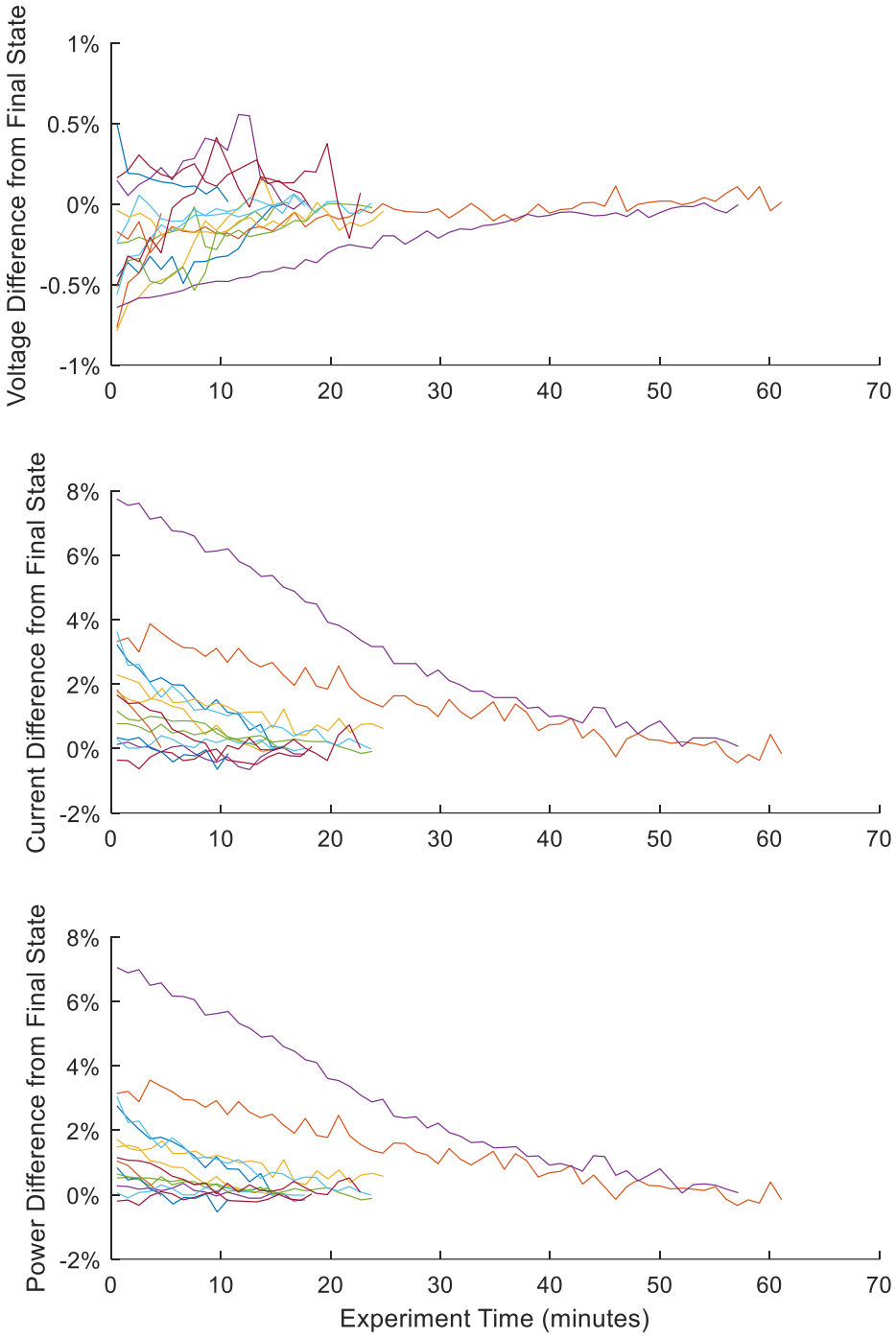

Figure 56: Voltage (upper), current (middle), and power (lower) time histories. with minimal battery charging, normalized against values at end of each experiment. Data

represent averages over one minute and are normalized by values at end of each experiment.

Even if the battery load is missing, we do see some change in stack power output over time. This could be due to heating of the load bank (with higher temperatures generating higher resistances, and so lower current demands). Encouragingly, the variation is relatively small in most cases. However, the percent variation from the final reading isn't necessarily a fair representation given the different lengths of time of each experiment—most, but not all, are approximately 20 minutes. The greatest differences, unsurprisingly, are seen in the longest experiments with time to drift.

If we instead consider the approximate slope over time, from Figure 56 we can tell that for even minute-to-minute data points, the slope between them can vary drastically. If we extend the averaging time to two minutes, and evaluate the slope between points, we can identify the point at which a threshold slope (here arbitrarily 0.1% variation per minute) is reached. These points are represented by the black dots on each time history line in Figure 57.

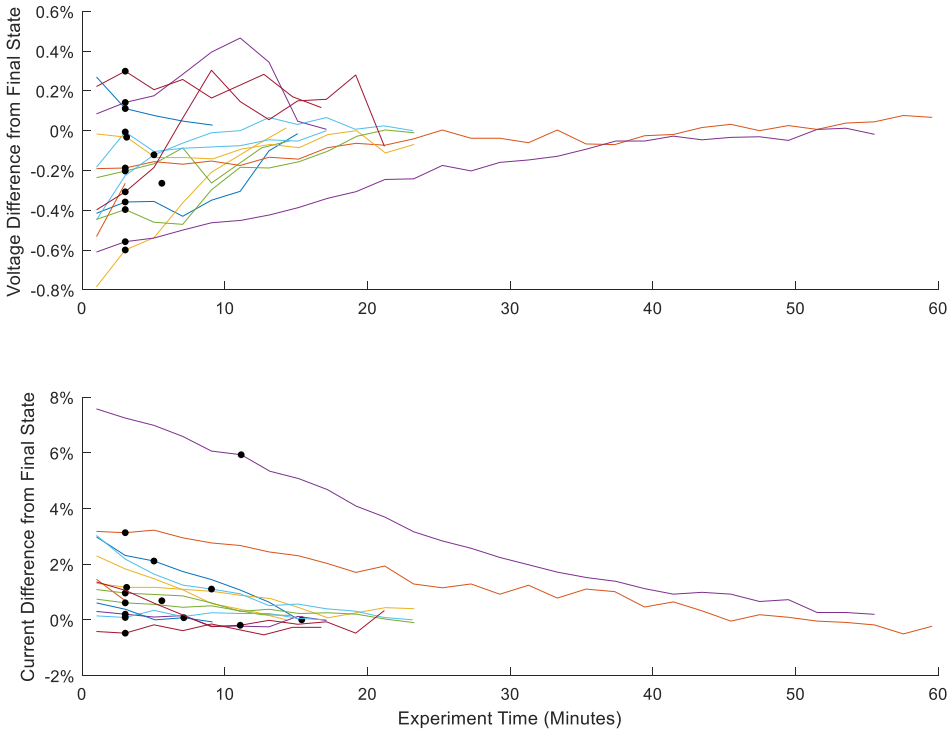

Figure 57: Voltage (upper) and current (lower) time histories with minimal battery charging, normalized against values at end of each experiment. Black dots indicate "converged" slopes of less than 0.1% change per minute. All values averaged over two minutes.

The proposed rule is satisfied within five minutes in all cases for voltage measurements. For current measurements, this rule is satisfied within approximately 15 minutes in all cases although the value is seen to drift by at least 6% as the system equilibrates in the worst case shown here. The rules set for convergence may be modified with different target slopes or averaging of data points, but the qualitative results appear to be similar, in that most cases generate shallow slopes, though individually even average values appear to not generate wholly smoothed curves. Overall, the changes over time in voltage are small (<1% change over the course of

an experiment) compared to the changes in current output. As such, voltage values may be acceptable as an averaged measurement over a short period of time, but corrections may be useful for current values. “Convergence” via a slope measurement furthermore does not reliably indicate an equilibrium value and, due to the noise in the measurements, still requires multi-minute measurement periods which are not ideal for the eventual use in a laboratory-scale GT-SOFC demonstrator. As such, in the next section we will see if there might be a way to predict equilibrium performance more quickly using nonlinear exponential decay fitting.

10.6.2 Predicting Convergence via Exponential Decay Fitting

Regression analysis using exponential functions has been used to model the transient response of polymer electrolyte membrane (PEM) fuel cells [93] so we will use this approach to try to predict equilibrium operating conditions without waiting for the system to equilibrate. A least-squares nonlinear solver in MATLAB was used to fit a function of the form $f(t) = Ae^{-bt} + C$ to the data where C is the function value at $t = \infty$ or the asymptotic value. The fitting algorithm was run over all measurements taken for experimental trial undistorted by the battery charging (as for Figure 56) to find the best least-squares fit values. If the fit results were outside of reasonable ranges (negative values for either voltage or current, or values above 50 volts or 12 amps) then the initial values provided to the fitting algorithm as the starting point of the fit were altered, and the algorithm re-run. The initial values of A, b, and C are the same for each fitting. The value of C can also be matched to be the

value of the first data point, but this yields similar results to providing the same initial values every time, while also preventing the solver from taking the initial value for C as 'sufficiently converged' already.

The results are shown in Figure 58, with the data from each experiment plotted with its fitted curve. Most of the fits appear satisfactory (visually) although in most cases the overall exponential decay characteristics are not strongly evident relative to the noise level of the data. The value C associated with each fitted curve is assumed to be the "extrapolated" equilibrium value.

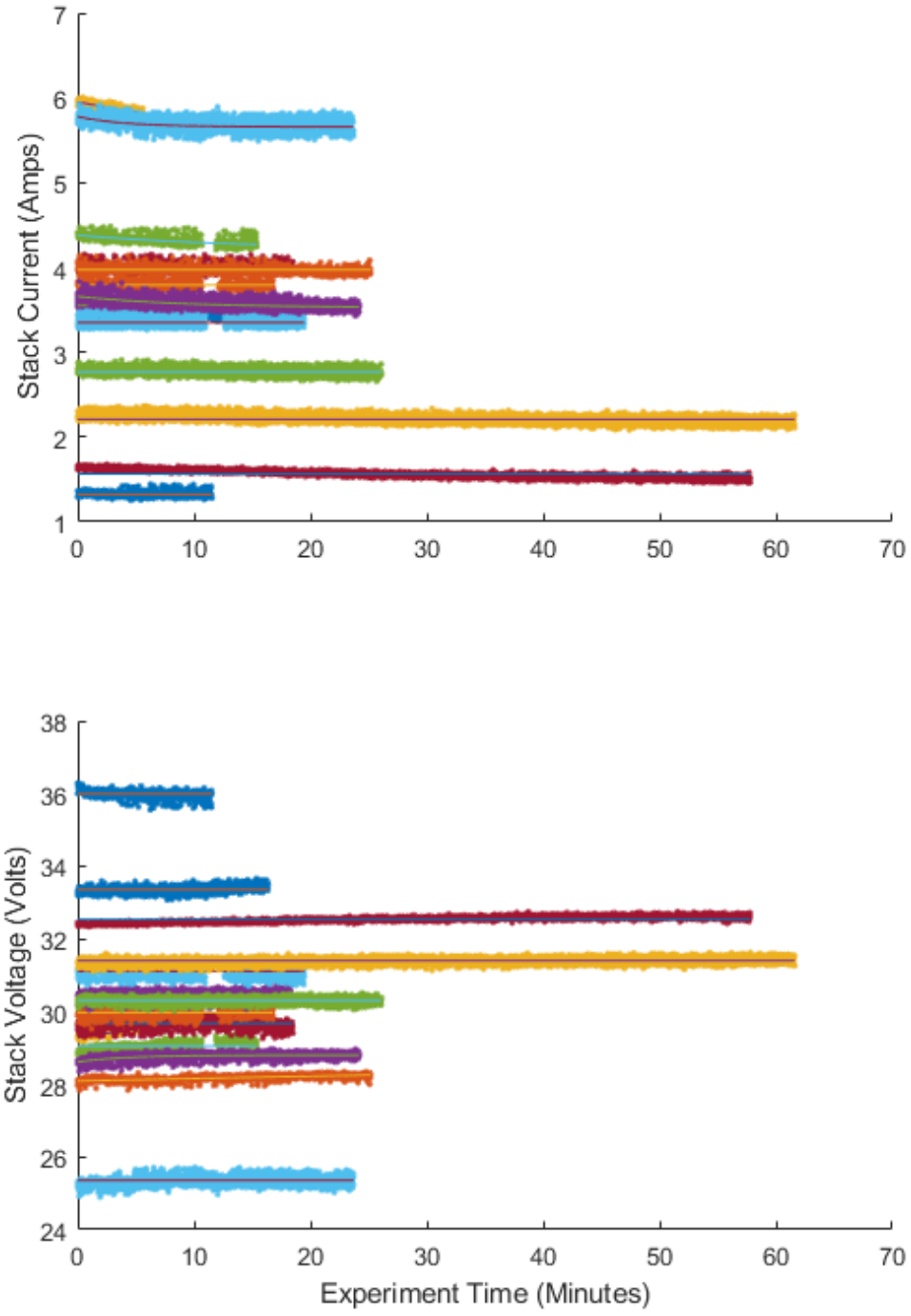

Figure 58: Subset of Experiments Current and Voltage data with overlaid curve fits

The extrapolation process is most useful if it only needs to be applied to the initial data collected. As such, we can repeat the curve fitting process for the first minute of data collected, or about the first 93 data points of each experiment.

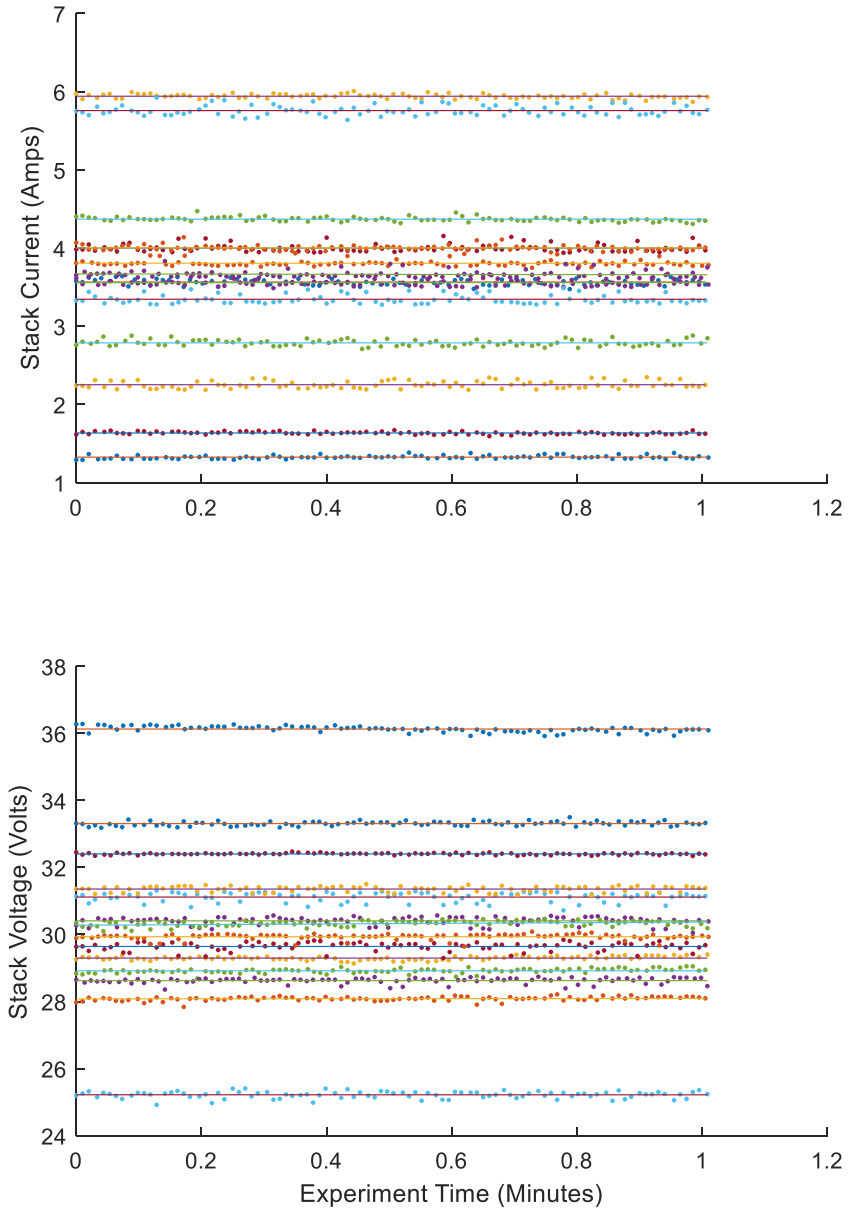

Figure 59: Subset of Experiments' first minute of current and voltage data with overlaid curve fits.

The results again appear qualitatively linear, which is not unexpected for the short timeframe considered. The values of C generated by the fitting algorithm in for all data available (~15-60 minutes depending on experiments available) tend to be very similar! The question is whether the extrapolated equilibrium values approach the true equilibrium conditions. Figure 60 plots normalized last-minute average ($\bar{V}_{last,norm}$), 1-minute extrapolated ($V_{ex1,norm}$) and all-data extrapolated ($V_{exAll,norm}$) voltage and equivalent current values, all normalized (as shown in Equation (29)) by the average value of the first minute of data collected ($\bar{V}_{first}$) since all data collection regimes will have this data available.

$$\bar{V}_{last,norm} = \bar{V}_{last}/\bar{V}_{first} \tag{29}$$

Lines are drawn to connect the last-minute values and their associated extrapolations from the same experiment to show drift between the methods.

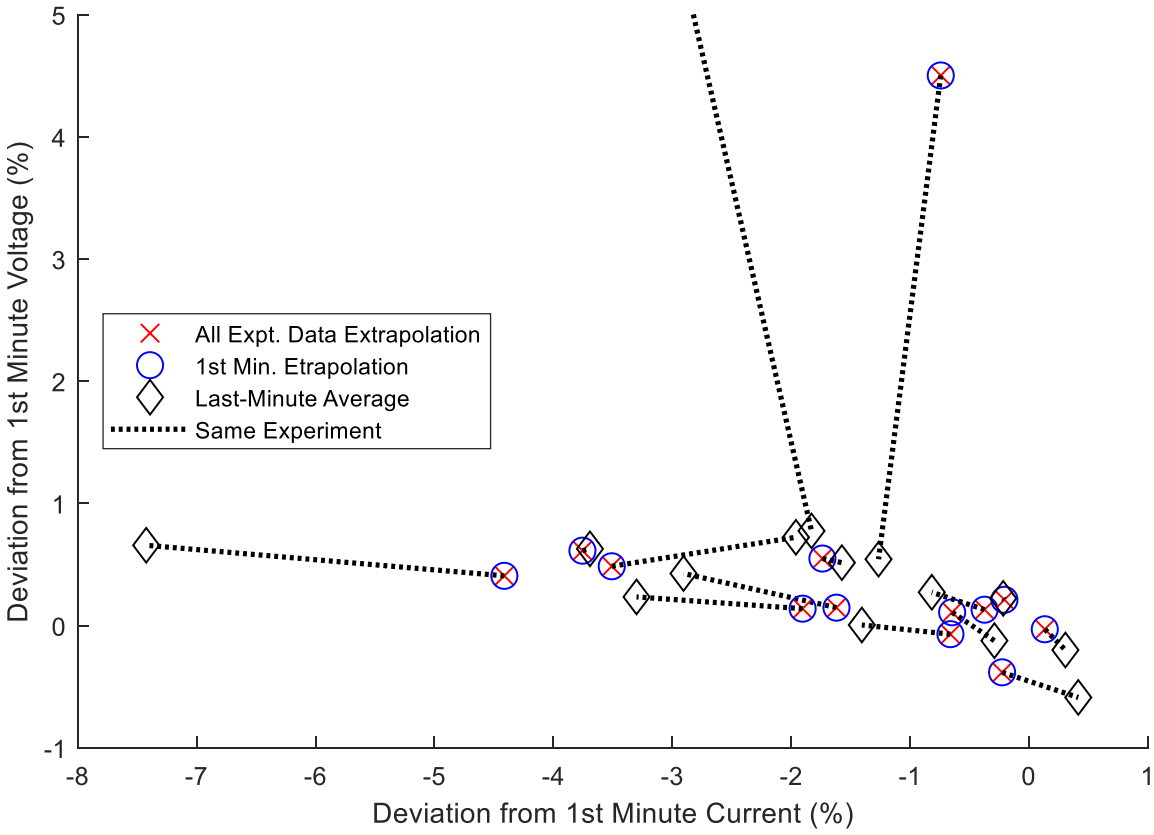

Figure 60: Comparison of extrapolation and first- and last-minute values from subset of experiments

Presuming that the system is equilibrating such that the final minute of data are closer to equilibrium than the first minute of data collected, with a few exceptions the extrapolations provide a more "accurate" value than the first-minute mean, though they usually are still off by at about 1-2% of the current and <1% of the voltage. The exceptions are significant, with one disagreement each between final-minute and extrapolated voltage values of 4% and 30% (off chart). Improvement to the fitting rules may adjust for these outliers in future, as there wasn't any immediately apparent

explanation for the discrepancy. There is also no immediately discernible trend of the extrapolations overshooting or undershooting the last-minute value.

In both the cases of establishing convergence to the equilibrium and of predicting convergence values, the data are obscured by the varying loads and adjustments of the balance of plant, control system, and load bank. Future work will involve disconnecting the SOFC stack from the balance of plant, and improvements to the load bank for constant-current and automated data collection may improve the quality of the data collected such that the processes outlined in this section may yield more reliable results. As of this time however, practically speaking simply averaging the initial measurements will still fall within ranges of $\pm 2\%$ for voltage values and worst case $\pm 10\%$ for current value, as compared to measurements taken at long times ($\geq$20 minutes) thereafter. Extrapolations using first-minute data will generally provide an improvement towards equilibrium, but not yet reliably with the current fitting method.

Overall, the results presented previously in Figure 55 capture the performance of the AMI APU over a variety of loads and may be sufficient for developing a preliminary model of the bench-scale GT/SOFC hybrid. However, all of the experiments have been conducted at atmospheric pressure whereas pressures in the gas turbine's combustor are ~ 3 atm. While there are crude methods for extrapolating these results to higher pressures (such as tuning the model to match results at the lower operating condition), more measurements at elevated pressures are required. Also of interest would be finding ways to infer equilibrium voltage and current from

time histories that are not converged and measuring more detailed aspects of the fuel cell's performance like ohmic, activation, and concentration losses. Measuring the latter may be easier when the system is disassembled but is not possible now while the APU control system is activated, and could entail analysis using electronic impedance spectroscopy if available to generate equivalent polarization curves for comparison of results.

11 Preliminary Design of a Bench-Scale GT/SOFC Hybrid

Finally we will consider an initial NPSS model of a laboratory-scale GT-SOFC hybrid based on the small turbojet engine described in section 6.3.3 and the APU described in Chapter 10. The results provide insight into how to design the prototype by indicating what conditions (i.e. pressure, temperature, flow rate) will need to be accommodated where. This section is based closely upon a previous conference paper by the author.[4]

11.1 GT Model

The full characterization and NPSS model validation for the AMT Olympus High Power system has been addressed in prior work by Vannoy and Cadou [61], with substantial refinements by Vannoy [62] that were not available in time to be included in the integrated analysis. The NPSS model components and system settings produced were used as the basis for conversion into a GT-SOFC, with design parameters provided below in Table 7.

Table 7: Baseline conditions for NPSS model of AMT Olympus HP, adapted from [61]

Parameter	Value
RPM	108,500
Air Flowrate (lbm/sec)	0.99
Compressor Total Pressure Ratio (P_{03}/P_{02})	3.7
Compressor Efficiency	0.75
Fuel Type	Jet-A
Fuel Flowrate (lbm/sec)	0.0262
Turbine Total Pressure Ratio (P_{04}/P_{05})	2.148
Turbine Efficiency	0.729

These model components include a compressor map provided by the manufacturer, as well as a scaled low-pressure turbine map developed by General Electric as part of the NASA Energy Efficient Engine (E^3) program.[89], [94] The NPSS turbojet model schematic used for the design of the bench-scale model is shown in Figure 61. The AMT Olympus HP is a single-spool turbojet that has no bleeds or fan bypass. Air flows from inlet to compressor, mixed with fuel and combusted before driving the turbine and exiting the nozzle to produce thrust.

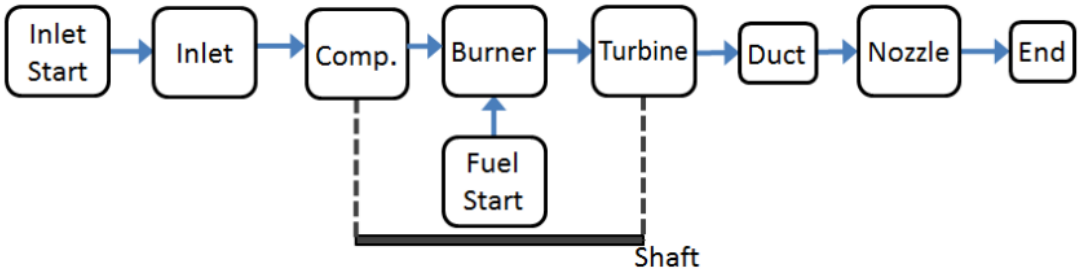

Figure 61: NPSS Schematic for AMT Olympus High Power. Reproduced from [62, p. 38]

Each of the main elements, the Inlet, Combustor ("Burner"), Turbine, Nozzle, etc. function identically to those described in Chapter 8.1. The NPSS model was validated against an AMT Olympus HP set up on a thrust stand in the laboratory, pictured in Figure 62.

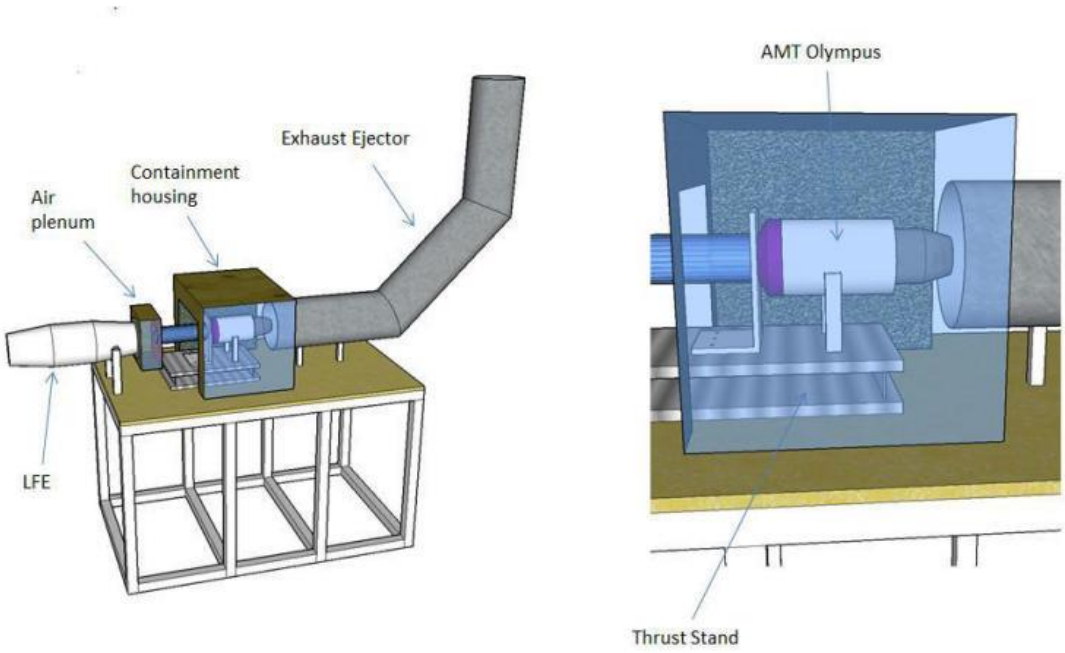

Figure 62: AMT Olympus HP test facility, reproduced from Vannoy.[61]

Measurements taken using the pre-instrumented "University Configuration" as well as an experimental thrust stand were used to improve the fidelity of the NPSS model.

The instrumentation included temperature (thermocouple) and pressure (transducer) sensors at the various stages of the engine cycle. Additional measurements of air flow rate, fuel flow rate, and thrust were provided by the thrust stand setup. A comparison between measured and predicted inter-stage temperatures and pressures is shown in Figure 63. The results show that the NPSS model predicts temperatures and pressures to within 6% of the measurements.

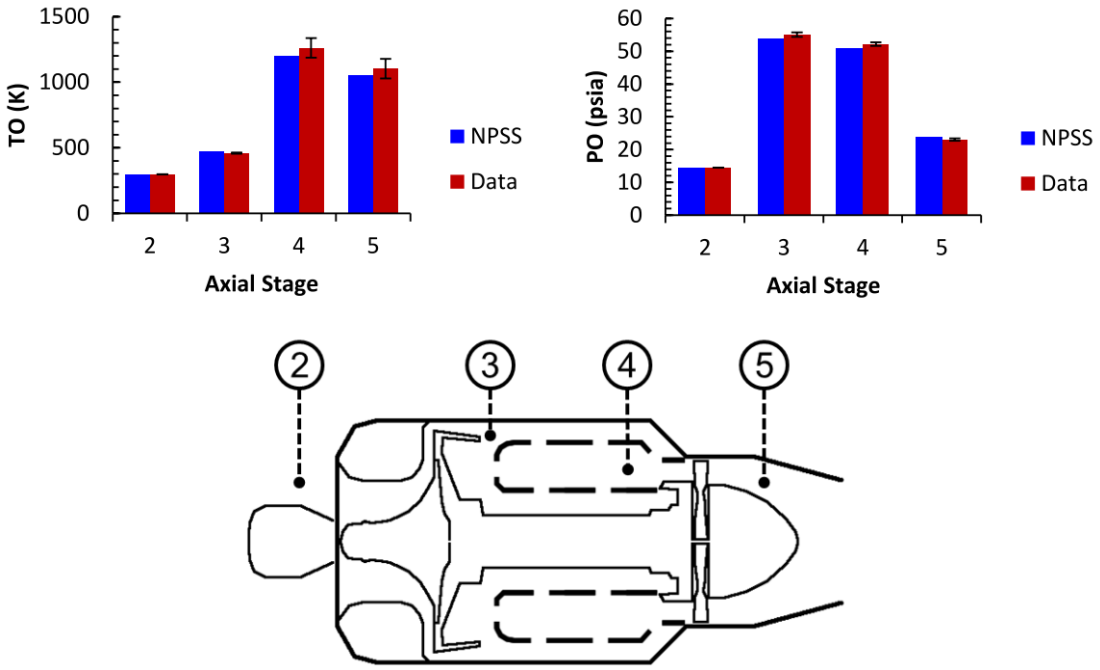

Figure 63: Comparison of predicted stagnation temperatures and pressures along the axial stages of the AMT Olympus GT at full throttle. Reproduced from [61]

Airflow rates tend to be overestimated by approximately 15% for any given engine speed, as shown in Figure 64. In the same figure, the fuel flow rate is observed to be within the margin of error at most conditions—the large error range generated at full throttle is suspected to be an artifact of the gravimetric means of flow rate determination, as at high power the test stand vibrates substantially while the sampling rate is locked to 10Hz.

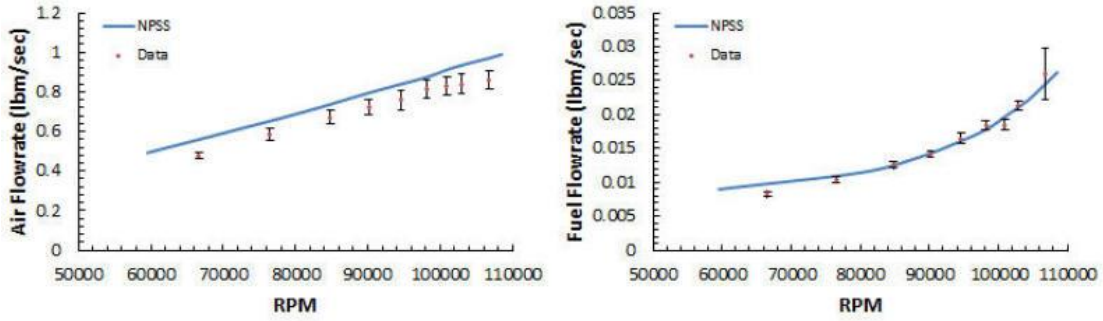

Figure 64: Air flow rate (left) and fuel flow rate (right) measurements and model predictions as a function of engine RPM. Reproduced from [61]

Additionally, Figure 65 illustrates a general underprediction in thrust of an average of 2.68lbf, and so a corresponding overprediction of specific fuel consumption (SFC) of about 0.32 lbm/lbf-hr.[61]

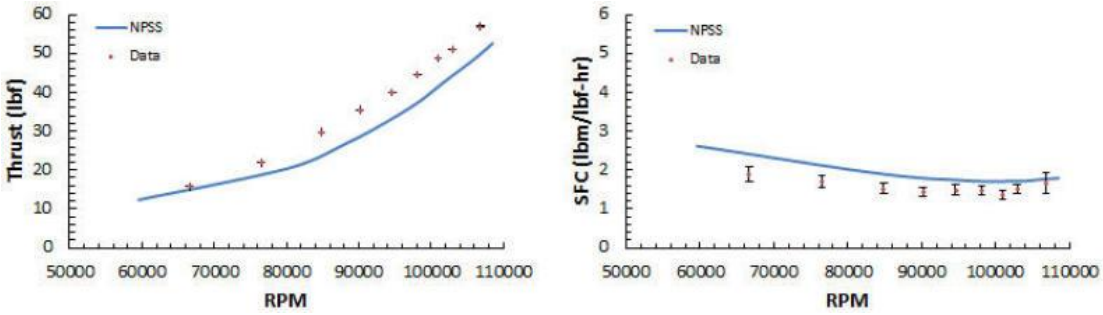

Figure 65: Thrust measurements and predictions as a function of RPM. Reproduced from [61]

The NPSS GT model as presented here matches the one used in the subsequent GT-SOFC analysis in later sections.

11.2 SOFC Model Modifications

Aside from geometric scaling, the underlying fuel cell assembly model is identical to the one described in section 8.5. Previously, analyses of GT-SOFC systems using the NPSS model were performed under the simplification that the circumferential stacks are large enough to be treated as flat, essentially "unwrapped" from the engine—this geometric assumption is less reasonable in the laboratory-scale gas turbine because its radius of curvature is much smaller. However, the first lab-scale system will not use a custom-designed conformal stack and will instead divert air to the APU's tubular 'stack' located outside but adjacent to the engine. The larger problems will be thermal inconsistencies arising from the fact that the NPSS model assumes rectangular cells whereas the APU uses tubular ones and that heat transfer is only being considered through the top and bottom of each unit. However, these simplifications are acceptable since the current purpose of the integrated NPSS GT-SOFC model at this stage is to approximate requirements for operating conditions. Future work will improve these geometric approximations, as well as adapt the fuel used by the SOFC from Jet-A (shared by the engine) to propane to more appropriately model the Ultra-AMI SOFC APU.

11.3 NPSS GT-SOFC Integrated System Model

The NPSS schematic for the lab-scale GT-SOFC prototype is provided below in Figure 66. As before, the SOFC assembly components of splitter, reformer (CPOx),

fuel cell inlet, SOFC, and combiner in placed into the flow path between the compressor and combustor of the gas turbine.

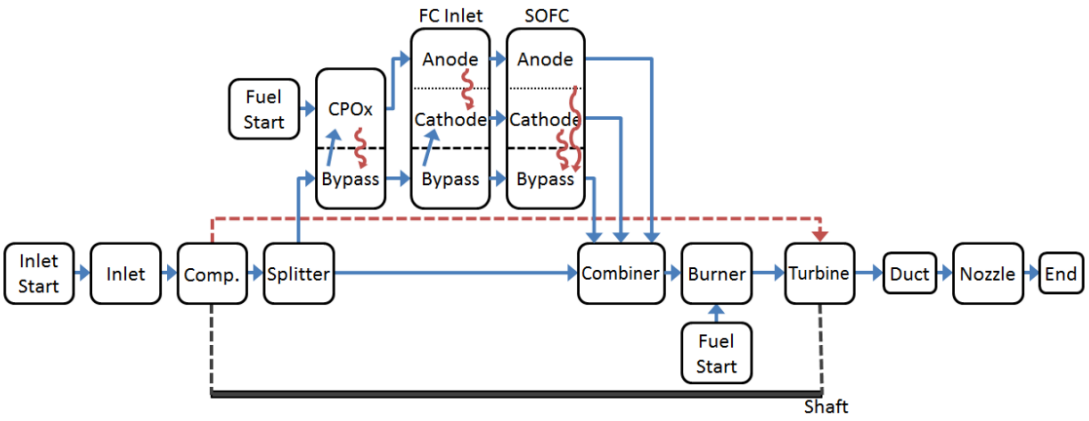

Figure 66: Lab-scale GT-SOFC NPSS schematic; reproduced from [4]

For the purposes of this chapter, NPSS was configured to be a 7-layer ($N_{rep} = 7$) stack with eight units (for a total of 56 SOFC 'tubes'), with total dimensions in centimeters of $10.16 \times 8.4 \times 7.22$, as shown in Figure 67 below, to better approximate the estimated size of the APU tubular SOFC units. The aspect ratio of the channels was designed to match an equivalent active area to volume ratio of a tubular channel with the diameter of a pencil (~0.6cm), as described by the manufacturer. Additionally, 56 CPOx units, already modeled as tubular, are given the same diameter, and the fuel cell inlet shares the same proportions as the SOFC stack.

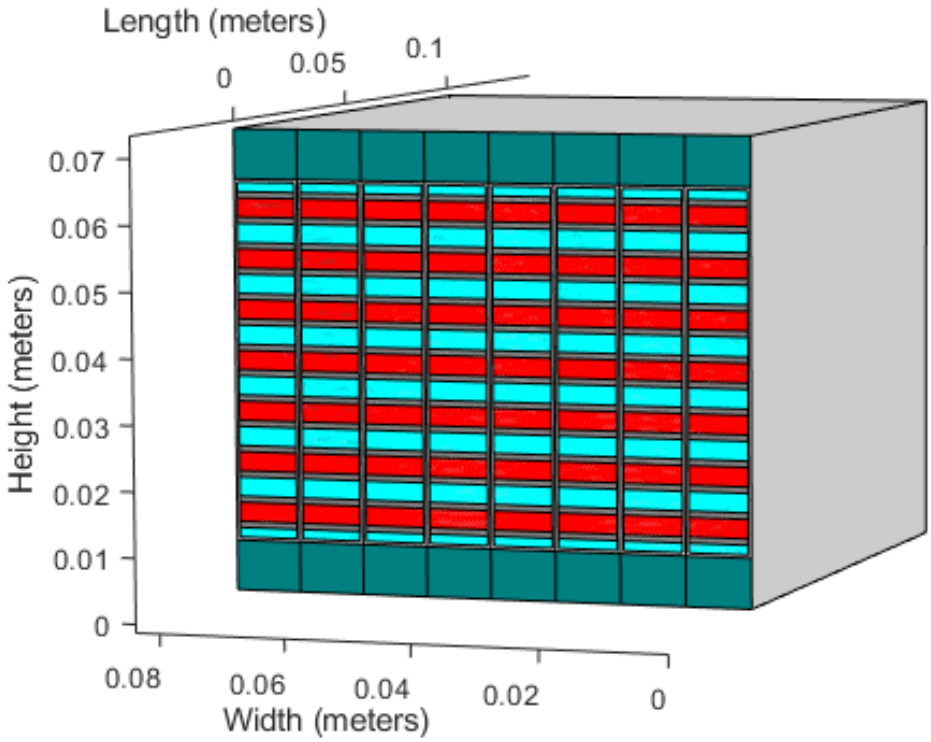

Figure 67: Demonstrator sizing model SOFC stack spatial representation, anode channels in red, cathode channels in cyan, and insulation in dark green

Mechanical, thermal, and electrochemical parameters of the fuel cell components (channels and MEA) are the same as in prior work. However, the engine being considered here is much smaller than the engines considered in prior work with a maximum mass flow rate of approximately 0.45 kg/s. As a result, far fewer unit cells are needed.

11.4 Results

11.4.1 Model Validation

While the electrochemical model used in this work has been previously validated,[80] a limited validation of the GT-SOFC model was performed by solving the model for a range of stack voltage conditions to generate a polarization curve for the integrated system while at full throttle at sea-level-static (SLS, i.e. laboratory) conditions, shown in Figure 68. The intent is to show that "reasonable" results are produced, rather than attempt to model a specific SOFC system at this point in development.

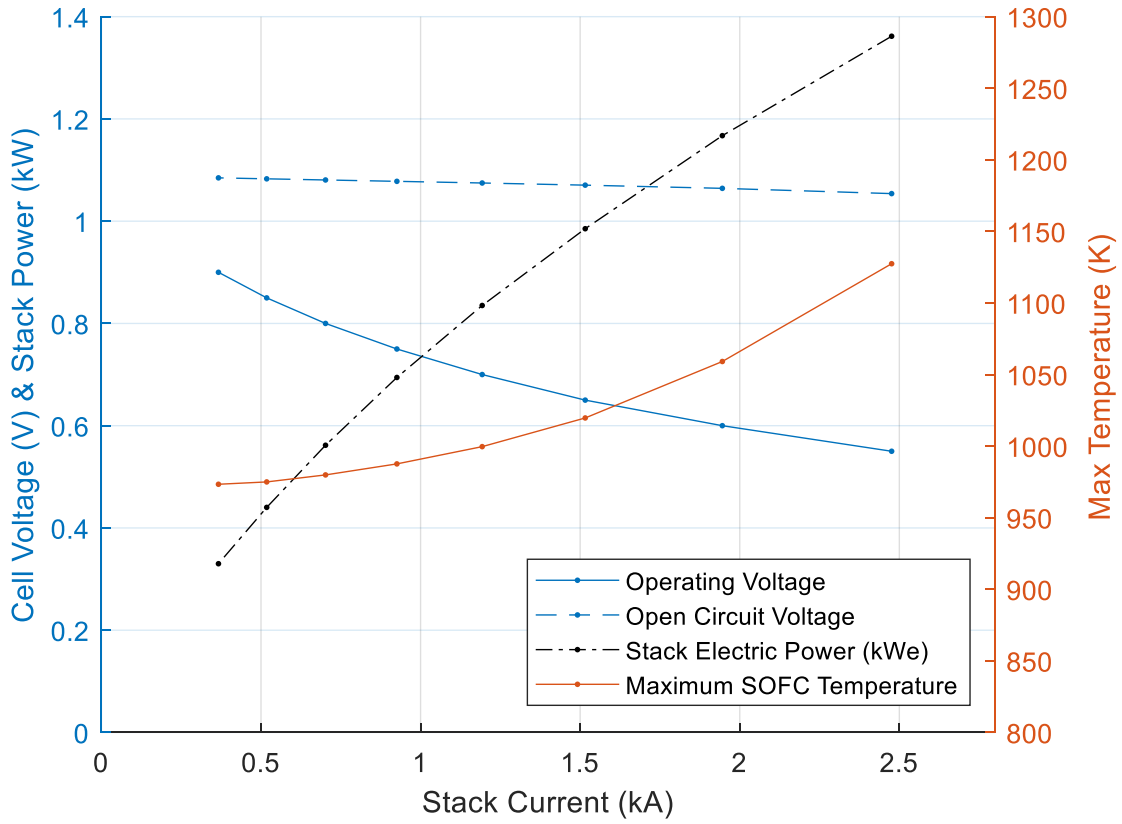

Figure 68: GT-SOFC Demonstrator Model Polarization Curve for full-throttle operation at sea-level-static conditions, including also stack power, open-circuit voltage, and maximum temperature for varying stack current

The polarization and power density curve found is qualitatively consistent in shape and magnitude with what is found in other SOFC MEAs.[77] Observe also that the operating temperature increases with current density due to increased (primarily ohmic) overpotential losses. The open-circuit potential is shown to vary only slightly as the temperature varies such that it has not strongly impacted the shape of polarization curve.

Down-the-channel variation in flow composition is also calculated by the model at 100% throttle provided below in Figure 69. The trends observed are

consistent with what one would expect in a fuel cell—fuel, here Jet-A reformed into a syngas of CO and H_2 is progressively "burned" into carbon dioxide and water along the anode.

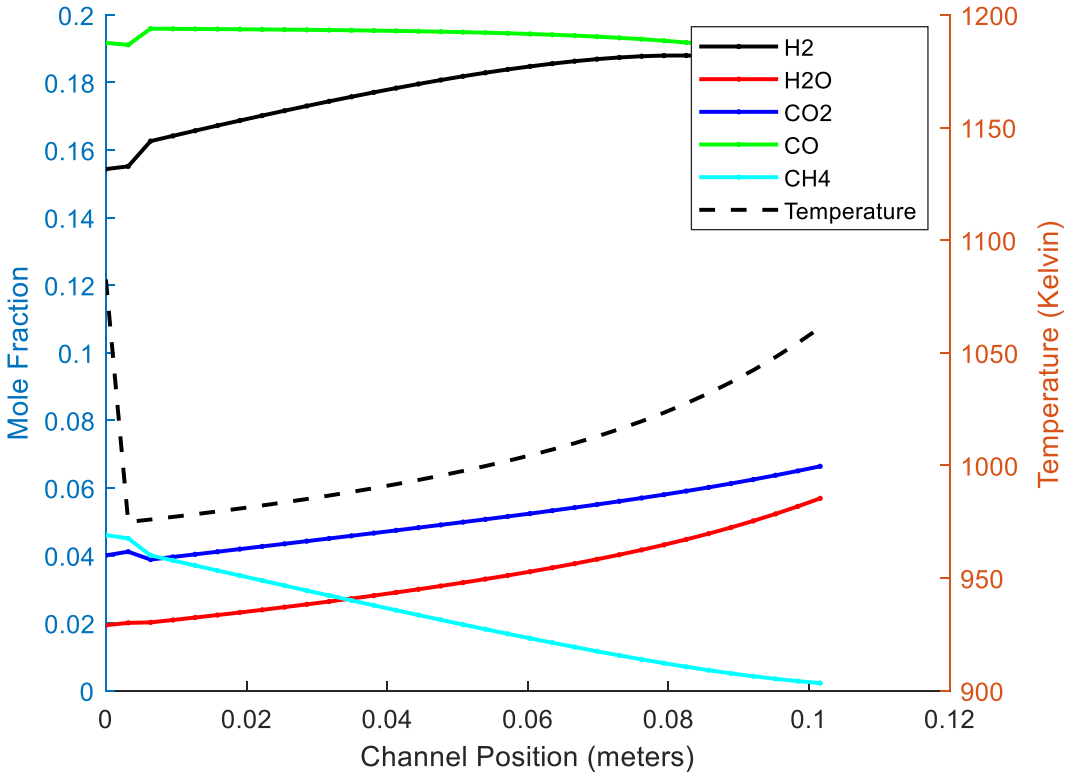

Figure 69: Down-the-channel composition of SOFC anode flows at 100% throttle

In this geometry, the inlet component does not fully match anode and cathode flow temperatures, causing a temperature drop immediately after the inlet after which reactions in the channel generate higher temperatures further down the channel. The temperature shock in the real APU is mitigated by preheating of the cathode flow through the combustor, which is not currently a feature of the computational model.

11.4.2 Preliminary Design

Figure 70 provides the initial sizing design for the lab-scale demonstrator hybridized with a model approximating the COTS APU discussed in Chapter 10. The conditions shown are for 100% throttle at sea-level static (SLS) atmospheric conditions. Figure 70 shows a scaled outline of the AMT Olympus HP engine along with a to-scale overhead view of the SOFC assembly with the CPOx and fuel cell inlet integrated as a single component. The SOFC cell voltage is set to be 0.6V as in previous work, though trades may be made for between power density and efficiency by varying this value according to the polarization curve in Figure 68.

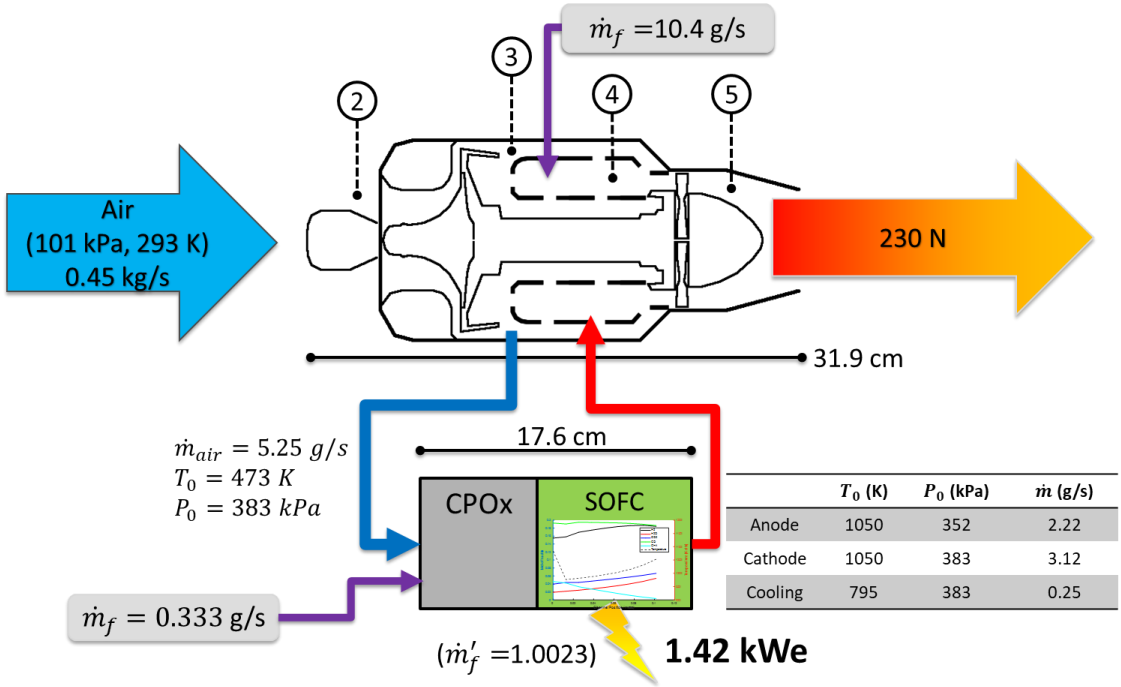

	T_0 (K)	P_0 (kPa)	$\dot{m}$ (g/s)
Anode	1050	352	2.22
Cathode	1050	383	3.12
Cooling	795	383	0.25

Figure 70: Preliminary design for GT-SOFC laboratory demonstrator, operating at 100% throttle

There are several conclusions that may be drawn from the design as provided. First is that the power output is more than four times greater than the real-life APU (1.42kWe vs. 300We). This is likely due to the higher pressure conditions inside the cell (~3.8 atm) and a greater fuel flow rate, as well as the lack of balance-of-plant demands and other non-idealities.

Second, the fuel cell assembly requires a relatively small proportion of air from the gas turbine, slightly over 1%. Additionally, the overall relative fuel flow rate (1.0023) is less than 1% more than the gas turbine alone for the same performance. This value is nearly identical to that a mechanical generator producing the same amount of electric power, but this is almost certainly due to the relatively low amount electric power requirement—however the usual metric of electric power fraction is additionally difficult to ascertain for SLS conditions since the gas turbine is producing zero power while held in place on a thrust stand.

Finally, we may note that there are three different exhaust streams from the fuel cell assembly with anode and cathode temperatures only 50K short of the combustor exhaust temperature of 1100K and essentially no substantial pressure losses for the cathode and cooling air channels. A current problem to be resolved is the lowered pressure of the anode flow (which underwent combustion) which will require pressure matching of some kind in order to integrate with the higher-pressure gas turbine combustor.

12 Conclusions and Future Work

12.1 Conclusions

12.1.1 Summary

Over the course of this thesis, several related projects were pursued surrounding the concept of GT-SOFC hybrid systems for aircraft. Building off of prior work to develop the integrated GT-SOFC model, we have investigated the effects of drag – both induced (due to the extra mass of the components) and profile (due to the protrusion of fuel cell components into the air flow in pylon-mounted configurations) on the efficacy of GT-SOFC hybrids in regional transport jets and high-altitude, long-endurance aircraft like the RQ-4 Global Hawk. The results have demonstrated the greater impact and sensitivity of the outfitted aircraft to profile drag rather than drag penalty represented by the additional mass alone. This conclusion allows us to prioritize design decisions to minimize profile drag. Furthermore, a more-detailed sensitivity analysis has been performed or revised for several system characteristics.

However, the exploration of drag was still wholly theoretical, and performed entirely within NPSS. Looking to the need to validate our modeling efforts against a real-world system, we collected and characterized COTS components to serve as the basis of a demonstrator system. The COTS APU was characterized as part of this work by measuring the stack's polarization curve. In the process, methods of operating the fuel cell and analyzing the available output for effective data collection

were explored, yielding an initial polarization curve and providing guidance to speed up future data collection activities.

Looking ahead to the integration of the COTS GT and SOFC APU systems in a bench-scale system, a model of such a system was created in NPSS in order to guide the development of hardware when it is finally time to "bend metal" to create the prototype GT-SOFC.

12.1.2 Author Contributions

In pursuing the research discussed in this thesis, the author made several personal contributions to the project. These have included improvements to the modeling of external aerodynamic drag (both induced and profile drag) and investigations into the role these penalties play in limiting the performance advantage of integrated GT-SOFCs in aircraft (Chapter 9). Additionally, the author has expanded and corrected the associated sensitivity analyses necessary to confirm the ability of the model to generate meaningful results. Through these efforts, the author has helped to identify aerodynamic drag as a key performance limiter for GT-SOFC systems in aircraft.

Looking towards the development of a laboratory-scale GT-SOFC demonstrator, the author was responsible for the design, construction, and operation of an experimental apparatus to measure the performance of an off-the-shelf SOFC APU that will later serve as the basis of the SOFC assembly in the demonstrator system. This process included both hardware and software design to devise a load bank and data collection method and routine, using a hobbyist Linux computer and

scripting to take the place of LabView for a non-standard interface. The author has collected many hours of data produced by the apparatus and successfully processed them into the results presented in Chapter 10, characterizing an SOFC APU. As part of this analysis, the author has devised more rapid procedures for measuring SOFC APU performance without having to wait for full equilibration, which will enable data collection from an integrated GT-SOFC on a reasonable timescale.

The SOFC APU was also approached from the direction of simulation, as the author has developed an NPSS model of the SOFC APU and integrated the model with an NPSS model of a COTS turbojet engine, using the resulting integrated model to create an initial design for the lab-scale demonstrator system (Chapter 11). The author also analyzed the integrated model for its relative performance against a traditional turbojet outfitted with a mechanical generator for electricity production.

Finally, the author undertook several projects to improve the NPSS GT-SOFC model code base, including the transfer of the project to rigorous version control and project tracking, enabling easy access/distribution to sponsors and collaborators. The author has also developed tools to minimize the impact of the currently slow (often weeks of runtime) calculation speed. In particular, the author has replaced custom viewer files in favor of a dump of all variables to disk, building on that standard capability with scripts to sort and tabulate the results for easy processing in analysis software such as MATLAB. Additionally, this method retains the option to retrieve any new variable used by the calculation immediately without having to re-run the entire simulation just for adding an entry to the Viewer file. Also, convenience

features such as runtime, notes, titles and minor speed improvements were added by the author wherever possible.

12.2 Future Work

There are several future directions for research into GT-SOFC systems for aircraft. Perhaps most interesting is how to put the electric power—so far only generated for secondary purposes—back into the propulsion system. Should this be used to the compressor or distributed fans throughout the aircraft? Part of answering this question will require new models for electrically-driven components.

Additionally, building off the preparatory work performed here, further characterization and modeling are necessary for the COTS components for the GT-SOFC demonstrator. Improved and rigorous data collection at a variety of operating temperatures and pressures will be most useful in providing a model validation target. This goal may require automated constant-current testing equipment and eventually deconstructing the operating APU to fully separate the effects of the control system and its attendant system load. At the same time, the NPSS models should be improved to allow for greater flexibility in system configuration and the ability to model multiple fuels as would be used in the first bench-scale integrated systems (propane for the COTS APU and Jet-A for the COTS GT).

Finally, future work should investigate the composition and temperature of the FC exhaust in order to understand its effect when reintroduced into the combustor. For example, will introducing hot anode exhaust containing unreacted H_2 back into

the combustor lead to potentially damaging hot spots? Or alternately could the exhaust be used to reduce thermal NO_x formation by enhancing flame stability, enabling operation at lower overall equivalence ratios.

13 Appendices

13.1 Gas Turbine Fundamentals[2]

Gas turbines employ the Brayton cycle to convert energy in fuel to mechanical power either through shaft work or propulsive power via the transfer of momentum to flow through a nozzle.[95, Ch. 4] The precise balance of these outputs is dependent on the application: A turboshaft engine will put the vast majority of power into torque, while most power in a turbojet engine is expended to produce thrust.

A gas turbine generally consists of five main components; an inlet, compressor, combustor, turbine, and nozzle. The can be arranged in different ways, but in a simple turbojet they are arranged as illustrated in Figure 71.

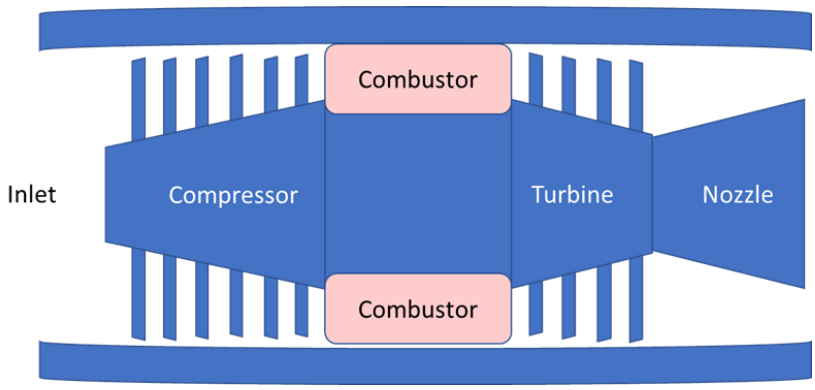

Figure 71: Layout of Axial Gas Turbine

[2] Much of the material in this section is drawn from the more complete and elaborate explanation available in Mattingly, 2006.[95]

In the cycle, air from the environment passes through the inlet, and is raised to a higher pressure inside the compressor at the cost of some invested work. Fuel is added to the pressurized airflow and ignited, adding heat energy (and entropy) to the flow at an approximately constant pressure. This hot flow enters the turbine, which recovers the energy required to run the compressor. The remaining enthalpy in the can be used to produce thrust or shaft power by expanding through a nozzle or secondary turbine respectively. Shaft loads might be a fan or propeller as in a turbofan or turboprop engine, an electrical generator, a hydraulic pump, fuel pump, etc.

A temperature-entropy diagram of the ideal Brayton cycle is presented in Figure 72. The cycle consists of an isentropic compression, a constant pressure heat addition, an isentropic expansion, and a constant pressure heat rejection that occurs in the atmosphere outside the engine.

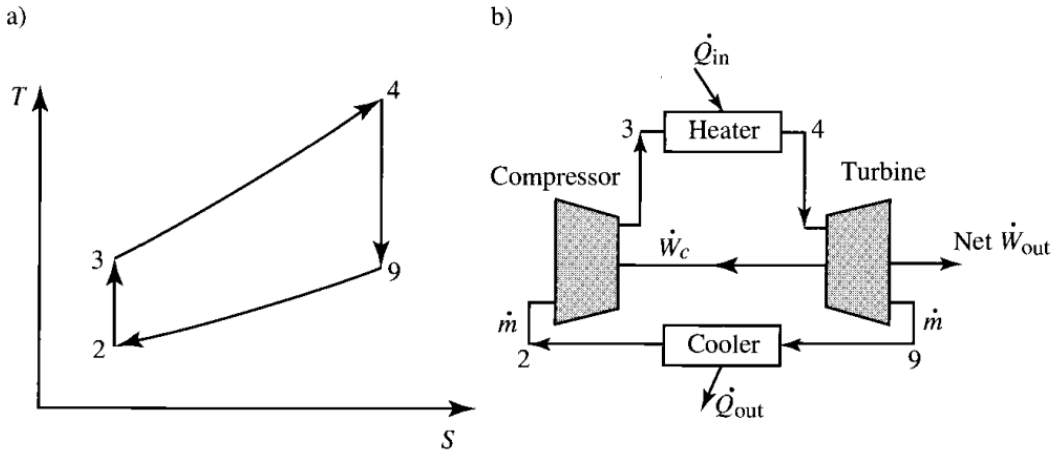

Figure 72: Brayton Cycle Application to Gas Turbine, adapted from [95, Ch. 4]

Practically speaking, the limits on the performance of the gas turbine are the maximum material temperature limit of the combustor and turbine inlet, as well as the compression ratio which is limited by the size and efficiency of compressor components. More important for this work are the effects that variations in pressure and temperature of operation have on the fuel cell portions of the overall system.

13.2 Fuel Cell Fundamentals[3]

Like engines, fuel cells produce electrical power by reacting hydrogen-bearing fuel with oxidizer to produce water and additional products like carbon dioxide. Unlike engines, most of the energy release drives electrons through a potential gradient producing electrical power directly, as opposed to heating a working fluid that does work through expansion. In the fuel cell, reactants flow in two streams (fuel and oxidizer) through adjacent channels separated by walls called the membrane-electrode assembly (MEA). The MEA is made up of three main layers. The outer two layers in contact with the reactants are called electrodes and permit the transport of both ions and electrical charge.

The difference in chemical potential between reactions occurring on the electrodes drives the flow of electrons in the system. The nature of the reaction that occurs on each electrode depends on which reactant flow it contacts, with the fuel stream undergoing oxidation reactions (with the electrode designated the “anode”) and the oxidizer stream undergoing reduction reactions (with the electrode designated the “cathode”). Reactions occurring on the surfaces of the electrodes are usually enabled and accelerated by a catalyst coating that improves the rate of power conversion on a given surface area.

---

[3] Much of the material in this section is drawn from the more elaborate explanations available in *Principles of Fuel Cells* by Xianguo Li.[10]

The electrodes are separated by a material layer called the electrolyte that is electrically insulating, but conductive to at least one of the species created in the reaction at the anode or cathode. In many low-temperature fuel cells (like Proton-Exchange Membrane, or PEM, fuel cells, see Figure 73) the exchanged species are protons, generated from the decomposition of hydrogen gas ($H_2 \rightarrow 2H^+ + 2e^-$) on the anode. The protons diffuse through the electrolyte to react with oxygen ($2H^+ + \frac{1}{2}O_2 + 2e^- \rightarrow H_2O$) on the cathode side.

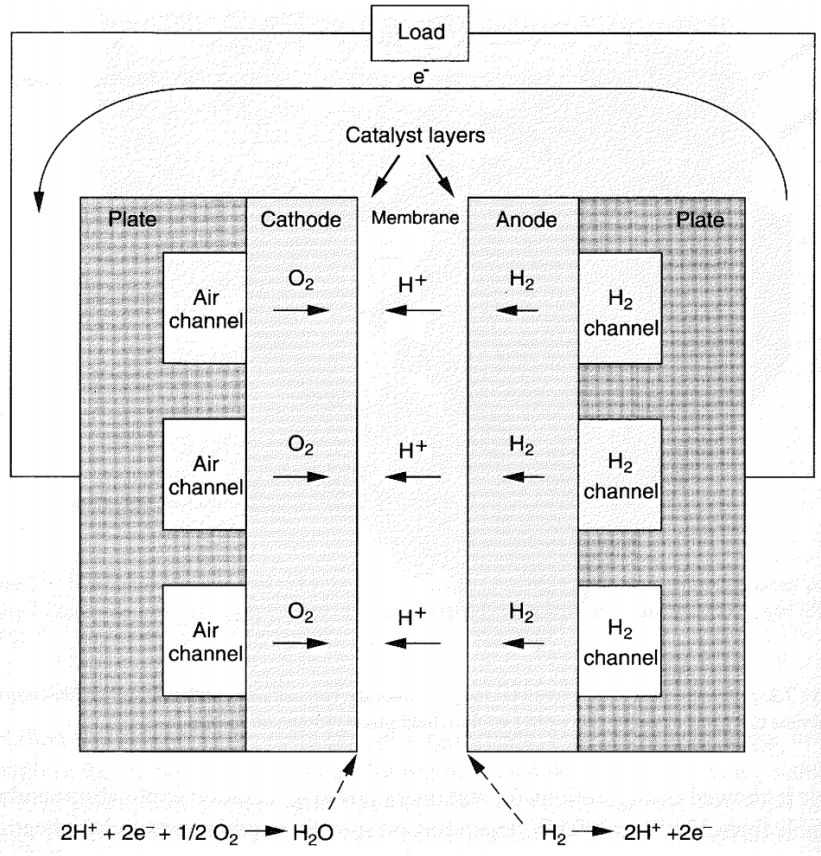

Figure 73: Schematic of PEM fuel cell operation, adapted from [10, p. 304]

In solid oxide fuel cells (SOFCs), the exchanged species are oxygen ions that flow from cathode to anode as illustrated in Figure 74. In this case, the reaction

occurring on the cathode side is the dissociation of oxygen, while on the anode side is the formation of water. The fuel stream in an SOFC is typically a mixture of H_2, CO, CO_2 and H_2O called 'syngas' that is produced by reforming a hydrocarbon fuel, while is typically the oxidant stream.

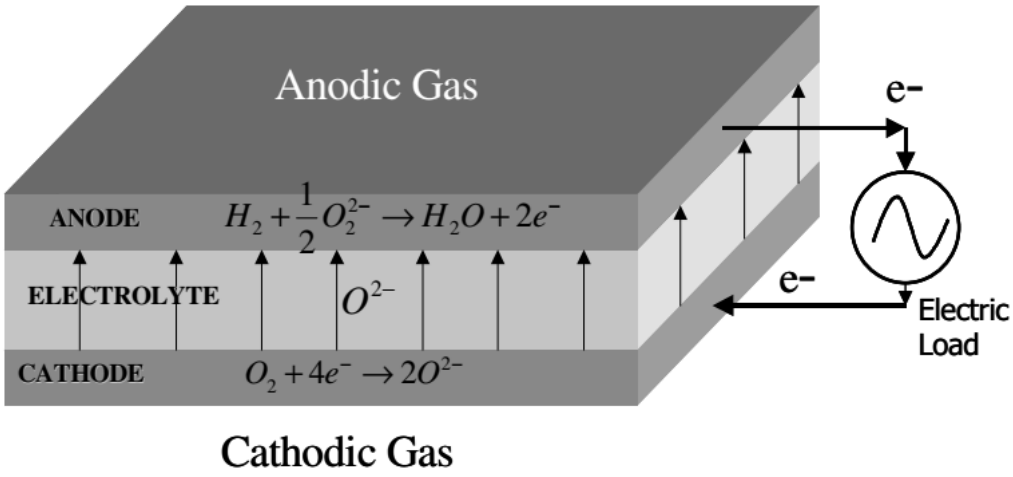

Figure 74: Solid Oxide Fuel Cell Schematic, adapted from [96]

In an SOFC, the distinguishing characteristics are an electrolyte made of an oxide ceramic material. At sufficiently high operating temperatures (between approximately 550-1000°C), the oxygen ions within the oxide material become mobile among vacancies inside the material structure, allowing the oxide to transport oxygen ions across the interior of the material while remaining an insulator to electricity. The main half-reactions occurring at each electrode surface are:

$$H_2 + O^{2-} \rightarrow H_2O + 2e^- \ (Anode)$$
$$\frac{1}{2}O_2 + 2e \rightarrow O^{2-} \ (Cathode)$$

While a similar reaction employing CO is another (though much slower) component, potentially more important is the water-gas shift reaction, which converts water and carbon monoxide in the stream to carbon dioxide and hydrogen gas:

$$CO + H_2O \leftrightarrow CO_2 + H_2$$

From a practical perspective, SOFCs are somewhat more resistant to poisoning than other types of fuel cells (albeit can still be poisoned over time by sulfur concentrations over 0.1ppm) and require no humidification as in PEM fuel cells. Their high operating temperature also allows them to operate in a similar temperature range to heat-engine components which will be important later.

13.2.1 Standard Modeling for Fuel Cells

Fuel cell models are based on the principles of the reversible cell potential, and conservation of mass, momentum, energy, and species. The details of how these processes are represented will be discussed in section 8.4.

The fundamental equation for the performance of a fuel cell is the Nernst equation, which relates the maximum possible cell potential/voltage (E_{Nernst}) to the reversible cell potential (usually measured at some standard condition like 1 atm and 25°C), Faraday's constant (F), the gas constant (R), the number of electrons transferred (n) and the partial pressures of the reactants and products. The Nernst potential in the hydrogen-oxygen system specifically is given by:

$$E_{Nernst} = E_{rev}(T, P) - \frac{RT}{nF}\ln\left(\frac{P_{H_2}P_{O_2}^{1/2}}{P_{H_2O}}\right)$$

For the hydrogen-oxygen system $n = 2$. The Nernst potential is the maximum potential that is thermodynamically achievable, but the potential of a real cell is lower because of various loss processes. These losses are represented using 'overpotentials' (η) so that the expression for the actual cell voltage can be given by:

$$E_{cell} = E_{Nernst} - \eta_{act} - \eta_{ohm} - \eta_{conc}$$

Activation overpotentials (η_{act}) are related to the excess energy needed to cause a reaction to occur spontaneously (the "activation energy") by overcoming any energetically unfavorable conditions in the transition between reactants and products. Ohmic overpotentials (η_{ohm}) are associated with resistive losses throughout the system, both at electrodes and through system wiring. Finally, concentration overpotentials (η_{conc}) are related to the kinetics of the system at the electrodes, such that gradients of products and reactants can be expected to form, affecting the effective concentration at the location where reactions occur.

For SOFCs, the activation and concentration overpotentials are often small due to the high operating temperature and electrode catalysts, which create fast reaction kinetics and rapid mass diffusion. However, the corresponding ohmic losses are significant, generating almost linear losses to voltage with increasing current. Taken together, these losses can be used to generate a polarization curve which is a standard way of representing fuel cell performance.

13.2.2 Performance Characterization: Polarization Curve

The polarization curve is the relationship between the fuel cell's output voltage and output current. A typical polarization curve of a generic fuel cell is shown below from Li [10, p. 94] in Figure 75 below:

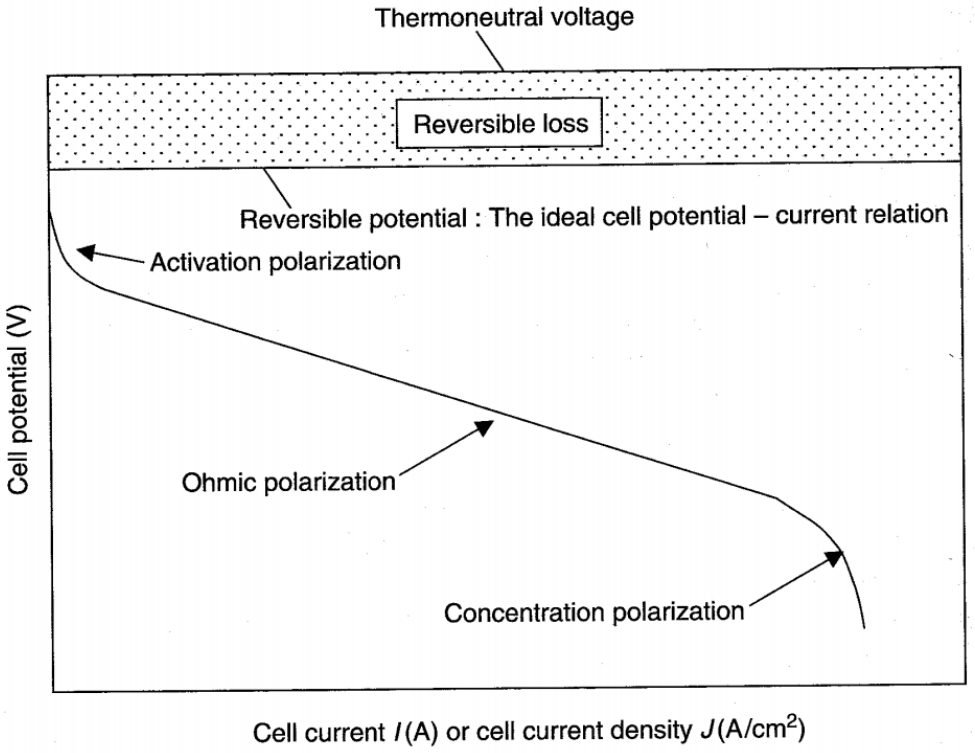

Figure 75: Typical Polarization Curve and Contributing Factors adapted from Li [10, p. 94]

Note that one implication of this polarization curve is that the fewest losses occur at low cell current loads. If a curve representing the power output was overlaid with this plot however, we would see a peak power (and so a peak power density) at some higher level of cell current depending on the scaling of the system. The tradeoff

between efficiency and power density is important for mass-sensitive applications such as aircraft.

13.2.3 Efficiency Paradigm

The limits of efficiency of a fuel cell are fundamentally the same as those of a heat engine than a heat engine cycle, with both based on the second law of thermodynamics (yielding so-called "second law efficiencies"). [10, p. 83] The equation for the maximum efficiency of a reversible process (applying to both ideal fuel cells and ideal heat engines) is the ratio of Gibbs Free Energy (Δg) to Enthalpy (Δh) available. The Gibbs energy is also the negative of the work out (w) in the reversible case:

$$\eta_{rev} = \frac{\Delta g(T,P)}{\Delta h(T,P)} = \frac{-w}{\Delta h}$$

In the special case of a heat engine, the system operates between at least two thermal energy reservoirs (TERs), one at a high (T_H) and one at a low (T_L) temperature state. Heat energy is drawn from the hot TER (q_L) and absorbed by the cool TER (q_L). For the ideal reversible case, according to the first law of thermodynamics the difference in the two heat quantities represents the amount of work (w) generated by the heat engine:

$$w = q_H - q_L$$

The second law of thermodynamics for a reversible system (the case for the maximum efficiency) implies that $q = T\Delta s$ at both TERs, such that:

$$\frac{q_L}{T_L} = \frac{q_H}{T_H} = \Delta s = 0$$

If we take the heat engine efficiency to be defined as the ratio of the work out to the amount of energy that supplied as a cost (here q_H) we can substitute from above to show that:

$$q_H = q_L \frac{T_H}{T_L} \rightarrow \eta_{rev} = \frac{w}{q_H} \rightarrow \eta_{rev} = \frac{q_H - q_L}{q_H} \rightarrow \eta_{rev} = 1 - \frac{T_L}{T_H}$$

This is the traditional Carnot efficiency relationship. Conceptually, we can compare the Carnot efficiency and the fuel cell efficiency relationships by considering a thermodynamic system appropriate for a fuel cell. Take the operating temperature of the fuel cell to be T_L, as the reactants enter the system at roughly this temperature. A high temperature TER exists where the combustion reaction occurs, but products leave the TER at the original "low" operating temperature as most fuel cells are designed to maintain as consistent a temperature and pressure as possible. In a fuel cell, the T_H value is never physically reached. For a reversible case, the outcome [10, p. 86] is the fuel cell reversible efficiency expression, with T_L as the function input to the enthalpy and Gibbs energy.

As such, a way to consider a reversible fuel cell is as an ideal Carnot heat engine that always operates using a stoichiometric mixture of reactants and products, while T_L is set as the operating temperature of the fuel cell rather than ambient conditions. An equivalent heat engine operating at ambient would reach the adiabatic flame temperature (approximately 3200°C for hydrogen-oxygen), yielding a substantially higher efficiency than what would normally be considered for a heat engine. However,

it would not face the usual material difficulties in achieving that temperature (as the actual operating temperature is ambient), nor require the fuel and oxidant flows to be stoichiometric (though the partial pressures of the reactants and products are relevant). Additionally, roughly the same ΔT would be generated regardless of T_L, with the resulting "Carnot" efficiency dropping off as T_L increases:

$$\eta_{rev} = 1 - \frac{T_L}{T_L + \Delta T} \xrightarrow[T_L \to \infty]{} \eta_{rev} = 0$$

Figure 76 illustrates this behavior for a hydrogen-oxygen system with a Carnot engine and an SOFC. Note that the temperature given is the highest "operating" temperature, which in the conception outlined here is actually T_L for the fuel cell, and T_H for a heat engine.

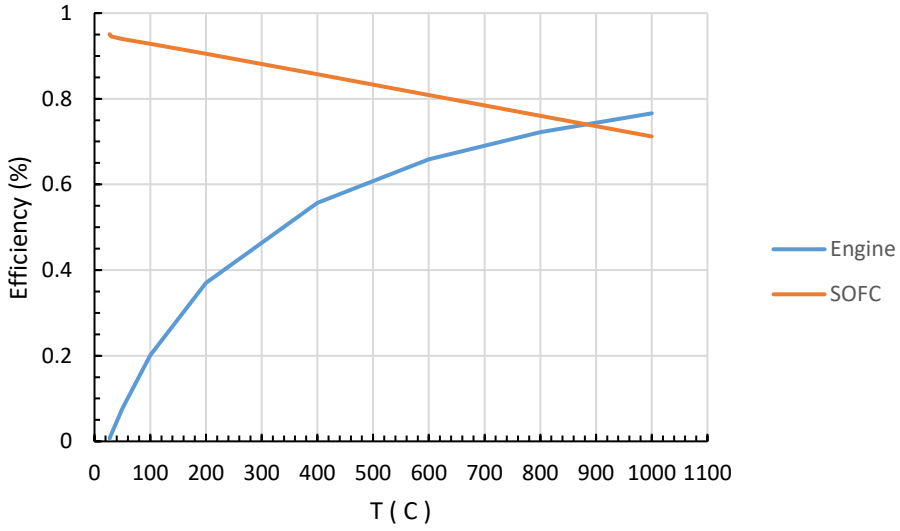

Figure 76: Comparison of reversible efficiency of Carnot engine and fuel cell at varying operating temperatures

13.2.4 Balance of Plant Concerns

"Balance of Plant" refers to the additional machinery necessary to run the overall energy conversion system beyond the fuel cell itself. This includes pumps, blowers, controlling electronics, valves, and fuel processors/reformers [1]. These additional components lower the specific power of the system by adding additional "dead weight" that isn't related to the power density of the fuel cell itself.

13.2.5 Prior Fuel Cell Applications in Aerospace

In general, fuel cells are not widely employed in aerospace applications, with certain exceptions in early spacecraft and occasional niche or experimental uses [97, Ch. 17.6]. Their relatively low technological readiness and low power density relative to the gas turbine are disadvantageous in the mass-sensitive aerospace environment—for context, the specific power of a standalone fuel cell tends to be on the order of hundreds of Watts per kilogram versus the specific power of modern heat engines that reach on order kilowatts per kilogram [98].

13.3 SOFC Standard Operating Procedures

1. SYSTEM COMPONENTS AND REQUIREMENTS
    a. Ultra/AMI D300 SOFC APU
    b. Charged BB-2590/U battery
    c. Operational hood or other strong ventilation system
    d. Carbon monoxide/flammable-gas warning sensor
    e. Industrial-grade propane supply ()
    f. Raspberry Pi with monitor/keyboard/mouse
    g. System Load (as of time of writing, a resistor load bank)
    h. Electrical multimeter
2. STARTUP PROCEDURE
    a. Charge BB-2590/U battery some time before experiment
    b. Turn on (1) hood, (2) raspberry pi, (3) CO/flammable-gas sensor
    c. Prepare system load (here, resistor load bank)
        i. Attach ground wire to outlet ground
        ii. Check that system load switch is open
        iii. Connect all resistors and check for short between resistors and ground plate
        iv. Turn on load cooling fans as available
    d. Open Propane tank main valve and set propane regulator to 15-20 psi of output feed pressure
    e. Press and hold main power button on APU
    f. On Raspberry Pi, start SerialConnect2.py (or updated equivalent) software and answer prompts to begin data collection
        i. can start any time, though it's suggested to wait 20-30 minutes since startup data can be largely uninteresting and is well covered)
        ii. Alternately, allow system to run and recharge battery until "Hybrid Battery Current" approaches -0.01 A, which will indicate a charged battery and largely stable load conditions (~1 hour)
3. OPERATING PROCEDURE (NOTIONAL)
    a. If not done before data collection started, allow system to charge battery and reach equilibrium (Step 2(f)(ii) above)
    b. Set first desired resistive load value on resistor bank by connecting the appropriate resistors with alligator clip wires. Note that resistance values less than ~4 have resulted in overload conditions for the APU, which will attempt to maintain the target voltage (~32V) at the expense of current output

c. Flip system load switch to close the output circuit
d. Allow system to equilibrate for at least 20 minutes – longer is better whenever possible
e. Flip system load switch to open the circuit, and reconfigure resistor bank to next intended resistance value
f. Repeat steps 3c-3e until desired range of values have been collected. Note that the shutdown procedure can take between 20-30 minutes to complete, so allow for enough time in the experiment schedule

4. SHUTDOWN PROCEDURE
    a. After last data collected, flip the system load switch to open, and hold the power button on the APU until it begins the shutdown procedure. Proceed with other steps but stay with system until completion
    b. Click the "Quit" button or equivalent on the Raspberry Pi script and follow the instructions
    c. Turn off (1) Raspberry Pi, (2) laboratory hood, and (3) CO/Flammable gas sensor (1 and 3 can remain on)
    d. Close regulator valve to fuel supply (screwing "up") and close main outlet valve

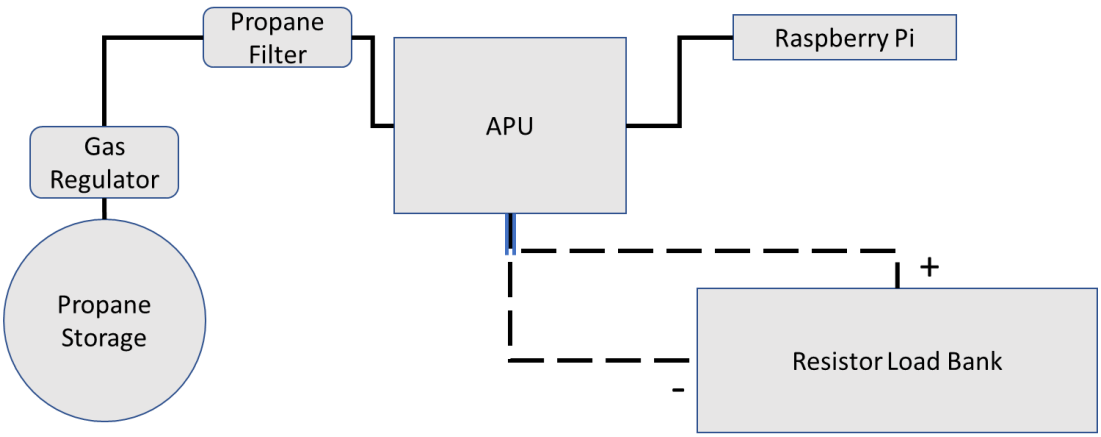

13.4 SOFC APU Experiment Data

The following Table 8 contains information regarding the characteristics of each experiment. The hand-collected experiments from November 11, 2017 are included with their limited information. In addition, plots showing the most relevant raw data for each run are provided.

Table 8: SOFC APU Summary of Characterization Experiments

Run	Experiment	Effective Load (Watts)	Start Time (Min)	End Time (Min)	Duration (Min)	Start Voltage (Volts)	End Voltage (Volts)	Start Current (Amps)	End Current (Amps)	Battery Charged Time (Min)	Notes
1	1	140.9	23.1	40.6	17.5	NaN	32.4	NaN	4.3	114.8	Bulk Battery Charging
1	2	74.9	40.6	93.1	52.5	NaN	36.3	NaN	2.1	114.8	Battery Charging
2	1	68.4	44.5	68.8	24.3	NaN	36.5	NaN	1.9	118.7	Battery Charging
2	2	66.1	68.8	100.8	32.0	NaN	36.8	NaN	1.8	118.7	Battery Charging
2	3	72.3	101.9	117.5	15.5	NaN	36.3	NaN	2.0	118.7	
2	4	86.7	118.2	137.7	19.4	NaN	35.5	NaN	2.4	118.7	
2	5	115.8	141.2	157.5	16.4	33.3	33.4	3.6	3.5	118.7	
2	6	172.2	161.8	167.3	5.6	29.3	29.5	5.9	5.8	118.7	
3	1	171.1	85.4	97.9	12.6	NaN	24.0	NaN	7.1	133.2	Battery Charging
3	2	149.5	100.8	117.8	17.0	NaN	27.0	NaN	5.5	133.2	Battery Charging
3	3	134.4	123.6	138.1	14.5	NaN	28.3	NaN	4.7	133.2	Battery Charging
3	4	124.8	141.5	156.9	15.4	28.9	29.1	4.4	4.3	133.2	
3	5	118.1	159.0	177.4	18.5	29.6	29.6	4.0	4.0	133.2	
3	6	113.3	180.3	197.1	16.8	29.9	30.0	3.8	3.8	133.2	
3	7	108.2	199.5	217.8	18.3	30.4	30.5	3.6	3.6	133.2	
3	8	104.2	219.0	238.4	19.5	31.1	31.1	3.3	3.4	133.2	
3	9	47.9	240.1	251.6	11.5	36.1	35.9	1.3	1.3	133.2	
4	1	53.0	30.0	113.6	83.6	NaN	32.6	NaN	1.6	100.0	Battery Charging
4	2	68.5	113.6	175.2	61.6	31.4	31.4	2.3	2.2	100.0	
4	3	83.4	175.4	201.5	26.1	30.3	30.3	2.8	2.7	100.0	

5	1	49.4	103.0	160.8	57.8	32.4	32.6	1.6	1.5	18.9	
5	2	111.6	170.0	195.2	25.2	28.1	28.2	4.0	4.0	18.9	
5	3	154.8	199.9	227.9	28.0	NaN	24.3	NaN	6.4	18.9	Load Disruption
6	1	52.5	19.5	29.7	10.2	NaN	32.4	NaN	1.6	22.0	Battery Charging
6	2	101.6	31.9	56.1	24.2	28.6	28.8	3.7	3.5	22.0	
6	3	143.6	64.7	88.4	23.7	25.2	25.3	5.8	5.7	22.0	
Hand-record	1	55.1	NaN	NaN	NaN	NaN	32.4	NaN	1.7	NaN	Recording Error
Hand-record	2	68.9	NaN	NaN	NaN	NaN	31.3	NaN	2.2	NaN	Recording Error
Hand-record	3	83.6	NaN	NaN	NaN	NaN	30.4	NaN	2.8	NaN	Recording Error
Hand-record	4	95.0	NaN	NaN	NaN	NaN	29.7	NaN	3.2	NaN	Recording Error
Hand-record	5	102.2	NaN	NaN	NaN	NaN	29.2	NaN	3.5	NaN	Recording Error
Hand-record	6	106.6	NaN	NaN	NaN	NaN	28.8	NaN	3.7	NaN	Recording Error
Hand-record	7	111.5	NaN	NaN	NaN	NaN	28.6	NaN	3.9	NaN	Recording Error
Hand-record	8	118.0	NaN	NaN	NaN	NaN	28.1	NaN	4.2	NaN	Recording Error
Hand-record	9	120.4	NaN	NaN	NaN	NaN	28.0	NaN	4.3	NaN	Recording Error
Hand-record	10	127.9	NaN	NaN	NaN	NaN	27.5	NaN	4.7	NaN	Recording Error
Hand-record	11	136.2	NaN	NaN	NaN	NaN	26.7	NaN	5.1	NaN	Recording Error

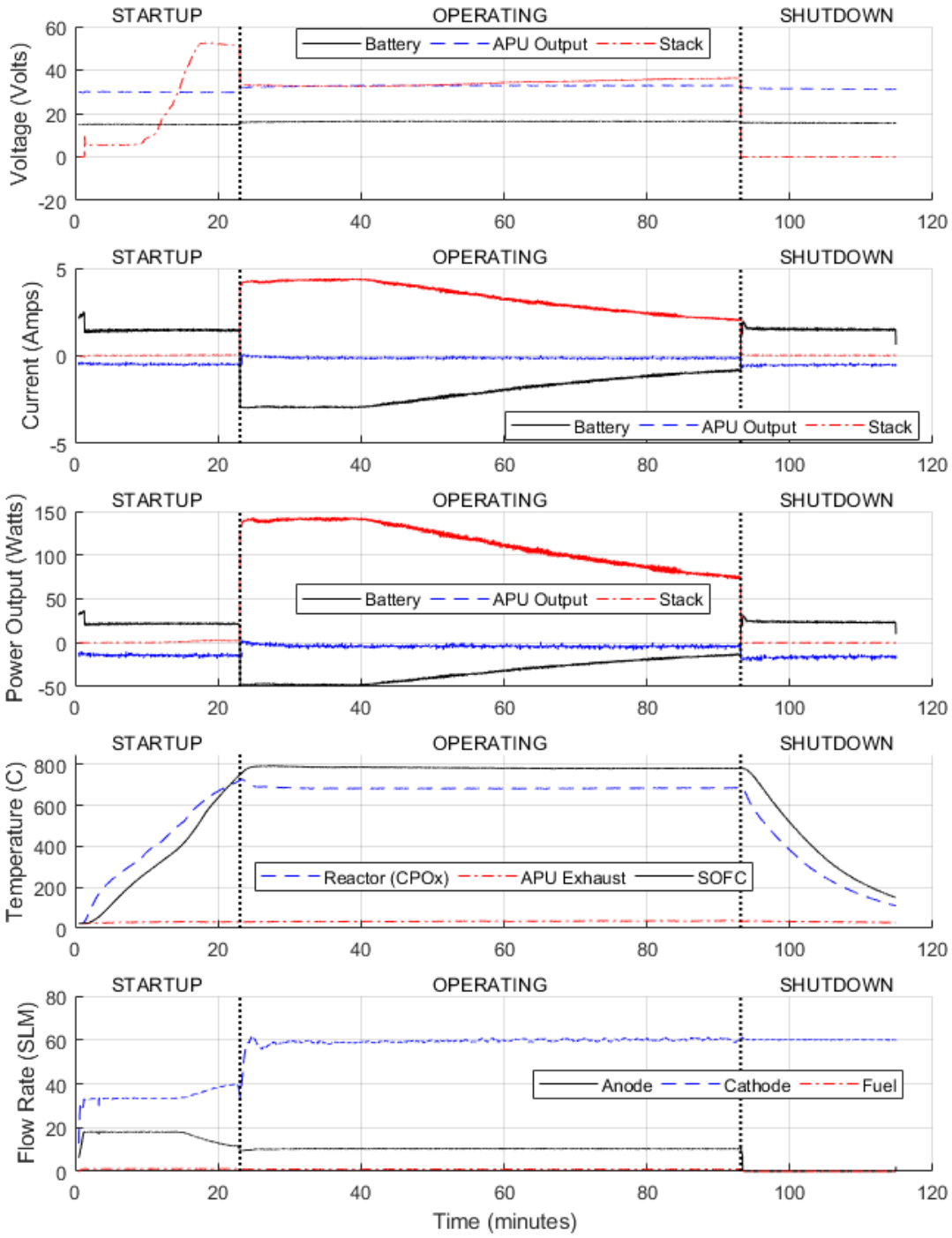

Figure 77: APU Data Output from March 16, 2016

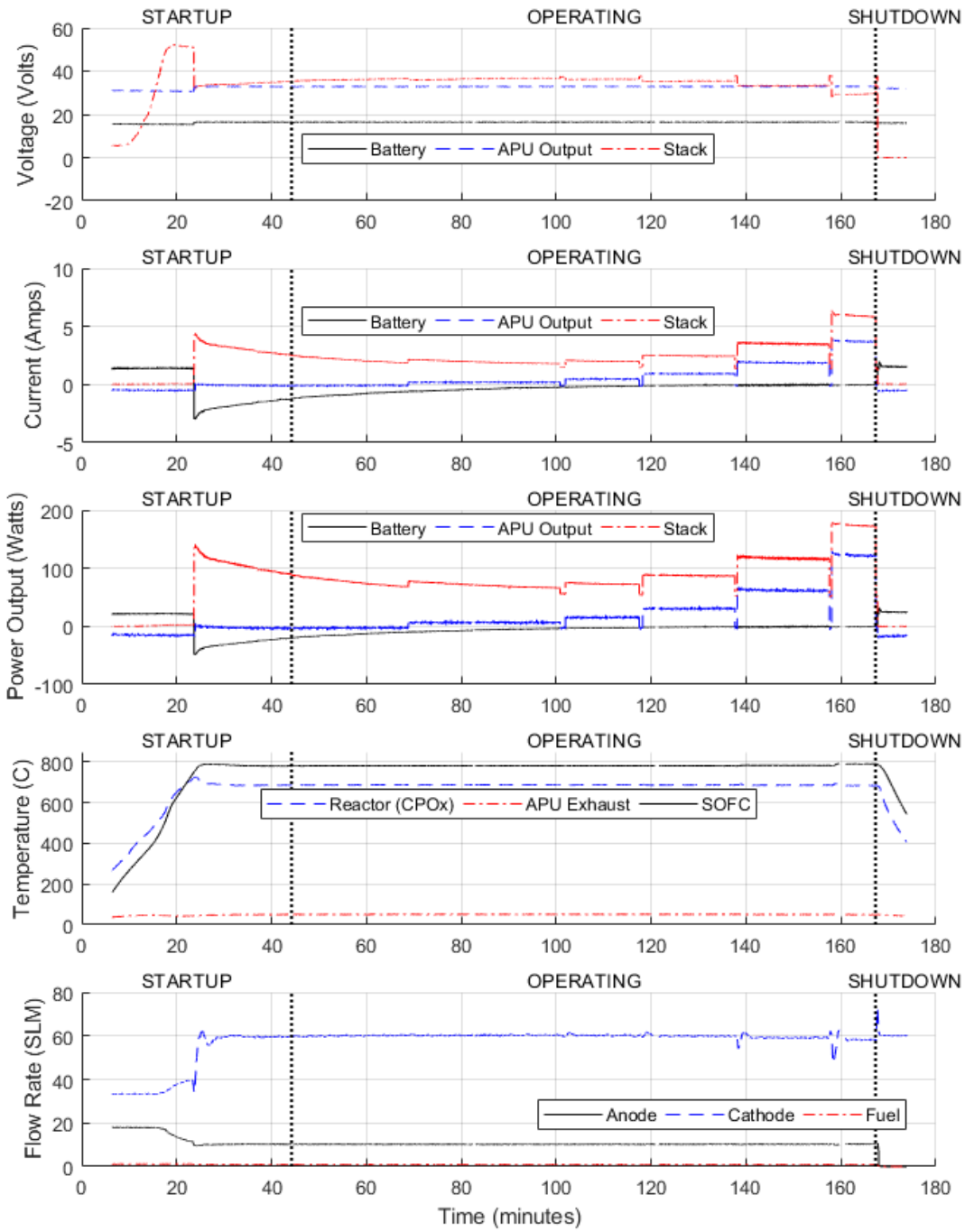

Figure 78: APU Data Output from November 3, 2017

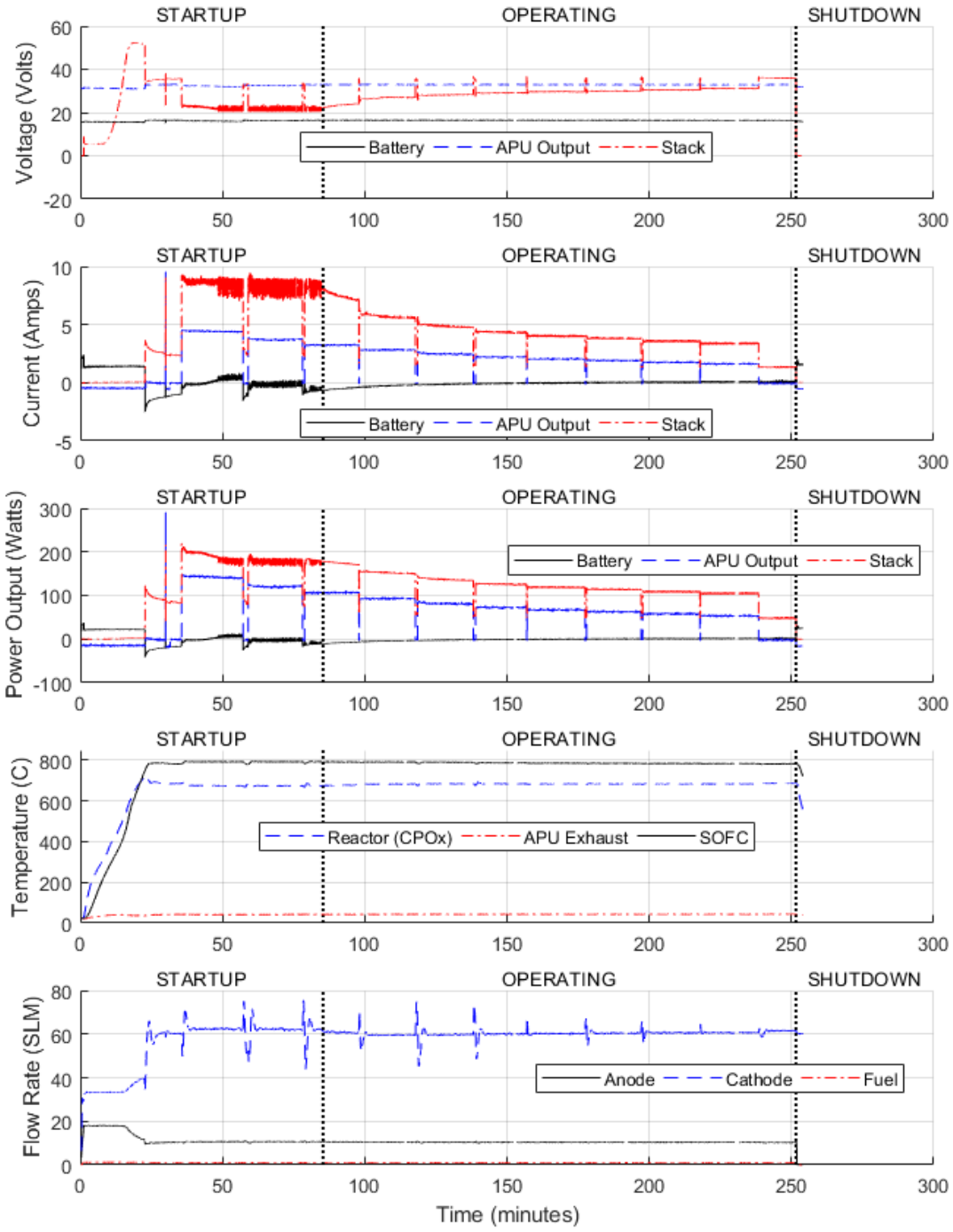

Figure 79: APU Data Output from November 7, 2017

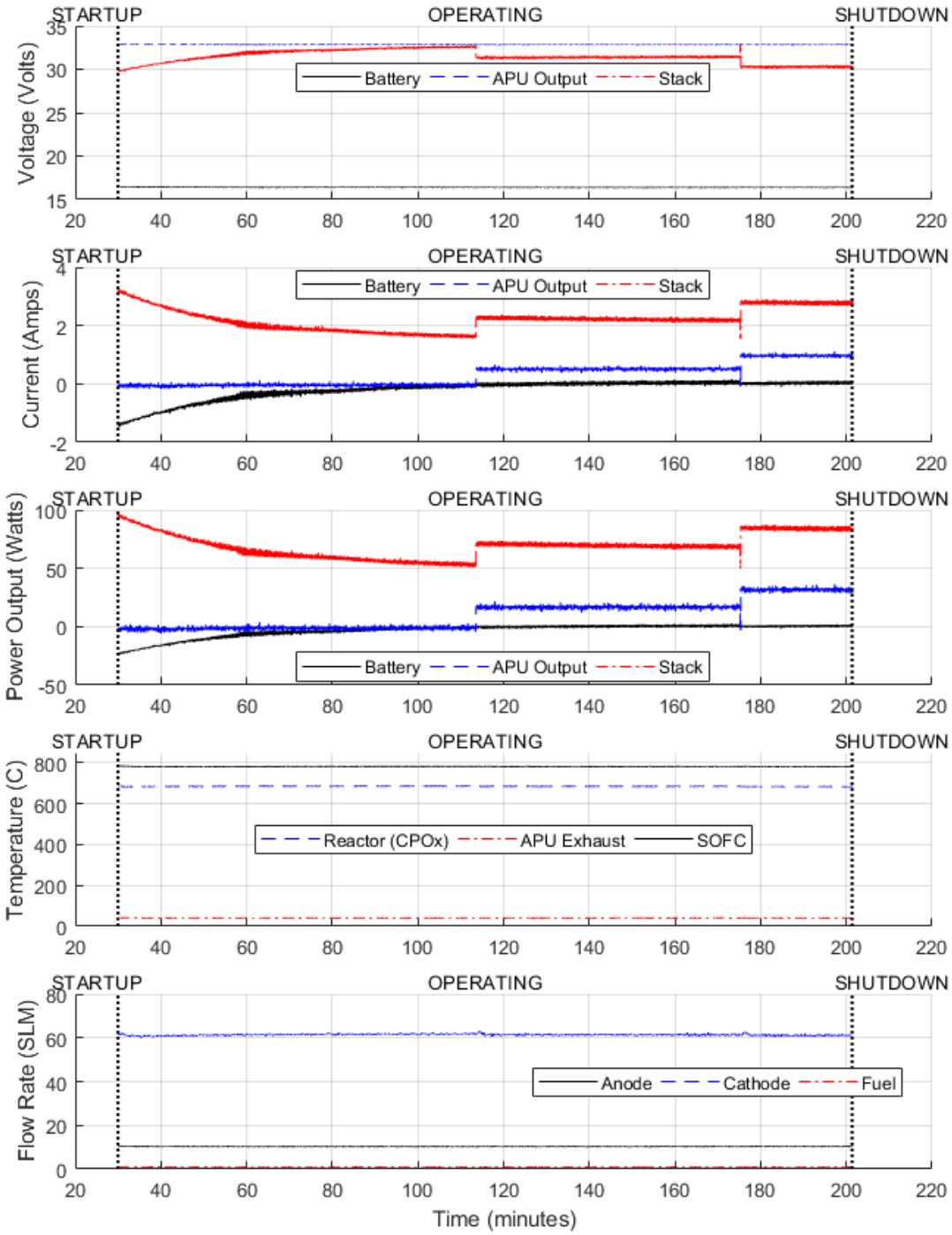

Figure 80: APU Data Output from January 3, 2018

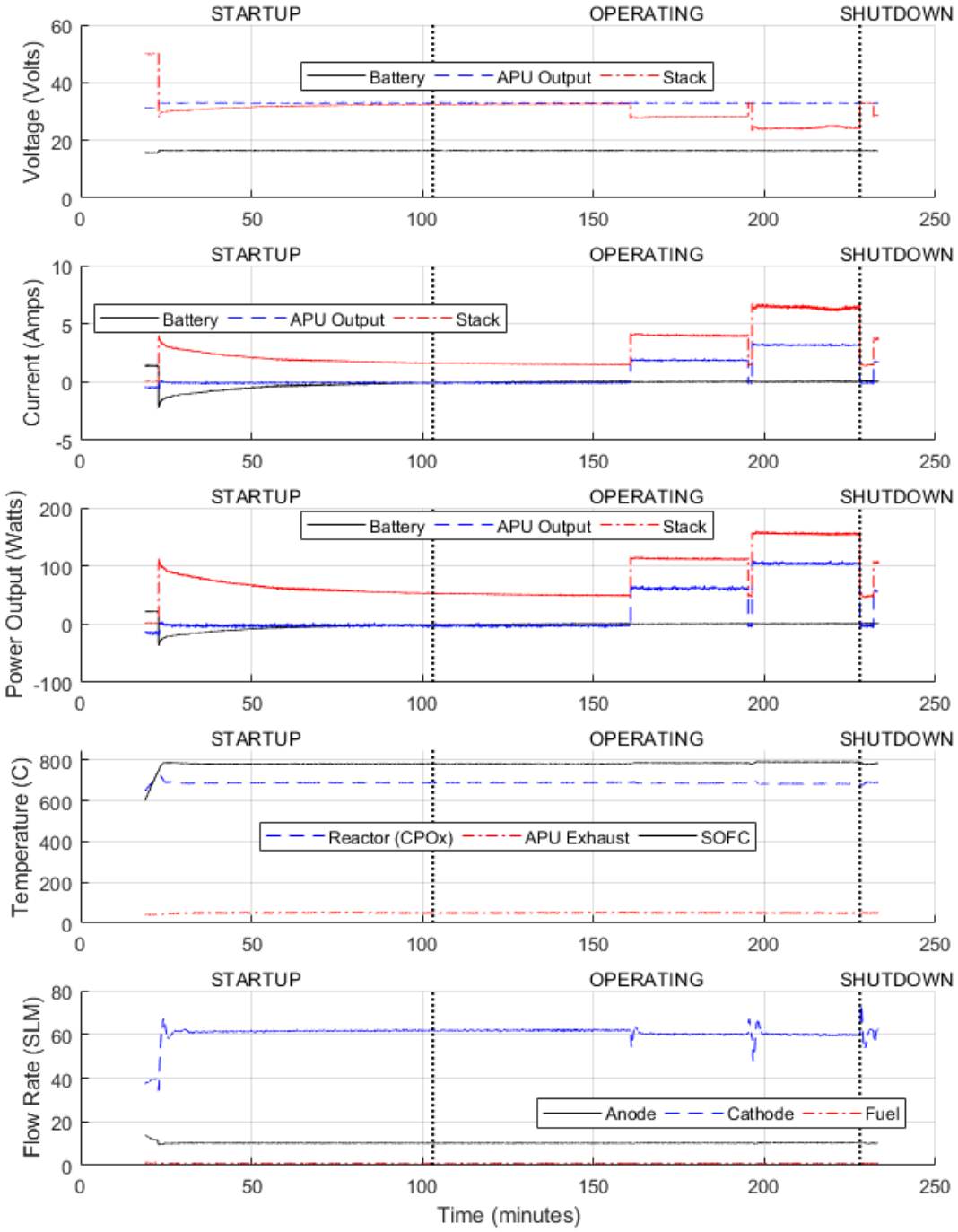

Figure 81: APU Data Output from April 24, 2018 (first data collection)

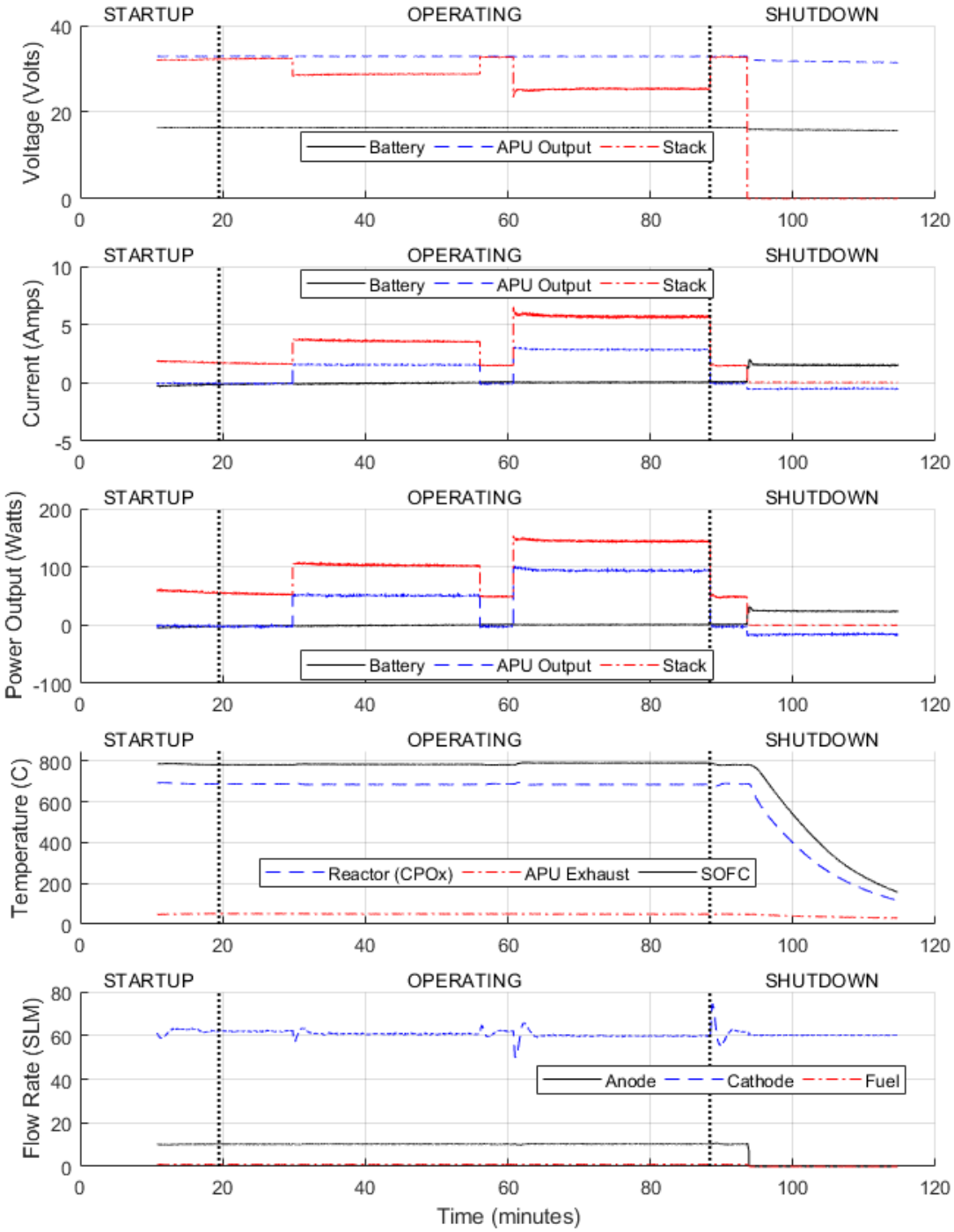

Figure 82: APU Data Output from April 24, 2018 (second data collection)

14 Bibliography

[1] D. F. Waters, “Modeling of Gas Turbine - Solid Oxide Fuel Cell Systems For Combined Propulsion and Power on Aircraft,” University of Maryland, 2015.

[2] K. Rajashekara, “More electric aircraft trends [Technology Leaders],” *IEEE Electrif. Mag.*, vol. 2, no. 4, 2014.

[3] National Aeronautics and Space Administration, “NEW AVIATION HORIZONS INITIATIVE and Complementary Investments,” 2017.

[4] L. M. Pratt, S. Vannoy, and C. P. Cadou, “Development of an Engine-Integrated Fuel Cell Concept Demonstrator: Initial System Sizing,” *52nd AIAA/SAE/ASEE Jt. Propuls. Conf.*, pp. 1–14, 2016.

[5] P. Jackson, K. Munson, and L. Peacock, “IHS Jane’s All the World’s Aircraft: Development & Production.” IHS Global, Inc., Alexandria, VA, 2014.

[6] M. Daly and M. Streetly, “IHS Jane’s All the World’s Aircraft: Unmanned,” Alexandria, VA.

[7] S. W. Ashcraft, A. S. Padron, K. a Pascioni, G. W. Stout Jr., and D. L. Huff, “Review of Propulsion Technologies for N+3 Subsonic Vehicle Concepts,” no. October, p. 38, 2011.

[8] R. Royce, *Jet Engine*, 5th ed. John Wiley & Sons, 2015.

[9] L. R. Radovic and H. H. Schobert, “Chapter 4: Efficiency of Energy Conversion,” in *Energy and Fuels in Society: Analysis of Bills and Media Reports*, 2nd ed., no. 1, New York: McGraw-Hill, 1997, pp. 53–76.

[10] X. Li, *Principles of Fuel Cells*, 1st ed. New York: Taylor & Francis, 2006.

[11] A. J. Head, “Performance Trends of High-Bypass Civil Turbofans,” 2015.

[12] K. Flittie and B. Curtin, “Pathfinder solar-powered aircraft flight performance,” *23rd Atmos. Flight Mech. Conf.*, 1998.

[13] B. Scrosati and J. Garche, “Lithium batteries: Status, prospects and future,” *J. Power Sources*, vol. 195, no. 9, pp. 2419–2430, 2010.

[14] W. Ng and A. Datta, “Development of Propulsion System Models for Electric-VTOL Aircraft,” in *2018 AIAA Aerospace Sciences Meeting*, 2018.

[15] M. Yassine and D. Fabris, “Performance of Commercially Available Supercapacitors,” *Energies*, vol. 10, no. 9, p. 1340, Sep. 2017.

[16] P. G. Hill and C. R. Peterson, *Mechanics and Thermodynamics of Propulsion*, 2nd ed. Reading, MA: Addison-Wesley, 1992.

[17] D. F. Waters and C. P. Cadou, “Engine-integrated solid oxide fuel cells for

efficient electrical power generation on aircraft," *J. Power Sources*, vol. 284, pp. 588–605, Jun. 2015.

[18] M. Henke *et al.*, "Effect of pressure variation on power density and efficiency of solid oxide fuel cells," *Electrochim. Acta*, vol. 66, pp. 158–163, Apr. 2012.

[19] J. H. Yi and T. S. Kim, "Effects of fuel utilization on performance of SOFC/gas turbine combined power generation systems," *J. Mech. Sci. Technol.*, vol. 31, no. 6, pp. 3091–3100, Jun. 2017.

[20] F. Calise, M. Dentice d' Accadia, L. Vanoli, and M. R. von Spakovsky, "Single-level optimization of a hybrid SOFC–GT power plant," *J. Power Sources*, vol. 159, no. 2, pp. 1169–1185, Sep. 2006.

[21] Y. HASELI, I. DINCER, and G. NATERER, "Thermodynamic modeling of a gas turbine cycle combined with a solid oxide fuel cell," *Int. J. Hydrogen Energy*, vol. 33, no. 20, pp. 5811–5822, Oct. 2008.

[22] A. Abbasi and Z. Jiang, "Multidisciplinary modeling and simulation of a fuel cell/gas turbine hybrid power system," in *2009 IEEE Power & Energy Society General Meeting*, 2009, pp. 1–7.

[23] S. H. Chan, H. K. Ho, and Y. Tian, "Modelling of simple hybrid solid oxide fuel cell and gas turbine power plant," *J. Power Sources*, vol. 109, no. 1, pp. 111–120, Jun. 2002.

[24] J. Palsson, A. Selimovic, and L. Sjunnesson, "Combined solid oxide fuel cell and gas turbine systems for efficient power and heat generation," *J. Power Sources*, vol. 86, no. 1–2, pp. 442–448, Mar. 2000.

[25] P. Costamagna, L. Magistri, and A. F. Massardo, "Design and part-load performance of a hybrid system based on a solid oxide fuel cell reactor and a micro gas turbine," *J. Power Sources*, vol. 96, no. 2, pp. 352–368, Jun. 2001.

[26] T. LIM *et al.*, "Operating characteristics of a 5kW class anode-supported planar SOFC stack for a fuel cell/gas turbine hybrid system," *Int. J. Hydrogen Energy*, Jan. 2008.

[27] T. Suther, A. S. Fung, M. Koksal, and F. Zabihian, "Effects of operating and design parameters on the performance of a solid oxide fuel cell-gas turbine system," *Int. J. Energy Res.*, vol. 35, no. 7, pp. 616–632, Jun. 2011.

[28] Y. Zhao, J. Sadhukhan, A. Lanzini, N. Brandon, and N. Shah, "Optimal integration strategies for a syngas fuelled SOFC and gas turbine hybrid," *J. Power Sources*, vol. 196, no. 22, pp. 9516–9527, Nov. 2011.

[29] L. Leto, C. Dispenza, A. Moreno, and A. Calabrò, "Simulation model of a molten carbonate fuel cell–microturbine hybrid system," *Appl. Therm. Eng.*, vol. 31, no. 6–7, pp. 1263–1271, May 2011.

[30] A. Buonomano, F. Calise, M. D. D'Accadia, A. Palombo, and M. Vicidomini, "Hybrid solid oxide fuel cells-gas turbine systems for combined heat and power: A review," *Appl. Energy*, vol. 156, pp. 32–85, 2015.

[31] M. A. Azizi and J. Brouwer, "Progress in solid oxide fuel cell-gas turbine hybrid power systems: System design and analysis, transient operation, controls and optimization," *Appl. Energy*, vol. 215, no. August 2017, pp. 237–289, Apr. 2018.

[32] J. H. Yi, J. H. Choi, and T. S. Kim, "Comparative evaluation of viable options for combining a gas turbine and a solid oxide fuel cell for high performance," *Appl. Therm. Eng.*, vol. 100, pp. 840–848, 2016.

[33] M. Rokni, "Performance Comparison on Repowering of a Steam Power Plant with Gas Turbines and Solid Oxide Fuel Cells," *Energies*, vol. 9, no. 6, p. 399, May 2016.

[34] Z. Hajabdollahi and P.-F. Fu, "Multi-objective based configuration optimization of SOFC-GT cogeneration plant," *Appl. Therm. Eng.*, vol. 112, pp. 549–559, Feb. 2017.

[35] T. Choudhary and Sanjay, "Thermodynamic assessment of advanced SOFC-blade cooled gas turbine hybrid cycle," *Int. J. Hydrogen Energy*, vol. 42, no. 15, pp. 10248–10263, Apr. 2017.

[36] P. Saisirirat, "The Solid Oxide Fuel Cell (SOFC) and Gas Turbine (GT) Hybrid System Numerical Model," *Energy Procedia*, vol. 79, pp. 845–850, Nov. 2015.

[37] J. H. Yi, J. H. Choi, and T. S. Kim, "A Comparative Study on the Options in Combining Solid Oxide Fuel Cell with Gas Turbine," in *Proceedings of the ASME Turbo Expo 2015: Turbine Technical Conference and Exposition*, 2015.

[38] J. Pirkandi, M. Mahmoodi, and M. Ommian, "An optimal configuration for a solid oxide fuel cell-gas turbine (SOFC-GT) hybrid system based on thermo-economic modelling," *J. Clean. Prod.*, vol. 144, pp. 375–386, Feb. 2017.

[39] S. F. Sghaier, T. Khir, and A. Ben Brahim, "Energetic and exergetic parametric study of a SOFC-GT hybrid power plant," *Int. J. Hydrogen Energy*, vol. 43, no. 6, pp. 3542–3554, Feb. 2018.

[40] Z. Dang, H. Zhao, and G. Xi, "Conceptual Design and Performance Analysis of SOFC/Micro Gas Turbine Hybrid Distributed Energy System," *J. Fuel Cell Sci. Technol.*, vol. 12, no. 3, p. 031003, Jun. 2015.

[41] E. A. Valencia, V. Hidalgo, L. Panagiotis, D. Nalianda, R. Singh, and C. Liu, "Design Point Analysis of an Hybrid Fuel Cell Gas Turbine Cycle for Advanced Distributed Propulsion Systems," in *51st AIAA/SAE/ASEE Joint Propulsion Conference*, 2015.

[42] V. A. Chakravarthula, R. A. Roberts, and M. Wolff, "Dynamic Model of Solid

Oxide Fuel Cell Integrated with Fan and Exhaust Nozzle," in *14th International Energy Conversion Engineering Conference*, 2016, pp. 1–14.

[43] K. Okai, T. Himeno, T. Watanabe, H. Nomura, and T. Tagashira, "Investigation of FC/GT Hybrid Core in Electrical Propulsion for Fan Aircraft," in *51st AIAA/SAE/ASEE Joint Propulsion Conference*, 2015, pp. 1–2.

[44] K. Okai, T. Himeno, T. Watanabe, H. Nomura, T. Tagashira, and A. Nishizawa, "Potential of Aircraft Electric Propulsion with SOFC/GT Hybrid Core," in *52nd AIAA/SAE/ASEE Joint Propulsion Conference*, 2016, pp. 1–14.

[45] K. Okai, H. Nomura, T. Tagashira, and A. Nishizawa, "Effects of Fuel Type on Aircraft Electric Propulsion with SOFC/GT Hybrid Core," in *53rd AIAA/SAE/ASEE Joint Propulsion Conference*, 2017, no. July, pp. 1–13.

[46] S. E. Veyo, L. A. Shockling, J. T. Dederer, J. E. Gillett, and W. L. Lundberg, "Tubular Solid Oxide Fuel Cell/Gas Turbine Hybrid Cycle Power Systems: Status," *J. Eng. Gas Turbines Power*, vol. 124, no. 4, p. 845, 2002.

[47] R. J. Braun, M. Gummalla, and J. Yamanis, "System Architectures for Solid Oxide Fuel Cell-Based Auxiliary Power Units in Future Commercial Aircraft Applications," *J. Fuel Cell Sci. Technol.*, vol. 6, no. 3, p. 031015, 2009.

[48] S. Eelman, I. del Pozo y de Poza, and T. Krieg, "Fuel Cell APU's in Commercial Aircraft – an Assessment of SOFC and PEMFC Concepts," *24th Int. Congr. Aeronaut. Sci. (IC*, pp. 1–10, 2004.

[49] J. E. Freeh, J. W. Pratt, and J. Brouwer, "Development of a Solid-Oxide Fuel Cell/Gas Turbine Hybrid System Model for Aerospace Applications," in *Volume 7: Turbo Expo 2004*, 2004, no. May 2004, pp. 371–379.

[50] J. E. Freeh, C. J. Steffen, and L. M. Larosiliere, "Off-Design Performance Analysis of a Solid-Oxide Fuel Cell/Gas Turbine Hybrid for Auxiliary Aerospace Power," in *3rd International Conference on Fuel Cell Science, Engineering and Technology*, 2005, vol. 2005, no. December 2005, pp. 265–272.

[51] K. Rajashekara, J. Grieve, and D. Daggett, "Solid Oxide Fuel Cell/Gas Turbine Hybrid APU System for Aerospace Applications," in *Conference Record of the 2006 IEEE Industry Applications Conference Forty-First IAS Annual Meeting*, 2006, vol. 5, pp. 2185–2192.

[52] K. Rajashekara, J. Grieve, and David Dagget, "Hybrid Fuel Cell Power in Aircraft," *IEEE Industry Applications Magazine*, vol. 14, pp. 54–60, 2008.

[53] C. J. Steffen, J. E. Freeh, and L. M. Larosiliere, "Solid Oxide Fuel Cell/Gas Turbine Hybrid Cycle Technology for Auxiliary Aerospace Power," in *Volume 5: Turbo Expo 2005*, 2005, no. May 2005, pp. 253–260.

[54] A. Himansu, J. E. Freeh, C. J. Steffen, R. T. Tornabene, and X.-Y. J. Wang, "Hybrid Solid Oxide Fuel Cell/Gas Turbine System for High Altitude Long Endurance Aerospace Missions," in *ASME 2006 Fourth International Conference on Fuel Cell Science, Engineering and Technology, Parts A and B*, 2006, vol. 2006, no. May 2006, pp. 573–583.

[55] P. AGUIAR, D. BRETT, and N. BRANDON, "Solid oxide fuel cell/gas turbine hybrid system analysis for high-altitude long-endurance unmanned aerial vehicles," *Int. J. Hydrogen Energy*, vol. 33, no. 23, pp. 7214–7223, Dec. 2008.

[56] M. K. Bradley and C. K. Droney, "Subsonic Ultra Green Aircraft Research : Phase I Final Report," 2011.

[57] M. K. Bradley and C. K. Droney, "Subsonic Ultra Green Aircraft Research Phase II: N+4 Advanced Concept Development," 2012.

[58] S. M. Jones, "An introduction to thermodynamic performance analysis of aircraft gas turbine engine cycles using the numerical propulsion system simulation code," no. March, 2007.

[59] Mason E. A. and A. P. Malinauskas, *Gas transport in porous media : the dusty-gas model / E.A. Mason and A.P. Malinauskas*. Elsevier Scientific Pub. Co Amsterdam ; New York, 1983.

[60] D. F. Waters, S. Vannoy, and C. P. Cadou, "Influence of Flow Path Configuration on the Performance of Hybrid Turbine - Solid Oxide Fuel Cell Systems for Aircraft Propulsion and Power," in *51st AIAA/SAE/ASEE Joint Propulsion Conference*, 2015.

[61] S. Vannoy and C. P. Cadou, "Development and Validation of an NPSS Model of a Small Turbojet Engine," in *52nd AIAA/SAE/ASEE Joint Propulsion Conference*, 2016.

[62] S. Vannoy, "Development and Validation of an NPSS Model of a Small Turbojet Engine," University of Maryland College Park, 2017.

[63] B. Campbell, S. Crase, and B. Sims, "Review of Fuel Cell Technologies for Military Land Vehicles," Fisherman's Bend, 2014.

[64] "NPSS ™ REFPROP Thermodynamic Property Package User Guide," 2012.

[65] "NPSS Developer's Guide." 2008.

[66] *NPSS User Guide*, Rev. 4., vol. 01. Cleveland: Ohio Aerospace Institute, 2012.

[67] "NPSS Customer Deck User's Guide." 2008.

[68] D. F. Waters and C. P. Cadou, "Optimization of Gas Turbine - Solid Oxide Fuel Cell Systems for Aircraft Power Generation," in *53rd AIAA Aerospace Sciences Meeting*, 2015, no. January, pp. 1–15.

[69] C. Kelley, *Solving Nonlinear Equations with Newton's Method*. Philadelphia: Society for Industrial and Applied Mathematics, 2003.

[70] S. Gordon and B. J. McBride, "Computer Program for Calculation of Complex Chemical Equilibrium Compositions and Applications, NASA RP-1311." NASA, 1994.

[71] "NPSS Reference Sheets," Cleveland, 2008.

[72] F.-P. Nagel, "Electricity from wood through the combination of gasification and solid oxide fuel cells Systems analysis and Proof-of-concept," ETH Zurich, 2008.

[73] A. H. Lefebvre and D. R. Ballal, *Gas Turbine Combustion: Alternative Fuels and Emissions, Third Edition*, 3rd ed. Taylor & Francis, 2010.

[74] Y. S. Muzychka and M. M. Yovanovich, "Pressure Drop in Laminar Developing Flow in Noncircular Ducts: A Scaling and Modeling Approach," *J. Fluids Eng.*, vol. 131, no. 11, p. 111105, 2009.

[75] Y. S. Muzychka and M. M. Yovanovich, "Laminar Forced Convection Heat Transfer in the Combined Entry Region of Non-Circular Ducts," *J. Heat Transfer*, vol. 126, no. 1, p. 54, 2004.

[76] F. P. Incroprera, D. P. DeWitt, T. L. Bergman, and A. S. Lavine, *Fundamentals of Heat and Mass Transfer*, 6th ed. Hoboken, NJ: John Wiley & Sons, Inc., 2007.

[77] H. Zhu and R. J. Kee, "A general mathematical model for analyzing the performance of fuel-cell membrane-electrode assemblies," *J. Power Sources*, vol. 117, no. 1–2, pp. 61–74, May 2003.

[78] H. Zhu, R. Kee, and G. Jackson, "Solid Oxide Fuel Cells Using Syngas," in *Synthesis Gas Combustion*, CRC Press, 2009, pp. 329–374.

[79] X. B. Zhu *et al.*, "A direct flame solid oxide fuel cell for potential combined heat and power generation," *Int. J. Hydrogen Energy*, vol. 37, no. 10, pp. 8621–8629, 2012.

[80] H. Zhu and R. J. Kee, "Modeling Distributed Charge-Transfer Processes in SOFC Membrane Electrode Assemblies," *J. Electrochem. Soc.*, vol. 155, no. 7, p. B715, 2008.

[81] H. Zhu, R. J. Kee, V. M. Janardhanan, O. Deutschmann, and D. G. Goodwin, "Modeling Elementary Heterogeneous Chemistry and Electrochemistry in Solid-Oxide Fuel Cells," *J. Electrochem. Soc.*, vol. 152, no. 12, p. A2427, 2005.

[82] R. J. Kee, H. Zhu, A. M. Sukeshini, and G. S. Jackson, "Solid Oxide Fuel Cells: Operating Principles, Current Challenges, and the Role of Syngas,"

Combust. Sci. Technol., vol. 180, no. 6, pp. 1207–1244, May 2008.

[83] R. J. Kee, H. Zhu, and D. G. Goodwin, "Solid-oxide fuel cells with hydrocarbon fuels," *Proc. Combust. Inst.*, vol. 30, no. 2, pp. 2379–2404, Jan. 2005.

[84] H. Zhu and R. J. Kee, "Thermodynamics of SOFC efficiency and fuel utilization as functions of fuel mixtures and operating conditions," *J. Power Sources*, vol. 161, no. 2, pp. 957–964, Oct. 2006.

[85] H. Zhu and R. J. Kee, "The influence of current collection on the performance of tubular anode-supported SOFC cells," *J. Power Sources*, vol. 169, no. 2, pp. 315–326, Jun. 2007.

[86] E. Onat and G. W. Klees, "A method to estimate weight and dimensions of large and small gas turbine engines," 1979.

[87] V. Sanghi, S. K. Kumar, S. K. Sane, and V. Sundararajan, "Preliminary Estimation of Engine Gas-Flow-Path Size and Weight," *J. Propuls. Power*, vol. 14, no. 2, pp. 208–214, 1998.

[88] D. Raymer, *Aircraft Design: A Conceptual Approach*, 2nd ed. Washington, DC: American Institute of Aeronautics and Astronautics, Inc., 2012.

[89] C. C. CIEPLUCH, D. Y. DAVIS, and D. E. GRAY, "Results of NASA's Energy Efficient Engine Program," *J. Propuls. Power*, vol. 3, no. 6, pp. 560–568, Nov. 1987.

[90] "Ultra Electronics AMI fuel cells for UAVs, critical military tech," *Fuel Cells Bull.*, vol. 2013, no. 7, p. 4, Jul. 2013.

[91] M. Hanasaki *et al.*, "SOFC Durability against Standby and Shutdown Cycling," vol. 161, no. 9, pp. 850–860, 2014.

[92] L. Mastropasqua, S. Campanari, and J. Brouwer, "Solid oxide fuel cell short stack performance testing - Part A: Experimental analysis and M-combined heat and power unit comparison," *J. Power Sources*, vol. 371, pp. 225–237, 2017.

[93] R. L. Edwards and A. Demuren, "Regression analysis of PEM fuel cell transient response," *Int. J. Energy Environ. Eng.*, vol. 7, no. 3, pp. 329–341, 2016.

[94] P. G. Batterton, "Energy Efficient Engine Program Contributions to Aircraft Fuel Conservation," in *Aviation Fuel Conservation Symposium*, 1984.

[95] J. D. Mattingly, *Elements of Propulsion: Gas Turbines and Rockets*. Reston ,VA: American Institute of Aeronautics and Astronautics, 2006.

[96] N. M. Sammes, R. Bove, and J. Pusz, "Solid Oxide Fuel Cells," in *Fuel Cell Technology: Reaching Towards Commercialization*, N. Sammes, Ed. London:

Springer London, 2006, pp. 1–26.

[97] G. P. Sutton and O. Biblarz, *Rocket Propulsion Elements*. John Wiley & Sons, 2010.

[98] S. G. Chalk and J. F. Miller, “Key challenges and recent progress in batteries, fuel cells, and hydrogen storage for clean energy systems,” *J. Power Sources*, vol. 159, no. 1, pp. 73–80, Sep. 2006.

[99] N. Sammes, Ed., *Fuel Cell Technology*. London: Springer London, 2006.